TOPOLOGICAL PHASES IN THE REAL WORLD

A Dissertation

Presented to the Faculty of the Graduate School

of Cornell University

in Partial Fulfillment of the Requirements for the Degree of

Doctor of Philosophy

by

Yi-Ting Hsu

August 2017

TOPOLOGICAL PHASES IN THE REAL WORLD

Yi-Ting Hsu, Ph.D.

Cornell University 2017

The experimental discovery and subsequent theoretical understanding of the integer quantum Hall effect, the first known topological phase, has started a revolutionary breakthrough in understanding states of matter since its discovery four decades ago. Topological phases are predicted to have many generic signatures resulting from their underlying topological nature, such as quantized Hall transport, robust boundary states, and possible fractional excitations. The intriguing nature of these signatures and their potential applications in quantum computation has intensely fueled the efforts of the physics community to materialize topological phases. Among various topological phases initially predicted on theoretical grounds, chiral topological superconductors and time-reversal symmetric topological insulators (TI) in three dimension (3D) are two promising candidates for experimental realization and application.

The family of materials, Bi_2X_3 (X=Se, Te), has been predicted and shown experimentally to be time-reversal symmetric 3D TIs through the observation of robust Dirac surface states with Rashba-type spin-winding. Due to their robust surface states with spin-windings, these 3D TIs are expected to be promising materials for producing large spin-transfer torques which are advantageous for spintronics application. As for topological superconductors, despite the exotic excitations that have been extensively proposed as qubits for topological quantum computing, materials hosting topological superconductivity are rare to date and the leading candidate in two dimensions (2D), Sr_2RuO_4, has a low transi-

tion temperature (T_c). The goal of my phd study is to push forward the current status of realization of topological phases by materializing higher T_c topological superconductors and investigating the stability of Dirac surface states in 3D TIs.

In the first part of this thesis, I will discuss our double-pronged objective for topological superconductors: to propose how to enhance the T_c of the existing leading candidate Sr_2RuO_4 and to propose new material candidates for topological superconductors. First, by carrying out perturbative renormalization group (RG) analysis, we predicted that straining the ruthenate films will maximize the T_c for triplet pairing channel when the Fermi surface is close to van Hove singularities without tuning on to the singularity. Then with a similar RG approach and a self-consistent calculation for the gap equations, we investigated the repulsion-mediated intrinsic and proximity-induced superconductivity in a family of lightly hole-doped noncentrosymmetric semiconductors, monolayer transition metal dichalcogenides (TMDs). We found that thanks to the spin-valley locking in lightly hole-doped TMDs, two distinct topological pairing states are favored for the intrinsically superconducting case: an interpocket paired state with Chern number 2 and an intrapocket paired state with finite pair momentum. Moreover, nematic odd-parity pairing with a possibly high T_c can be induced when proximitized by a cuprate. A confirmation of our predictions will open up possibilities for manipulating unconventional and topological superconductivity at a higher temperature on the device-friendly platform of strained ruthenate films and monolayer TMDs.

In the second part, I will discuss our studies on the stability of the Dirac surface states in 3D TIs in the presence of bulk states and in TI-ferromagnetic metal heterostructures. We constructed simple microscopic models with Fano-type couplings between localized and extended states for each situation. Then

with ab initio calculations we investigated the fate of the Dirac surface states in terms of the spectrum, the spatial profile and the spin-texture. Based on our results, we proposed explanations for existing experimental spectroscopic and spin-torque results.

BIOGRAPHICAL SKETCH

Yi-Ting Hsu grew up in Taipei, Taiwan, and has lived there until 2005. She joined the Department of Material Science in National Tsing Hua University, Hsin-Chu, Taiwan for 2005-2008, and she transferred to the Department of Physics in 2009. She obtained a Bachelor of Science in Physics at National Tsing Hua University, Hsin-Chu, Taiwan, in 2009 and worked as an associate in Prof. Daw-Wei Wang's group in 2010. She joined Prof. Daw-Wei Wang's group for 2009-2010 and did theoretical studies on ultracold atoms and molecules. She moved to Ithaca, NY, USA in 2010 to pursue a Ph.D in Physics at Cornell University. Yi-Ting Hsu joined Prof. Eun-Ah Kim's group after coming to Cornell to do theoretical research in condensed matter physics. Things that Yi-Ting likes to do during spare time include reading detective novels, playing puzzles, playing go, playing piano and violin, playing badminton and tennis.

This document is dedicated to all Cornell graduate students.

ACKNOWLEDGEMENTS

I really want to say thank you to my advisor Eun-Ah Kim for guiding, helping, and supporting me all along during my Ph.D. I have been learning a lot from her about many aspects in becoming a physicist, including forming interesting ideas, steps in doing research, and communicating results. Besides research, she always looks after each of us in her group for future-career planning and try to help us as much as she can. She has also been very supportive and able to pass the courage to me when I was trapped in difficult or stressful situations in research and in life. I feel very lucky that I had chosen to come to Cornell and joined her group.

I am very grateful to have my family supporting me through these years, including my parents in Taiwan and my husband Yuhsin Tsai, who is now a postdoc in high energy physics in U of Maryland. Through skyping with my parents and visiting them each winter, I firmly feel the warm and support from home. Though we work in different subfields, Yuhsin understands and accompanies me every step I went through. He has always been able to encourage me in convincing ways whenever I got discouraged in research or in life. I enjoy discussing and learning physics from him. I would not be able to go this far without him.

I thank all the faculty members in Cornell physics, applied and engineering physics, and material science that have interacted with me. Special thanks to Erich Mueller, who has spent time discussing my ideas with me and welcomed me to join their group meetings while Eun-Ah was on sabbatical, and also to Katja Nowack, who discusses with me and is leading experimental investigations about my theoretical works on superconductivity in transition metal dichalcogenides (TMD). I am also grateful to have the chances to present my

works in spin IRG led by Dan Ralph and TMD seed meetings led by Katja Nowack every semester, and also an NSF review led by Darrell Schlom. These have been precious experiences for me to communicate with and learn from my experimental collegues participating those meetings. Many thanks to them. I would also like to express my appreciation to the following ab initio experts and experimental collegues that have discussed and collaborated with me: Craig Fennie and his former student Andrew Mulder and former postdoc Alejandro Rebola, Kyle Shen and his student Bulat Burganov.

Special thanks to ab initio expert Kyungwha Park in Virginia Tech, who initiated collaboration and has been collaborating with me since my first March meeting talk. Also many thanks to numerical expert Weejee Cho who was in Stanford. He taught me a lot about coding and had many useful discussion with me during our collaboration.

My current and former group members, office mates and classmates in Cornell have helped me a lot during all these years at Cornell. I thank Kyungmin Lee, Andrej Mesaros, Mark Fischer, and Abolhassan Vaezi for spending time to discuss my questions with me, teach me various things, and/or collaborating with me. I also thank Jordan Venderley, Yi Zhang, Jian-Huang She, and Aaron Hui for sharing their results and dicussing physics with me. I enjoyed chatting, discussing interesting questions and various topics with my office mates Bhuvanesh Sundar, Kyungmin Lee, Ran Wei, and Matt Reichl. I also enjoyed watching them playing crossword puzzles and sudoku everyday. I would also like to thank my classmates Zhen-Wah Tan, Bhuvanesh Sundar and Siddarth Karkare for working on class works together with me. Special thanks to my friend Yan-Jiun Chen who helped me survived the first few years of me Ph.D. I really miss our working parties with Shayna and Yvonne in PSB.

Finally I would like to thank all the friends I met here in Ithaca, who accompanied me through these years. I thank my old and current roommates Adeline Yeh, Shing Hu, Anqi Song and A-Huang for the wonderful accompany. I thank my friends Bianka Lou, Adeline Yeh, and Julia Chen who took turn cooking with me for tolerating my cooking skills. I miss the friends who have left Ithaca: Yi-Ju, Pan Pan, Ginny, Large and Small Pai etc. Special thanks to Amanda Hood, a mathematician who has taught me how to knit, how to bake desserts, and how to play chess. I miss our time going to fitness classes and watching Sherlock Holmes together. And I will miss my friends who are still here: The working party pals Jing-Ting Huang, Whyjay Cheng, Yu-Cian Hong, Shing Hu, Adeline Yeh, Yao-Chuan CHang, Jen-Jie Lee; friends who played badminton and Go with me etc. I will miss all the chatting time and dessert time with Athena Yeh, and I wish her good luck pursuing her dream.

All of you made my years here in Ithaca during my Ph.D shine. I wouldn't have been able to go this far without you.

TABLE OF CONTENTS

LIST OF TABLES

LIST OF FIGURES

CHAPTER 1

INTRODUCTION

1.1 An Overview

A major advance in condensed matter physics over the past four decades is in distinguishing and characterizing states of matter that have the same symmetries but exhibit very different properties. This is a problem beyond the scope of the Landau paradigm which classifies phases using symmetries. The key insight of this revolution is the nontrivial role of topology[161, 48, 49, 51]. In non-interacting systems, the mathematical concept of topology enters the description of phases through the band structure. For instance, in the case of the integer Quantum Hall state (IQHE) where a perpendicular magnetic field is applied to two-dimensional (2D) electron gas at low temperature[87], the filled magnetic Bloch bands exhibit nontrivial Berry curvature[161, 88]. The integration of such curvature over the magnetic Brillouin zone divided by 2π is bound to be an integer that is known as the first Chern number $C = N$, $N \in \mathbf{Z}$[161, 88], which is responsible for the experimentally observed quantized Hall conductance Ne^2/h[87]. Just like the order parameters serve to label symmetry-distinct phases, this first Chern number serves as the topological index that labels the vacuum (C=0) and different integer quantum Hall states ($C = N \neq 0$) exhibiting different values of quantized conductance due to their topologically distinct Bloch bands. In general, insulating phases with a topologically non-trivial band structure feature quantized Hall transport and robust boundary states against perturbations that do not close the bulk gap[51].

Following the experimental and theoretical investigations of the time-

reversal breaking IQHE, several topological band insulators preserving time-reversal symmetry have been predicted[74, 10, 186] and discovered in the past decade such as the HgTe quantum well in two dimensions (2D)[91] and Bi_2Se_3 in three dimensions (3D)[57]. These time-reversal symmetric topological insulators (TI) essentially consist of two copies of quantum Hall insulators with opposite Chern numbers, one for each of the time-reversal partners. Although the overall Chern number is zero such that there is no quantized Hall effect in the charge sector, the topologically nontrivial bulk leads to counter-propagating edge modes of each spin species in 2D, which results in a quantized spin Hall effect (QSHE) [74, 10]. For 3D TIs, the topologically protected surface states have opposite Rashba-type spin windings on the opposite surfaces[57] and have thus become a potentially important element in spintronics[19, 132, 39, 118].

Besides insulators, superconductors can also be topological if described by a Bogoliubov de Gennes Hamiltonian with topologically nontrivial dispersion[142]. In particular, chiral superconductors are topological superconductors that break time-reversal symmetry and are characterized by nonzero Chern numbers[73]. The simplest example of a topological chiral superconductor is a chiral p-wave superconductor[142]. Besides robust boundary states and quantized Hall effects, chiral p-wave superconductors are most famous for being able to host half-quantum vortices with a 'Majorana zero mode' bound in the core[142, 2]. Such exotic excitations have been extensively proposed as qubits for topological quantum computing[124].

1.2 A road map for this thesis

Motivated by the intriguing nature of topological superconductors and insulators and their potential application in quantum computation, my PhD is dedicated to bridging these topological phases which were initially predicted on theoretical grounds towards the experimental accesible world. In this thesis, I will present my studies which focus on two main directions: (1) the materialization of topological chiral superconductors and (2) the stability of 3D TIs' surface states in the context of application to spintronics. I will discuss works along the former direction in Chapter 2 and those along the latter direction in Chapter 3.

1.2.1 Topological superconductors

One of the main challanges in the development of topological superconductors is that materials hosting topological superconductivity are still rare to date. So far the leading as-grown material candidate in 2D is Sr_2RuO_4, which is a transition metal oxide with a layered perovskite structure. Nonetheless, besides the on-going debates over the experimental evidences of edge states and half quantum vortices, this leading candidate suffers from a major disadvantage which is its low transition temperature (T_c) ~1.5 K[71]. To push forward the current status of topological superconductivity, during the past few years my collaborators and I pursued a double-pronged objective: we proposed how to enhance the T_c of Sr_2RuO_4 in an experimentally accesible way, and we also identified a family of widely experimetally studied 2D semiconductors, monolayer transition metal dichalcogenides (TMDs), to be new candidates for topological superconductors. I will discuss studies related to the superconductivity in ruthenates in

section 2.1 and 2.2, and studies related to the superconductivity in monolayer TMDs in section 2.3 and 2.4.

Superconductivity in strained ruthenates

In section 2.1, I will discuss our proposal for how to enhance the T_c of Sr_2RuO_4 through biaxial epitaxial strain. This section is adapted from a published work, Physical Review B **94**, 045118 (2016). An experiment in 2002[40] found that the T_c of a bulk Sr_2RuO_4 decreased with hydrostatic pressure. Our local experimental collaborators, Darrell Schlom's group and Kyle Shen's group, were inspired by this observation and wondered if straining could be a realistic and controllable way to tune the T_c of Sr_2RuO_4. What they managed to accomplish was to grow epitaxially strained ruthenate films with various degrees of biaxial strain and image how the Fermi surfaces evolve under such strain[17]. These films are, however, not yet superconducting due to the disorders.

Thus to predict if the T_c could improve under the strain while the superconductivity stays topological, I carried out a perturbative renormalization group (RG) analysis with an input of ARPES data on films with different degrees of strain. Using this RG method, I was able to calculate the superconducting tendency, which is related to the T_c, and the dominant pairing channel. In collaboration with a coding expert Weejee Cho, a density functional theory (DFT) expert Alejandro Rebola in Craig Fennie's group, and an ARPES expert Bulat Burganov, I found that instead of a monotonic change, the pairing tendency exhibited a peak with an inceasing strain. Moreover, at strain magnitudes where the pairing tendency was close to but not right at the peak, the superconductivity was topological. Here, topological superconductiviy was indicated by a

dominant spin-triplet pairing channel from the 2D band due to the energetics since the four-fold rotational symmetry was preserved in these biaxially strained films. I further understood how these results were related to the Lifshitz transition and the magnetic fluctuations of the 2D band Fermi surface. Most importantly, we predicted a particular strained film to host spin-triplet superconductivity with the highest T_c among all the available strained films and the bulk Sr_2RuO_4. A confirmation of our prediction, which would require a superconducting test on this film with an improved film quality, could lead to a higher-T_c topological superconductor.

In section 2.2, I will discuss a follow-up work on superconductivity in strained ruthenates, concerning the dependence of the perturbative RG method I used in the aforementioned study on the input band structure. This section is adapted from a preprint, arxiv:1701.07884. Here I demonstrated this dependence by an example of uniaxially strained Sr_2RuO_4. While studying the biaxially strained ruthenate films, I worked closely with both angle-resolved photoemission spectroscopy (ARPES) and first-principles experts. From their ARPES data and DFT-calculated band structures of biaxially strained ruthenates, they noticed that there was a large "mass enhancement" effect, which means that the DFT results underestimated the effective mass compared to the ARPES data[17]. Most importantly, they found such effect to be *band-selective* in strained ruthenates, where the effect was much more severe in the 2D band than in the 1D bands[17]. My advisor Eun-Ah and I suspected that generally speaking, such band-selective effect of the input band structure could cause a qualitative difference in the RG results when a DFT-calculated band structure is used rather than the ARPES data. To demonstrate such qualitative difference, I collaborated with a DFT expert Alejandro Rebola and used the RG method to study the supercon-

ductivity in Sr_2RuO_4 under various degrees of uniaxial strain with two sets of input band structures: one was calculated by DFT, and the other was based on ARPES data. We chose uniaxially strained Sr_2RuO_4 because a recent experiment on superconducting uniaxially strained Sr_2RuO_4 found a peak in T_c as the strain magnitude increases. By comparing the RG results using these two sets of input band structures, I found that only the ARPES-based RG result reproduced the observed peak in T_c in experiment while the DFT-based RG result showed a monotonic growth of T_c with increasing strain. Most importantly, such qualitative difference in an observable had its roots in the band-selective mass enhancement, which led to different bands being responsible for the superconductivity in the two sets of results. This work points out an under-appreciated effect in the RG community, and illustrates that extra caution is required when making RG predictions for multi-band superconductors in connection with experiments.

Superconductivity in monolayer TMDs

In section 2.3 and 2.4, I will discuss my effort on searching for new material candidates for topological superconductors. It has been well known that pairs formed by fermions of "the same spin species" are very likely to result in topological superconductivity. A famous proposal along this line was made by Fu and Kane. They proposed to proximitize a single surface of a 3D TI, which hosts a Fermi surface exhibiting only a counterclockwise (or clockwise) Rashba-type spin-winding, by a conventional s-wave superconductor[42]. While much experimental progress has been made in realizing this proposal, the fact that the proposed topological superconductivity exists on the interface between the TI and s-wave superconductor is expected to hinder further surface detection and

analyses of the superconducting properties.

Fortunately, Eun-Ah and I learned from students and postdocs in Dan Ralph's group about a family of graphene-like 2D semiconductors, monolayer transition metal dichalcogenides (TMDs), that has seized rapidly growing attention for its potential application in transistors, photoelectronics and valleytronics. Most interestingly, many of these unusual transport and optical properties result from the "spin-valley locked" band structure in the valance band[190, 159] due to the so-called Ising spin-orbit coupling[107] in the material. In particular, my collaborators and I noticed that lightly hole-doped TMDs have Fermi surfaces whose spin degeneracy is split in momentum space, which is dual to the case in Fu-Kane's proposal where the spin-degeneracy on the Fermi surface was split in real space. We then started to wonder what kind of superconductvity a lightly hole-doped monolayer TMD could host. In fact, superconductivity has been recently discovered in various *electron-doped* TMDs[177, 67, 152, 22]. Nonetheless, unlike the spin-valley locked Fermi pockets of hole-doped TMDs, pockets of the electron-doped TMDs are nearly spin-degenerate and thus not advantageous for topological pairing. Therefore, I began to study the pairing symmetry in lightly hole-doped monolayer TMDs using the RG method that was used in the aforementioned studies on ruthenates.

In section 2.3, I will discuss our study on the intrinsic superconductivity mediated by electronic repulsion in lightly hole-doped monolayer TMDs. This section is adapted from a published work, Nature Communication **8**, 14985 (2017). My collaborators and I predicted that two types of topological superconducting states would dominate: an inter-pocket paired state with Chern number $|C| = 2$ and an intra-pocket paired state which modulates in the real space. I will

further discuss proposals for the detection of these two paired states. As monolayer TMDs are 2D materials that are highly manipulable just like graphene, an experimental confirmation of our predictions will open up new possibilities for employing topological superconductivity on a device friendly platform.

Besides that TMDs are experimentally challenging to hole-doped, another possible obstable for the realization of our proposal is if the lightly hole-doped monolayer TMDs are not intrinsically superconducting. Therefore Eun-Ah and I were motivated to investigate what kind of superconductivity could be induced in lightly hole-doped monolayer TMDs when proximitized by another superconductor. In section 2.4, I will discuss our study on the proximity-induced superconductivity in monolayer TMDs when in contact with a cuprate, which is an experimentally established high-T_c d-wave superconductor. This section is currently being written up for publication in a peer-reviewed journal. By solving the gap equations for the bilayer self-consistently, we found that nematic odd-parity superconductivity is induced in the TMD. Therefore even if lightly hole-doped monolyer TMDs do not intrinsically superconduct, they can still offer a platform for experimental studies of 2D unconventional superconductivity with odd parity and with a possibly high T_c.

1.2.2 Topological Insulators

Unlike topological superconductors, 3D TIs protected by time-reversal symmetry have already been materialized and widely experimentally studied over the past decade[56, 57]. In particular, their robust Dirac surface states which possess Rashba-type spin texture[57, 59] have attracted much attention in terms of

application to spintronics[19, 29, 132, 39, 118, 34]. While being an appealing element in spintronics, these 'topologically protected' surface states, however, might be much more vulnerable than what one would expect in an isolated and theoretically ideal TI when placed in experimental devices. To bridge this gap between the naive theoretical picture for ideal TIs and realistic situations, my collaborators and I have investigated the stability of Dirac surface states under the influence of two important factors that are often present in experimental setups: the surface-bulk coupling arising from the metallic nature of realistic 'TI' materials, and the hybridization with metallic bands in TI-ferromagnetic metal heterostructures. I will discuss the study on surface-bulk coupling in section 3.1, and the study on the hybridization in heterostructures in section 3.2.

Many available materials for 3D TIs, such as Bi_2Se_3, are in fact naturally electron-doped, which makes them topological *metals* rather than insulators[11, 57]. Therefore, identifying the consequences of this coupling between the Dirac surface states and the bulk states becomes a key challenge when exploiting the transport and spin properties of these surface states in devices. In section 3.1, I will discuss an effective model we built that captures the surface-bulk coupling to the lowest order in the spirit of the Fano model. This section is adapted from a published work, Physical Review B **89**, 205438 (2014). The Fano model is a well-studied model describing generally the coupling between a localized state and extended states. My collaborators and I built an effective model for topological 'metals' by including symmetry-preserving Fano-type couplings between the surface and bulk states in a well-known effective model for electron-doped 3D TIs. Together with the DFT calculation on a slab of Bi_2Se_3 done by my collaborator Kyungwha Park, we showed that our effective model is able to capture features observed in previous ARPES and spin-ARPES data on TIs.

Besides the bulk states of the TI itself, the environment surrounding the TI can also cause major changes to the surface states of the TI. For example, it was observed that when a TI was simply left in the vacuum after cleaving, the band-bending effect due to the vacuum not only shifted the chemical potential but also created an additional 2D electron gas on the surface[11, 83]. Another example is that DFT calculations on various TI-insulator heterostructures have shown two interface states with Dirac dispersions, instead of one, at energies away from that of the single Dirac surface state in a bare TI[46, 101, 119]. While the origins of these interface states are still not fully clear, the band-bending effect due to the chemical potential difference between the TI and the insulator has been considered a major cause of the shifts in energy[101, 119].

On the other hand, the fate of the Dirac surface state in a TI-metal heterostructure, a widely used structure in spintronic devices, is even more elusive. This is because besides the band-bending effect, now the Dirac surface state on the interface could very well be destroyed when coupled to all the extented states from the metal layer at similar momenta and energies. Moreover, even if this coupling was negligibly small, the band-bending effect due to the large charge transfer from the metal to the TI is still expected to raise the chemical potential substantially. This is particularly problematic in terms of application to spintronics because the Dirac surface state which has the Rashba-type spin texture would not be able to participate in any transport if buried way below the chemical potential.

What piqued Eun-ah's and my curiosity was the large spin-transfer torque that was recently observed in a TI-permalloy bilayer[118]. This spin-torque signal was attributed by analyses to an interface state with a Rashba-type spin-

winding in the same direction as that of the bare Dirac surface state[118]. We were wondering about the identity of this interface state since it was far from clear to us if the Dirac surface state could suvive near the chemical potential under the influence of the permalloy layer. In section 3.2, I will discuss our effective model for a TI-ferromagnetic metal (FM) heterostructure which reveals the fate of the Dirac surface state in the presence of a substantial amount of charge transfer and severe hybridization with many FM states. This section is currently being written up for publication in a peer-reviewed journal. Combined with a DFT calculation on a Bi_2Se_3-Ni bilayer done by my collaborator Kyungwha Park, we showed that the hybridization not only destroyed the bare Dirac surface state on the interface, but also gave birth to new interface states which we dubbed "descendant states" near the chemical potential. While losing the Dirac dispersion, we found these descendant states to inherit both the spatial localization and the spin texture of the bare Dirac state on the interface. From our effective model and the DFT results, we thus deduce that these hybridization-induced descendent states are an important source of the experimentally observed large spin-torque[118].

CHAPTER 2

TOPOLOGICAL SUPERCONDUCTORS

2.1 Manipulating superconductivity in ruthenates through Fermi surface engineering

This section is adapted from Physical Review B, 94, 045118 (2016), which was in collaboration with Dr. Weejee Cho, Dr. Alejandro Federico Rebola, Bulat Burganov, Dr. Carolina Adamo, Prof. Kyle M. Shen, Prof. Darrell G. Schlom, Prof. Craig J. Fennie, and Prof. Eun-Ah Kim.

Besides the fact that material candidates for topological superconductors are still rare to date, one major challenge in the studies of topological superconductivity is that the transition temperature (T_c) of the leading candidate, Sr_2RuO_4, is low. To improve the T_c of Sr_2RuO_4, my collaborators and I put forth a new strategy, which is to combine theoretical developments in the weak-coupling renormalization group (RG) approach with the experimental developments in Fermi-surface (FS) engineering using lattice strain. To be specific, my experimental collaborator Carolina Adamo in Darrell Schlom's group managed to grow ruthenate films with different degrees of biaxial strain introduced by different substrates and an isovalent substitution $Sr \rightarrow Ba$[17]. Bulat Burganov in Kyle Shen's group then imaged the FSs of these films using angle-resolved photoemission spectroscopy (ARPES) and found that the Fermi pocket of the 2D band has overgone Lifshitz transition as the strain increased[17]. To predict if Sr_2RuO_4 can stay topological while the T_c increases under such change in that Fermi pocket, my goal is

to calculate the superconducting tendency in each pairing channel in the biaxially strained films. Using the density-functional-theory(DFT)-calculated band structures provided by Alejandro Rebola in Craig Fennie's group, I first test the RG method on uniaxially strained Sr_2RuO_4 and compare the result with the experimentally measured trend of T_c in strain[149]. Then with the ARPES-extracted low-energy band structure provided by Bulat Burganov, I carry out the RG calculation on the biaxially strained films with the help of a coding expert Weejee Cho. I find that the superconducting tendency of the spin-triplet pairing channel in the 2D band stays dominant, which indicates topological superconductivity, and becomes maximized when the 2D band Fermi pocket is close to but not sitting right at the van Hove singularities.

2.1.1 Introduction

The notion of topological superconductivity [167, 143, 65, 32, 124, 158, 28] drove intense investigation of a triplet superconductor Sr_2RuO_4 [64, 125, 76, 84, 30, 66]. Unfortunately its fairly low transition temperature $T_c \sim 1.5$ K[108] has been one of the limiting factors for experimental studies. Naturally there has been much interest in enhancing the T_c of Sr_2RuO_4. Since the T_c is extremely sensitive to disorder, the usual tuning knob of doping is not an option. On the other hand, successes in both local enhancement of T_c in eutectic samples[109, 3] and near dislocations[178] and in global enhancement of T_c using c-axis uniaxial pressure[86, 85] and in-plane uniaxial strain[54] point to a new knob: the lattice strain. Now the key question is how to connect this new knob to a theoretical framework that can guide the quest for higher T_c topological superconductor.

T_c is generally hard to theoretically predict since it is a non-universal quantity which depends on microscopic details of the system. The fact that one cannot just apply mean-field theory for repulsion-driven anisotropic superconductors makes it even worse. Nevertheless Kohn and Luttinger[89] have observed early on that even with a short-range bare repulsion, the momentum-dependence in the irreducible particle-particle vertex from higher order corrections can still give rise to a Cooper instability in a suitable channel. This insight was further developed for Hubbard type models on lattice [183, 47, 148, 55, 138]. A common thread in these approaches is the fact that the band structure near Fermi surfaces (FS) determines the bare susceptibilities which enter the expression for the pairing interaction. This invites the notion of controlling superconductivity through controlling fermiology, going beyond the traditional approach of doping [184, 160, 26, 121].

Our idea is to employ the weak-coupling renormalization group (RG) approach[138, 135] in embracing the new experimental knob of lattice strain. Since the pioneering work of Chu *et al.*[25], piezoelectric-based control of lattice strain has become a new knob. This approach was further developed[53] to enable substantial uniaxial strain on bulk Sr_2RuO_4 and led to a 40% enhancement of T_c[54]. A recent experimental advance by Darrell Schlom's group and Kyle Shen's group in growing epitaxially strained ruthenate films[18] presents a new opportunity. This is particularly exciting because the epitaxial strain can dramatically alter the band structure[18].

Here, we theoretically investigate how strain affects the fermiology and the associated superconducting tendencies. For this, we extract tight-binding parametrization from ARPES data and a density functional theory(DFT) cal-

culation on strained systems. We then use the tight-binding model as the microscopic input to the RG calculation to study superconducting instability. We examine the cases of piezoelectric-based uniaxial strain[54] and epitaxial biaxial strain[18]. We reproduce the observed trend for the case of uniaxial strain and predict non-monotonic dependence of the T_c on the biaxial strain.

2.1.2 The Model and the Approach

Our microscopic starting point is a three-band Hubbard model derived from the Ru t_{2g} orbitals d_{xz}, d_{yz}, and d_{xy}:

$$H = \sum_{\vec{k}\alpha\sigma} \epsilon^{\alpha}(\vec{k}) c^{\dagger}_{\vec{k},\alpha,\sigma} c_{\vec{k},\alpha,\sigma} + U \sum_{i\alpha} n_{i,\alpha,\uparrow} n_{i,\alpha,\downarrow}, \tag{2.1}$$

where $\vec{k} = (k_x, k_y)$, $\alpha = xz, yz, xy$, $\sigma = \uparrow, \downarrow$ denote the crystal momentum, the orbital index, and the spin respectively, and $n_{i,\alpha,\sigma} \equiv c^{\dagger}_{i,\alpha,\sigma} c_{i,\alpha,\sigma}$. Given the well-established unconventional aspects of superconductivity in bulk Sr_2RuO_4 [64, 125, 76], we focus on the repulsive intra-orbital on-site repulsion $U > 0$[89, 135]. [1]

For the intra-orbital kinetic energies $\epsilon^{\alpha}(\vec{k})$ we employ the following tight-binding parameterization:

$$\begin{aligned}
\epsilon^{xz}(\vec{k}) &= -2t_x \cos k_x - 2t_y^{\perp} \cos k_y - \mu_1 \\
\epsilon^{yz}(\vec{k}) &= -2t_y \cos k_y - 2t_x^{\perp} \cos k_x - \mu_1 \\
\epsilon^{xy}(\vec{k}) &= -2(t_x' \cos k_x + t_y' \cos k_y) - 4t'' \cos k_x \cos k_y - \mu_2
\end{aligned} \tag{2.2}$$

where we neglect the orbital-mixing terms. Although Scaffidi *et al.* [150] found

[1] We are not including the inter-orbital repulsion V in this letter. Nevertheless we have checked that the inter-orbital $V \leq 0.5U$ makes no qualitative difference to the results we report.

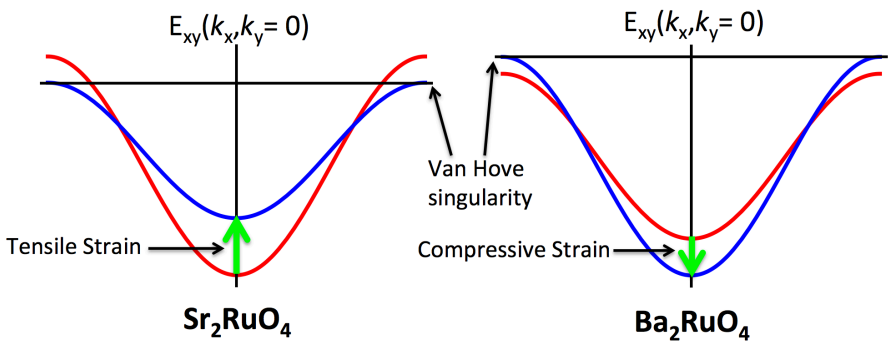

Figure 2.1: The effect of epitaxial biaxial strain on the xy 2D-band in Sr_2RuO_4 and Ba_2RuO_4, respectively. Red curves are unstrained bands. Bands were obtained by fitting tight-binding parameters to DFT data.

the spin-orbit coupling in particular to significantly alter the nature and mechanism of pairing in the unstrained system, the van Hove singularities occur at point $X = (\pi, 0)$ and $Y = (0, \pi)$ which lie in the region of the FS where orbital characters are well defined[146, 72, 52, 164] Hence we expect the absence of orbital-mixing terms in our model would not affect our conclusions in a qualitative manner. The dispersions of the three bands in Eq. (2.2) yield two quasi-one dimensional(1D) FS's consisting of the Ru orbitals d_{xz} and d_{yz}, and one quasi-two dimensional(2D) FS consisting of the Ru orbital d_{xy}.

We connect the lattice strain to the model Eq. (2.2) through the ARPES data of Ref. [18] and DFT calculations. Unstrained Sr_2RuO_4 and its close relative Ba_2RuO_4 have van Hove singularities of the d_{xy} character(2D xy band) at the X and Y points slightly above (Sr_2RuO_4) or below (Ba_2RuO_4) the Fermi level (see the Supplementary Material (SM) subsection II.B). When applying uniaxial tensile strain in [100] direction on these quasi 2D ruthenates, one expects[54, 36] the bandwidth to decrease along [100] direction while behaving oppositely in the [010] direction. Our DFT calculations indeed predict the density of states of the xz and xy band to show similar amount of growth for small magnitude of

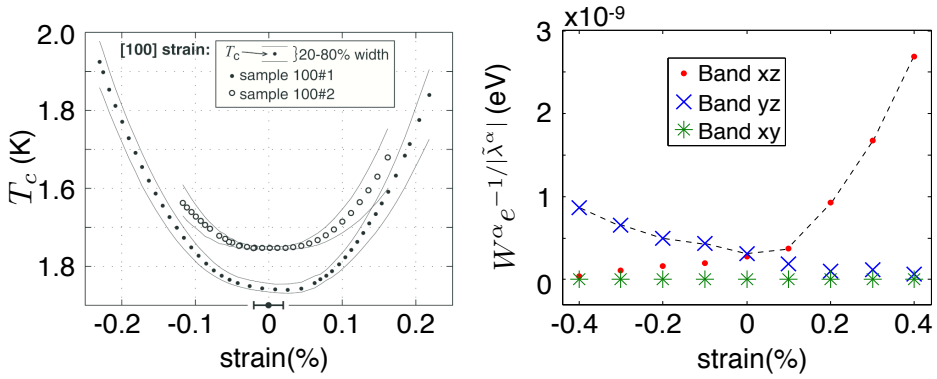

(a) (b)

Figure 2.2: (a)Measured T_c under both tensile(>0) and compressive(<0) uniaxial strain in [100] direction presented in Ref. [54]. (b) Calculated quantity $W^\alpha e^{-1/|\tilde{\lambda}^\alpha|}$ under different amounts of uniaxial strain in the [100] direction with $U = 1$ eV. The black dashed line shows the expected transition temperature T_c.

uniaxial strain(see SM subsection II.A) although it is the xy band that eventually reaches the van Hove singularity at X or Y at a large enough strain(see SM subsection II.A). As for the biaxial strain, we predict Sr_2RuO_4 and Ba_2RuO_4 to reach the van Hove singularity at both X and Y points at the Fermi level under a tensile and compressive strain respectively (see Figure 2.1 and SM subsection II.B), consistent with the experimental observations of Ref. [18] (see Fig. 2.10). Moreover, we find this shift to the van Hove singularity to be driven by both the change in the bandwidth of the xy band (see Fig. 2.1) and the charge-transfer from the xz and yz bands (see SM subsection I). Nevertheless DFT consistently overestimates the Fermi velocities v_F compared to ARPES, in particular that of the 2D band xy[18].

For completeness we now briefly review the two-step perturbative RG approach[138, 135] we adopt. As a first step we numerically calculate the effective pairing vertices in different channels at some intermediate energy scale $E = \Lambda_0$ near the FS by integrating out higher energy modes down to Λ_0. To the

one-loop order, the singlet and triplet effective pairing vertices $\Gamma^{\alpha}_{s/t}(\hat{k},\hat{k}')$ at energy Λ_0 are related to the repulsive bare interaction U and the static particle-hole bubbles $\Pi^{\alpha}_{ph}(\vec{q})$ through

$$\Gamma^{\alpha}_{s}(\hat{k},\hat{k}') = U + U^2\Pi^{\alpha}_{ph}(\hat{q}=\hat{k}+\hat{k}'), \tag{2.3}$$

and

$$\Gamma^{\alpha}_{t}(\hat{k},\hat{k}') = U^2\Pi^{\alpha}_{ph}(\hat{q}=\hat{k}-\hat{k}'). \tag{2.4}$$

Now the pairing tendency hosted by band α in each of the two pairing channels can be quantified by the most negative eigenvalue $\tilde{\lambda}^{\alpha}_{s/t} \equiv \lambda^{\alpha}_{s/t}(E=\Lambda_0)$ of a dimensionless matrix $g^{\alpha}_{s/t}(\hat{k},\hat{k}')$, which is a product of the density of states(DOS) $N^{\alpha}(\Lambda_0) \sim N^{\alpha}(0)$ and the normalized effective pairing vertices at the intermediate energy scale Λ_0:

$$g^{\alpha}_{s/t}(\hat{k},\hat{k}') = N^{\alpha}(\Lambda_0)\sqrt{\frac{\bar{v_F}^{\alpha}}{v^{\alpha}_F(\hat{k})}}\Gamma^{\alpha}_{s/t}(\hat{k},\hat{k}')\sqrt{\frac{\bar{v_F}^{\alpha}}{v^{\alpha}_F(\hat{k}')}}. \tag{2.5}$$

Here $\hat{k}^{(')}$ are the outgoing(incoming) momenta on the FS of band α, $v^{\alpha}_F(\hat{k})$ is the magnitude of Fermi velocity at $\hat{k}$, and $\frac{1}{\bar{v_F}^{\alpha}} \equiv \int \frac{d\hat{p}}{S^{\alpha}_f}\frac{1}{v^{\alpha}_F(\hat{p})}$ with $S^{\alpha}_F \equiv \int d\hat{p}$ being the FS 'area' of orbital α. The second step is to study the RG flows of the most negative eigenvalues $\lambda^{\alpha}_{s/t}(E)$ for different channels (α, s/t). Given the well known RG equations for the Cooper instability, $\frac{d\lambda^{\alpha}_{s/t}}{dy} = -(\lambda^{\alpha}_{s/t})^2$ in terms of $y \equiv \log(\Lambda_0/E)$[151], we can relate T_c to the most negative $\tilde{\lambda}^{\alpha}_{s/t}$ among all channels ($\tilde{\lambda}$) as $\mathrm{T_c} \propto \mathrm{e}^{-1/|\tilde{\lambda}|}$[135].

2.1.3 Uniaxially strained Sr_2RuO_4

Hicks *et al.*[54] found the superconducting T_c of Sr_2RuO_4 to enhance under both tensile and compressive uniaxial strain in [100] direction(see Fig. 2.2(a)). They

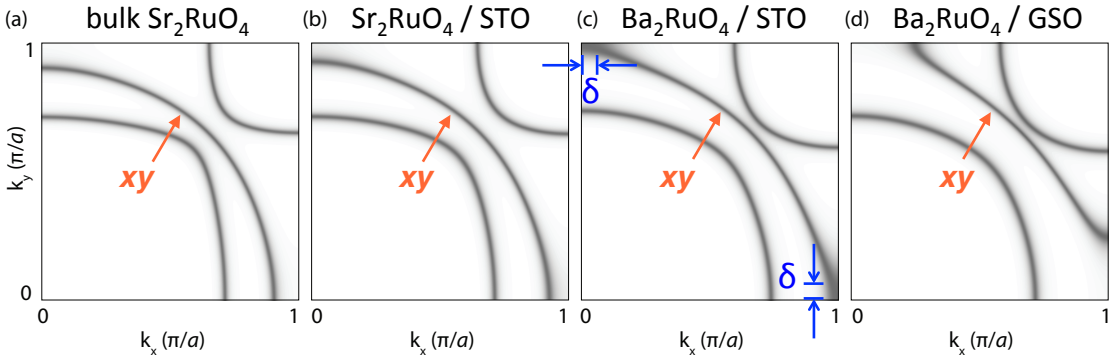

Figure 2.3: The spectral functions extracted from the ARPES data in Ref. [18] for (a) the bulk Sr_2RuO_4, (b) Sr_2RuO_4/ STO, (c) Ba_2RuO_4/ STO, and (d) Ba_2RuO_4/ GSO respectively. The distance from the hole pockets to the van Hove singularities located at $\vec{k}$=$(\pm\pi, 0)$ and $(0, \pm\pi)$ are denoted by δ in (c). The parameterizations for the bulk Sr_2RuO_4, Sr_2RuO_4/ STO, Ba_2RuO_4/ STO, and Ba_2RuO_4/ GSO are $(t, t^{\perp}, \mu_1, t', t'', \mu_2, t_{hyb})$ = (0.165, 0.0132, 0.178, 0.119, 0.0488, 0.176, 0.0215), (0.14, 0.0126, 0.148, 0.114, 0.0456, 0.171, 0.0224), (0.115, 0.0219, 0.112, 0.095, 0.0365, 0.1463, 0.0161), and (0.085, 0.0162, 0.074, 0.07, 0.0245, 0.11, 0.0136) in the unit of eV respectively.

then used phenomenological Ginzburg-Landau analysis to interpret that the enhancement of T_c was driven by the enhancement of density of states in one of the two quasi-one dimensional bands. Here, by determining the tight-binding parameters from DFT calculations under strain we gain insight into the interplay between strain and electronic structure. Further by feeding the the strained tight-binding parameters into the RG procedure, we can let our RG flow start from experimentally relevant short-distance physics.

We then carried out the RG analysis to obtain the most negative eigenvalues $\tilde{\lambda}^{\alpha}_{s/t}$, which are determined by the DOS $N^{\alpha}(0)$, band width W^{α}, and the on-site repulsion U. Fig. 2.2(b) shows a quantity corresponding to T_c which involves the pairing tendency of band α quantified by the more negative eigenvalue be-

tween singlet and triplet channels $\tilde{\lambda}^{\alpha} \equiv \min(\tilde{\lambda}^{\alpha}_{\mathrm{s}}, \tilde{\lambda}^{\alpha}_{\mathrm{t}})$ under different amounts of strain. We find that while the strain enhances the density of states of both 1D and 2D bands moderately (see SM subsection II.A), the strong pairing interaction of the 1D bands due to the antiferromagnetic fluctuation further amplifies the enhancement in the 1D pairing tendencies $|\tilde{\lambda}^{xz/yz}|^2$. As the more dominant of the two 1D bands will onset the superconducting transition, our results imply the transition temperature T_c to follow the dashed curve in Fig. 2.2(b) as a function of tensile and compressive strain. Note that the estimated value of U from first principle calculations is at the order of eV[163], which is beyond the weak coupling regime. Nonetheless, we set $U = 1$ eV in Fig. 2.2(b) for illustrative purposes. The so obtained strain dependence of the T_c qualitatively captures the measured trend [54] shown in Fig. 2.2(b).

2.1.4 Biaxially strained ruthenates thin films

We now turn to the epitaxial ruthenate films under biaxial strain[18]. Biaxial strain has the advantage that it retains the tetragonal symmetry necessary for the onset of topologically non-trivial $p_x + ip_y$ order parameter. Further, since X and Y points are approached simultaneously the van Hove singularity is expected to have a more substantial impact under biaxial strain(see SM subsection II. A and B). On the other hand, epitaxial strain can only access a discrete set of strain values and likely none will be precisely tuned to the van Hove point. But this may be a blessing since there are two theoretical issues when reaching the van Hove singularity. First, the van Hove points at X and Y points are forbidden

[2]We should note that DFT electronic structure significantly underestimate the density of states and the ferromagnetic fluctuation of the 2D band xy in particular, which can affect the balance.

from supporting a odd-parity triplet pairing by symmetry[174, 122]. Secondly, other ordering tendencies that can also benefit from the van Hove singularity can compete with superconductivity[77, 106]. Hence by being close to a van Hove singularity without tuning into one, epitaxial biaxial strain may optimize triplet pairing.

Four representative samples we consider are the unstrained bulk Sr_2RuO_4, a Sr_2RuO_4 film grown on $SrTiO_3$ (Sr_2RuO_4/ STO), a Ba_2RuO_4 film grown on $SrTiO_3$ (Ba_2RuO_4/ STO), and a Ba_2RuO_4 film grown on $GdScO_3$ (Ba_2RuO_4/ GSO). See Fig. 2.10(a)-(d) for the associated spectral function of quasi-particles simulating the ARPES data, where the *xy*-band is electron-like in Fig. 2.10(a)-(b) and hole-like in Fig. 2.10(c)-(d) [3]. Interestingly, the DFT calculations consistently underestimate the density of states and the Lindhard susceptibility at small $\vec{q}$ of the *xy*-band: $N^{xy}(0)$ and $\Pi^{xy}_{ph}(\vec{q})$ at small $\vec{q}$. For our RG analysis we use the parameters $t_x = t_y \equiv t$, $t^{\perp}_x = t^{\perp}_y \equiv t^{\perp}$, and $t'_x = t'_y \equiv t'$ extracted from the ARPES data of Ref. [18].

In Fig. 2.4 we show the resulting most negative eigenvalues $\tilde{\lambda}^{\alpha}_{s/t}$ of singlet and triplet channels hosted by each band α for the four representative samples. Since the measured effect of strain on the band structures of the 1D bands is mild, the eigenvalues associated with the 1D bands do not change drastically. The tight competition between different channels of unstrained system[135, 150] is lifted as triplet pairing tendency of 2D band shoots up to become clearly leading instability in the vicinity of the Lifshitz transition. Moreover, this leading pairing tendency shows a striking non-monotonic dependence on the strain with significantly improved pairing tendency in film Ba_2RuO_4/ STO. Importantly, as

[3]The simulation included an additional hybridization term between the 1D bands with strength $V_{hyb}(\vec{k}) = 4t_{hyb} \sin k_x \sin k_y$ extracted from the ARPES data[18].

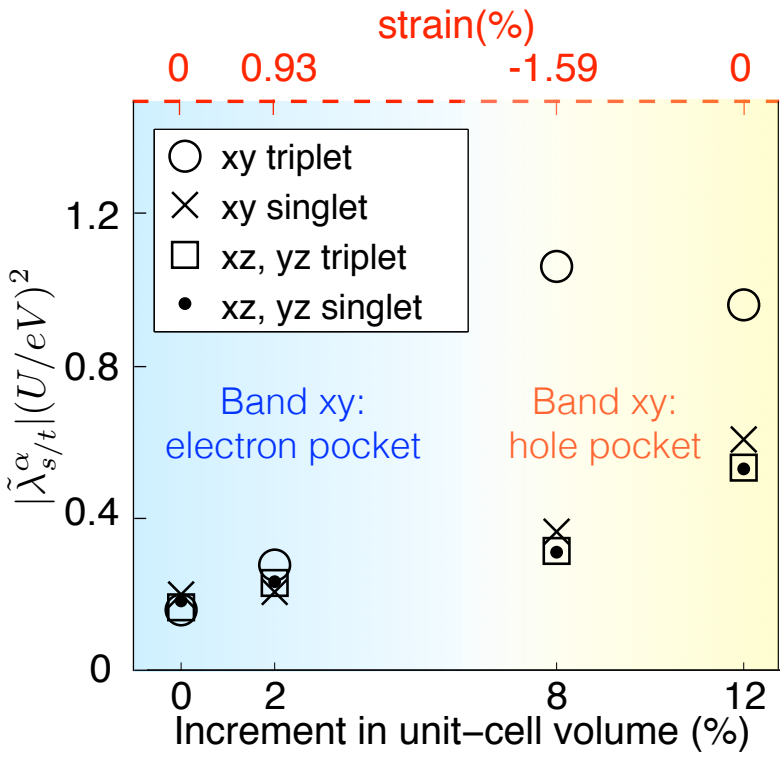

Figure 2.4: The magnitudes of the most negative eigenvalues $\tilde{\lambda}^{\alpha}_{s/t}$ of different channels (α, s/t) for the four representative samples. In the order of increasing volume of one unit cell, the ticks on the horizontal axis mark the four representative samples: the bulk Sr_2RuO_4(0%), and the films Sr_2RuO_4/ STO(2%), Ba_2RuO_4/ STO(8%), and Ba_2RuO_4/ GSO(12%). The percentage refers to the increase in the volume of one unit cell compared to that of the unstrained bulk Sr_2RuO_4. The upper horizontal axis shows the in-plane strain of each Sr_2RuO_4 and Ba_2RuO_4 sample defined with respect to the bulk Sr_2RuO_4 and Ba_2RuO_4/ GSO respectively.

the Ba_2RuO_4/ STO film is slightly away from the actual van Hove singularity by a small distance δ(see Fig. 2.10(c)) triplet pairing is allowed by symmetry.

The significant enhancement in the triplet pairing tendency of the 2D band in the Ba_2RuO_4/ STO film is due to the conspiracy between the enhanced DOS of the 2D band and associated enhancement in the ferromagnetic fluctuation in the measured band structure that enters the triplet pairing vertex through the

bare particle-hole bubble $\Pi^{xy}_{ph}(\vec{q} = 0)$. Interestingly, although the singlet pairing tendency of the 2D band also benefits from the enhanced DOS of the 2D FS near the van Hove singularity, the antiferromagnetic fluctuation which facilitates the singlet pairing does not benefit from the proximate van Hove singularities as much due to the lack of perfect nesting.

2.1.5 Summary

In summary, we theoretically investigated how strain-driven changes of band structure should impact the superconducting instabilities in ruthenates. Considering the effect of mild uniaxial strain of the degree achieved in Ref. [54], we confirmed our approach of using the strained band structure as an input to the RG calculation qualitatively reproduce the observed T_c -dependence on the lattice strain. We then noted by order few %strain the FSs can be altered sufficiently to come close to the nearby van Hove singularity. As such degree of biaxial strain has been achieved by Darrell Schlom's group and Kyle Shen's group[18] and shown to result in van Hove singularity in the 2D band, we used the band structure extracted from ARPES data as the input to the weak-coupling RG procedure and predicted triplet superconductivity with enhanced T_c to be driven predominantly by 2D bands near van Hove singularity. In order to test our predictions, the film purity[108] and structural order[116, 191] need to improve. Recent success in growing superconducting Sr_2RuO_4 thin films[97] makes us optimistic that point defects and extended defects of strained films can be sufficiently reduced.

It is important to note that in the proposed strategy of engineering Fermi

surface and using the resulting band structure as an input to an RG procedure, the aspects of results that are of great interest such as pairing channel and the T_c are non-universal aspects that are sensitive to microscopic details. As we propose to use this very sensitivity to engineer a desired superconductor with the advancement of experimental capabilities[54, 18, 157], we should also stress the importance of basing the microscopic model to the measurement of the actual band structure.

Acknowledgement – The authors are grateful to Andrew Mulder, Srinivas Raghu, Andrey Chubukov, Andy MacKenzie, Thomas Scaffidi, Fuchun Zhang, Steve Kivelson, Ronny Thomale, and Hong Yao for helpful discussions. After completion of this work, we have become aware of two preprints Ref. [157] and Ref. [106] focusing on uniaxial strain effects on Sr_2RuO_4. Steppke *et al.* [157] experimentally achieved the necessary uniaxial strain to access the van Hove singularity and compared the results with theoretical approach similar to that used in this paper but with somewhat different microscopic model. Liu *et al.*[106] used a functional renormalization group approach on a single band model focusing on the 2D band to study the competition between superconductivity and spin density waves under uniaxial strain approaching van Hove. This work was supported by the Cornell Center for Materials Research with funding from the NSF MRSEC program (DMR-1120296). Y-TH and E-AK acknowledge support from NSF grant no. DMR-0955822. WC was supported by NSF grant no. DMR-1265593. AFR and CJF acknowledge support from the NSF grant no. DMR-1056441.

2.1.6 Supplementary Note 1: Effects of strain on bandwidth and occupation

When either uniaxial or biaxial tensile strain is applied to the ruthenates, the bond length along the direction of strain increases which causes band-flattenings in the same direction (see Fig. 2.1 of the main text). On the other hand, a dramatic change in the shape of the bands is at the same time accompanied by a charge-transfer among different bands. In Fig. 2.5 we show the *d*-orbital crystal field splitting corresponding to the RuO_6 octahedra in Sr_2RuO_4 before and after applying strain (for comparison we also include the splitting corresponding to a perfect octahedral environment). In the biaxial case, tensile strain enlarges both in-plane lattice parameters while simultaneously reducing the out-of-plane one. The resulting octahedron is then less elongated and the energy splitting between orbital *xy* and orbital *xz, yz* is reduced. Consequently the occupation of the *xy* level increases. Such charge-transfer together with the flattening of the *xy* band along the strain direction could bring the quasi-2D Fermi surface which is already close to van Hove singularity in the absence of strain to one or both of the van Hove points $X = (\pi, 0)$ and $Y = (0, \pi)$. Similar effects occur in Ba_2RuO_4 under an opposite direction of strain due to the fact that the Fermi level lies above the van Hove points instead of below (see Fig. 2.1 of main text).

2.1.7 Supplementary Note 2: DFT calculation on strained ruthenates

In order to gain a deeper insight into the interplay between strain and electronic structure in ruthenates we perform DFT calculations by systematically varying the applied amount of uniaxial and biaxial strain. We use the PBEsol exchange-correlation functional as implemented in VASP[93, 13] with a plane wave basis cutoff of 520 eV. For structural and static calculations we use a 8x8x4 and 12x12x12 sampling of the Brillouin zone, respectively. Full structural relaxations are performed on Ba_2RuO_4 and Sr_2RuO_4 and the optimized cells thus obtained are the unstrained unit cells we later use in uniaxial and biaxial calculations. The resulting lattice constants are in both cases in good agreement with experiment: the obtained values are a = 3.947Å (exp. 3.990Å), c = 13.417Å (exp. 13.430Å) for Ba_2RuO_4, and a = 3.831Å (exp. 3.871Å) , c = 12.731Å (exp. 12.739Å) for Sr_2RuO_4[18]. Despite the negligible underestimation of the experimental value for the c lattice constant, we find the calculated in-plane lattice constant a to be underestimated by a 1% for both ruthenates, which leads to an artificial elongation in the RuO_6 octahedron. Moreover, while the Fermi velocities of all three bands *xz*, *yz*, *xy* are underestimated compared to the ARPES data, in particular we find the Fermi velocity of band *xy* to be underestimated the most which agrees with the observation made in Ref. [18]. These underestimation in turns reduces the *xy* band occupations and the DOS at the Fermi level for this band.

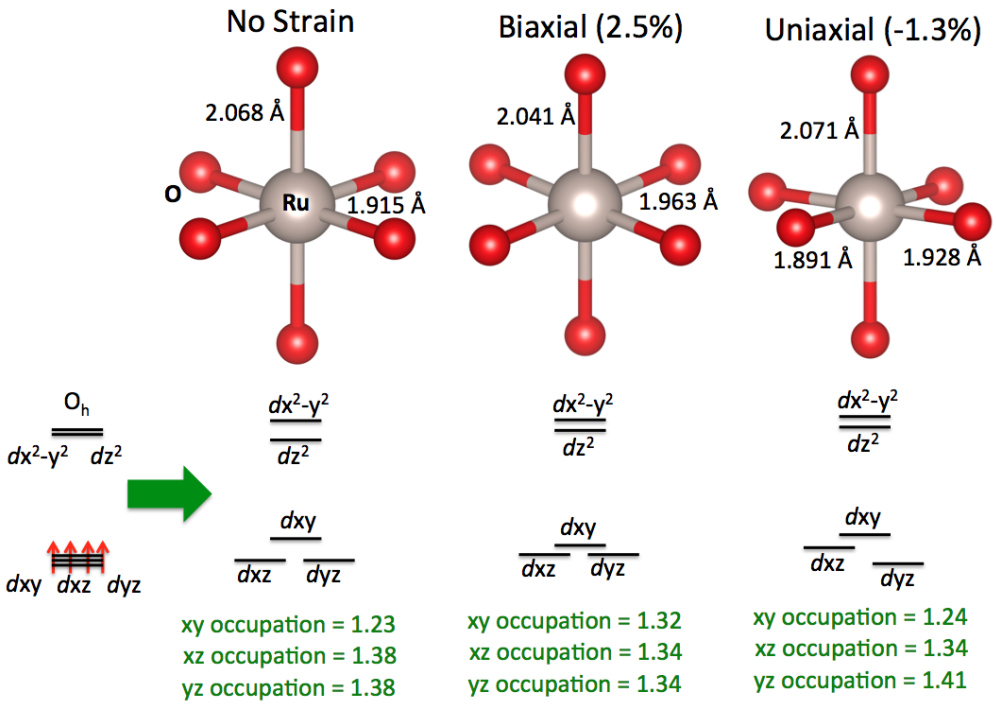

Figure 2.5: Crystal field splitting of energy levels in Sr_2RuO_4: unstrained, under tensile biaxial strain and under compressive [100] uniaxial strain. Octahedral symmetry is broken in the three cases. In the biaxial case, changes in the bond lengths decrease the energy difference between *xy* and *xz*, *yz* levels, increasing the *xy* occupation. For uniaxial case, bond lengths are reduced along the [100] direction and increased along [010], as a result the *xz* and *yz* levels are shifted up and down, respectively.

Uniaxial strain

We relax the internal structural degrees of freedom and transverse lattice constants by keeping the [100] direction fixed at the desired strain amount. The Fermi surfaces (FSs) and dispersions obtained from DFT are then used to fit the parameters for the tight-binding model in Eq. (2) in the main text.

In Fig. 2.6 we show the evolution of the band-projected density of states

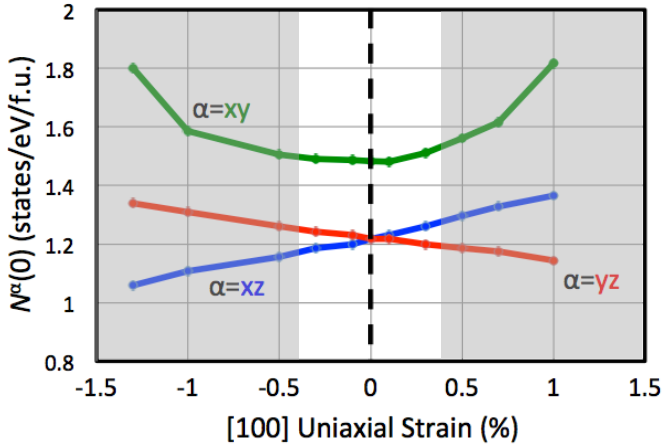

Figure 2.6: The density of states at the Fermi level for *xy*, *xz* and *yz* bands under tensile(>0) and compressive(<0) uniaxial strain. The unshaded regime is the regime with small strain magnitude which corresponds to Fig. 2(b) in main text.

(DOS) at Fermi level ($N^{\alpha}(0)$) as a function of [100] uniaxial strain in Sr_2RuO_4. As bond lengths along the *x*-direction are reduced, bond lengths along *y* increase. Consequently *yz* bands become less dispersive and the number of states at Fermi level is increased while it is reduced for *xz*. At the same time occupation for the *xz* bands decreases, while increasing for *yz* (see Fig. 2.5). Note that though the DOS of the *xy* band starts to thrive at a large amount of strain due to the van Hove singularity, the growths in DOS of *xz*(*yz*) and *xy* bands under a small amount of tensile(compressive) strain are of similar magnitudes as shown in the unshaded area. This small strain regime is the regime where we investigate the superconducting tendencies in Fig. 2(b) of the main text.

In our calculation, the *xy* band meets the van Hove points *X* and *Y* at the Fermi level for a [100] compressive strain of 1.3% and for a [100] tensile strain of 1% (see the top panel of Fig. 2.7). The larger value for [100] compressive strain

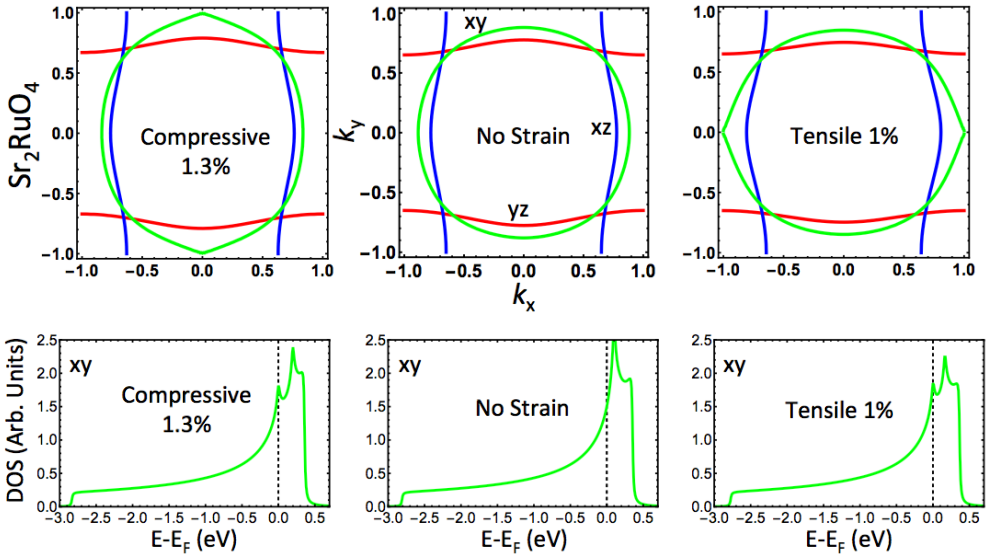

Figure 2.7: FSs at $k_z = 0$ for Sr_2RuO_4 (top panel) and the corresponding DOS for the xy band (bottom panel) as a function of [100] uniaxial strain. The uniaxial strain lowers the symmetry from D_{4h} to D_{2h}. As a result, while the peak in the DOS of xy band due to the van Hove point $X = (\pi, 0)$ sits at the Fermi level, the peak due to the van Hove point $Y = (0, \pi)$ lies above the Fermi level by around 200 meV. Units of k_x and k_y are π/a and π/b respectively, where a and b are the in-plane lattice constants.

is due to the in-plane Poisson ratio (≈ 0.4)[126] of Sr_2RuO_4. From the xy band DOS shown in the bottom panel of Fig. 2.7, we notice the peak due to van Hove singularities in the unstrained case splits into two peaks under strain. This is a consequence of uniaxial strain reducing the symmetry from D_{4h} to D_{2h}.

Biaxial strain

We perform DFT calculations for a wide range of values of tensile and compressive strain by fixing the in-plane lattice constants and letting all internal and out-of-plane lattice constant to relax. We then fit the tight-binding model pre-

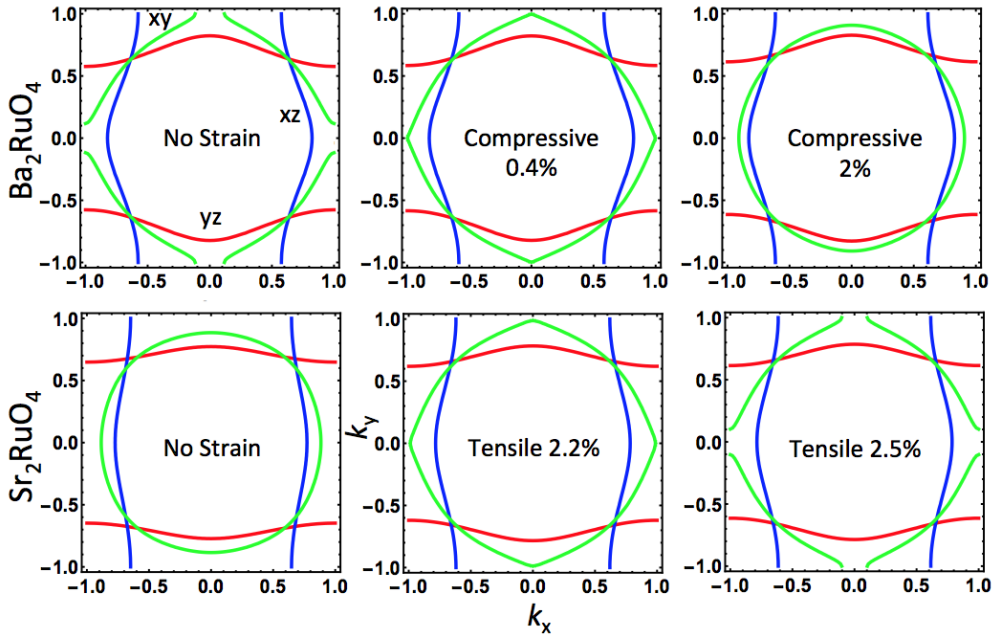

Figure 2.8: FSs at $k_z = 0$ for Ba_2RuO_4 (top panel) and Sr_2RuO_4 (bottom panel) as a function of strain obtained by fitting the tight-binding model to DFT data. While the Fermi level of Sr_2RuO_4 approaches the van Hove points $X = (\pi, 0)$ and $Y = (0, \pi)$ under a tensile strain, the opposite trend is predicted for Ba_2RuO_4. k_x and k_y are in the unit of π/a where a is the in-plane lattice constant.

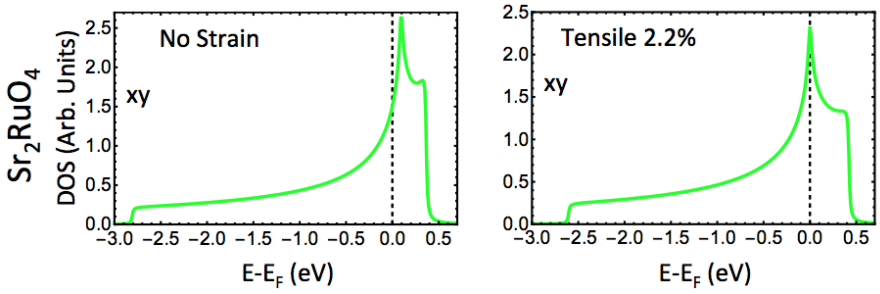

Figure 2.9: The density of states for Sr_2RuO_4 before and after applying the biaxial strain.

sented in the main text to our DFT data. As illustrated in Fig. 2.1 in the main text, in the case of Sr_2RuO_4 the hopping parameters decrease and the bands become flatter with tensile strain, thus approaching the van Hove singularity. Due to the simultaneous increase of in-plane bond lengths together with a decrease of the out-of-plane ones, *xy* energy levels move downwards while *xz* and *yz* are shifted up (Fig. 2.5). As mentioned in section I, this results in an enhancement of the *xy* occupation which further contributes to reaching the van Hove singularity. Our calculations predict a peak in the DOS of the *xy* band due to the Van Hove singularities at both X and Y at the Fermi level for a tensile strain of $\approx$ 2.2 % (lower panel in Fig. 2.8 and Fig. 2.9). Contrarily, for Ba_2RuO_4 it requires a compressive strain of $\approx$ 0.4 % (upper panel in Fig. 2.8). This is due to the fact that in Ba_2RuO_4 the *xy* band lies below the Fermi level and thus a compressive strain needs to be applied in order to increase the hopping parameters and broaden the band (see Fig. 2.1 in the main text). One important difference from the uniaxial strain case is that D_{4h} symmetry is preserved under biaxial strain such that the *xy* band FS can meet both van Hove points simultaneously. Thus the DOS of *xy* band only has a single peak due to the van Hove singularity with a much higher intensity (see Fig. 2.9) than the small split peak at the Fermi level of uniaxially strained Sr_2RuO_4 (see the bottom panel of Fig. 2.7).

2.2 Bandstructure-dependence of renormalization-group prediction on pairing channels

This section is adapted from a preprint, arxiv:1701.07884, which was in collaboration with Dr. Alejandro Federico Rebola, Prof. Craig J. Fennie, and

Prof. Eun-Ah Kim.

As discussed in the previous chapter, recent experimental advances in using strain engineering to significantly alter the band structure of ruthenates offer opportunities and challenges to the weak-coupling renormalization group (RG) analysis for predicting superconducting instabilities in moderately correlated materials with multi bands. On one hand, the RG approach can provide theoretical guidance. On the other hand, it is now imperative to better understand how the predictions of the RG approach depends on the non-universal details of the input microscopic models. Here my collaborators and I focus on the effect of band-selective mass-renormalization, which is often observed in angle resolved photoemission spectroscopy (ARPES) but not captured by density functional theory (DFT) calculations. To demonstrate possible consequences of such effect in RG predictions, I take uniaxially strained Sr_2RuO_4 as an example to carry out weak-coupling RG analyses with two sets of input band structures: one is from DFT calculations done by Alejandro Rebola in Craig Fennie's group, and the other is based on existing ARPES data[17]. Despite good qualitative agreement between the Fermi surfaces of the two sets of band structures, we find their corresponding RG analyses to predict qualitatively different trends in the strain dependence of the superconducting transition temperature T_c as well as the dominant pairing channel. Moreover, only the predicted trend based on the ARPES-based band structure agrees with the recent T_c-measurement on uniaxially strained Sr_2RuO_4. With this example, we want to point out a fact that has been so far under-appreciated by the community: seemingly unimportant quantitative details in the input microscopic model could lead to qualitatively different RG results for systems with more complicated band structures, such as

multi-band materials. We emphasize that extra care is necessary for the input microscopic model in attempts to connect RG predictions with experiments.

2.2.1 Introduction

Strain of magnitude that can significantly alter the band structure of correlated materials recently reached via bulk strain [54, 157] or epitaxial strain[17] now offers a new axis of control beyond traditional means. This new dimension presents both opportunity and challenge for theory. On the bright side, weak-coupling renormalization group (RG) approaches[139, 136, 149, 157, 26] that take the band structure based on microscopic information as starting points can now aspire to guide experimental efforts [60]. Nonetheless, such proximity to reality puts higher bar on the theory. Especially, importance of better understanding the sensitivity of the RG predictions against microscopic details cannot be understated.

Here, we focus on the impact of band-specific mass renormalization that can affect the RG prediction for dominant pairing channel in a qualitative manner. It is well-known that band structures obtained using DFT inaccurately predict bandwidth. In a single-band system, this is often remedied through overall rescaling. Now growing interest in multi-band systems have presented a new challenge: the discrepancy in the band mass, often referred to as "mass renormalization", is often band selective[17]. Under such band-specific mass renormalization there is no simple way to reconcile the discrepancy between the dispersion of density functional theory (DFT) based band structure and that of angle-resolved photoemission spectroscopy (ARPES) measurements, even

when the two band structures exhibit virtually identical Fermi surfaces (FSs). Now the critical question is the possible impact of such mass renormalization in possible superconducting instability. We investigate this issue in the context of strain-dependence of superconducting instability in Sr_2RuO_4.

Partially driven by the fact that Sr_2RuO_4 is the leading candidate material for a two-dimensional (2D) topological superconductor[72, 64, 125, 76, 84, 30, 66], recent strain-engineering efforts and careful study of experimental band structure focused on the material. In particular, Burganov *et al.*[17] reported band-specific mass renormalization. Burganov *et al.* also reported that ruthenate films can undergo Lifshitz transition upon epitaxial biaxial strain of order 1.6%[17, 60]. More recently, Steppke *et al.*[157] found the superconducting transition temperature (T_c) of Sr_2RuO_4 to change upon a bulk compressive uniaxial strain and peak at a certain magnitude [see Fig. 2.11(a)]. They further found that the upper critical field shows a decreased anisotropy at the T_c maximum, which indicates the pairing to become spin-singlet at the point. Nonetheless, the large mass renormalization found in the ARPES data of biaxially strained ruthenates suggests possible discrepancies between the DFT-based band structures and actual band structure under uniaxially strain. In particular, the band-selective mass renormalization in Sr_2RuO_4 was found to be at the order of 30% larger in the quasi-2D band than in the quasi-1D bands depend on the strain magnitude[17].

The purpose of this article is to point out a fact that has been so far underappreciated by the community: the perturbative RG results could be very sensitive to details in the input band structures. This would imply that extra attention is necessary in attempts to connect RG predictions with experiments. To demon-

strate our point, we will take the uniaxially strained Sr_2RuO_4 as an example to contrast the RG results based on the two sets of tight-binding parameters: one obtained from a DFT calculation, and the other from extrapolating the ARPES data in the absence of strain. Then, we will compare the two sets of results to the measured strain-dependent T_c[157].

2.2.2 The model and approach

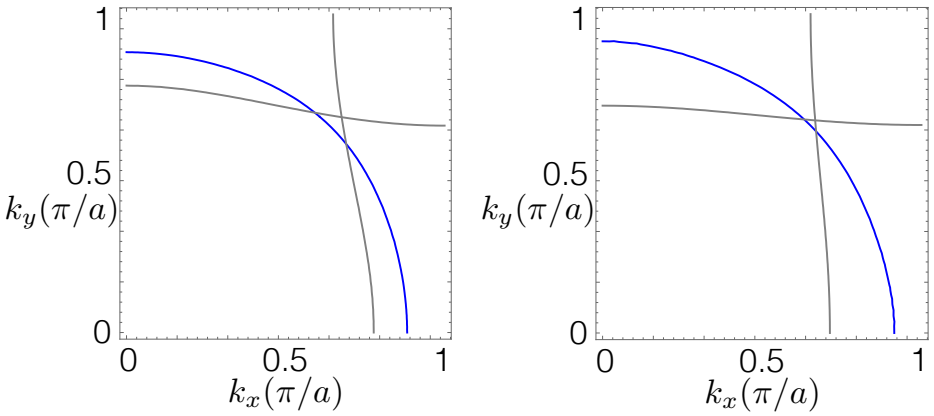

Figure 2.10: The FSs of unstrained Sr_2RuO_4 obtained from the tight-binding model with parametrizations extracted from (a) DFT calculation (b) ARPES measurement.

Our model for the uniaxially strained Sr_2RuO_4 is a three-band Hubbard model derived from the Ru t_{2g} orbitals d_{xz}, d_{yz}, and d_{xy}:

$$H(\epsilon) = \sum_{\vec{k}\alpha\sigma} E^{\alpha}_{\vec{k}}(\epsilon) c^{\dagger}_{\vec{k},\alpha,\sigma} c_{\vec{k},\alpha,\sigma} + U \sum_{i\alpha} n_{i,\alpha,\uparrow} n_{i,\alpha,\downarrow}, \tag{2.6}$$

where $\epsilon < 0$ denotes the compressive uniaxial strain along [100] direction. Here, $\vec{k} = (k_x, k_y)$, $\alpha = xz, yz, xy$, $\sigma = \uparrow, \downarrow$ denote the crystal momentum, the orbital index, and the spin respectively, and $n_{i,\alpha,\sigma} \equiv c^{\dagger}_{i,\alpha,\sigma} c_{i,\alpha,\sigma}$. We employ the following tight-

binding parameterization for intra-orbital kinetic energies:

$$
\begin{aligned}
E^{xz}_{\vec{k}}(\epsilon) &= -2t_x(\epsilon)\cos k_x - 2t^{\perp}_y(\epsilon)\cos k_y - \mu_1(\epsilon) \\
E^{yz}_{\vec{k}}(\epsilon) &= -2t_y(\epsilon)\cos k_y - 2t^{\perp}_x(\epsilon)\cos k_x - \mu_1(\epsilon) \\
E^{xy}_{\vec{k}}(\epsilon) &= -2t'_x(\epsilon)\cos k_x - 2t'_y(\epsilon)\cos k_y \\
&\quad - 4t''(\epsilon)\cos k_x \cos k_y - \mu_2(\epsilon),
\end{aligned}
\tag{2.7}
$$

where we neglect the orbital-mixing terms [4]. The dispersions of the three bands in Eq. (2.7) lead to two quasi-1D FSs comprising the Ru orbitals d_{xz} and d_{yz}, and one quasi-2D FS comprising the Ru orbital d_{xy}. For the bare interaction, we focus on the repulsive intra-orbital on-site repulsion $U > 0$[136] given the experimentally observed unconventional pairing in as-grown Sr_2RuO_4 [64, 125, 76].

Our model above differs from the model in Ref. [157] in that the latter has emphasized the inter-band coupling. Furthermore, starting from their DFT-based band structure, they found the quasi-1D bands to be the leading pairing channels although it is the 2D band that goes through the Lifshitz transition. Therefore, the inter-band repulsion U' of a significant magnitude of $0.84U$ was cruicial for the predominantly 1D-band-driven superconductivity to nevertheless show the experimentally observed peak in T_c as a function of uniaxial strain while the 2D band is closer to the van Hove singularity in the model of Ref. [157]. Here, we focus on the results in the absence of the inter-orbital repulsion U'. Nevertheless, we have checked that the inter-orbital $U' \leq 0.5U$ makes no qualitative difference to the results we report in this paper.

[4] Although Ref. [149] found the spin-orbit coupling to significantly affect the nature and mechanism of pairing in the unstrained system, the van Hove singularities which sit at point $X = (\pi, 0)$ and $Y = (0, \pi)$ lie in the region of the FS where orbital characters are well-defined[146, 72]. Hence, we expect the absence of orbital-mixing terms in our model would not affect our conclusions in a qualitative manner.

Our main concern is the effects on the pairing instability from the mass renormalization, which is often present in measured band structures, despite the calculated and measured FSs could be qualitatively similar [see Fig. 2.10]. Thus in the following, we contrast and compare the RG predictions starting from two sets of tight-binding parameters $E^{\alpha}_{\vec{k}}(\epsilon)$ in Eq. (2.7): 1) the parameters fitted to DFT calculations with varying degree of strain, and 2) the parameters fitted to the available unstrained ARPES data and strained appropriately. For the first set of parameters we performed DFT calculations by fixing the [100] lattice constants to the desired strain value and by letting all internal parameters as well as transverse lattice constant to fully relax. All our DFT calculations were performed with VASP [94, 14], using the PBEsol Exchange-correlation functional, a plane-wave basis cutoff of 520 eV and a 12x12x12 k-point sampling of the Brillouin zone. The band structure thus obtained was then used to fit the tight-binding model in Eq. (2.7).

For the second set of parameters, we use the parameters extracted from the ARPES data of an unstrained Sr_2RuO_4[17] at zero strain $\epsilon = 0$. As no ARPES data is currently available under uniaxial strain $\epsilon < 0$, we determine the tight-binding parameters under strain by extrapolating the unstrained ARPES-extracted parameters. For this, we determine the percentage change of each parameter $p(\epsilon)$ under strain from the first set of DFT-extracted parameters by $p(\epsilon) \equiv t_x^{DFT}(\epsilon)/t_x^{DFT}(0)-1$. We then estimate each strained parameter starting from the ARPES-measured parameter for unstrained system as $t_x(\epsilon) = t_x(0)[1 + p(\epsilon)]$. The key difference between the first and the second set of parameters is the band-selective mass renormalization that has been measured in the ARPES data of Ref. [17] in the absence of strain. Although it is well-known that DFT often underestimates band mass, band-selective mass renormalization in multi-band

system poses challenges that have been under-appreciated. It turns out that the mass renormalization is focused on 2D bands in Sr_2RuO_4, which enhances the density of states of the 2D band at the Fermi level substantially.[17, 60][5]

To study the dominant pairing channels under strain, we then carry out a two-step perturbative RG analysis with the microscopic model being Eq. (2.6) and (2.7) with the two sets of tight-binding parameters. For completeness, we now briefly review the perturbative two-step RG approach[139, 136] we adopt. In the first step, we numerically evaluate the effective pairing vertices in different channels at some intermediate energy scale $E = \Lambda_0$ near the Fermi level by integrating out the higher-energy modes down to Λ_0. Up to the one-loop order, the singlet and triplet effective pairing vertices $\Gamma^{\alpha}_{s/t}(\hat{k}, \hat{k}')$ at energy Λ_0 are related to the repulsive bare interaction U and the non-interacting static particle-hole susceptibilities $\Pi^{\alpha}_{ph}(\vec{q})$ for band α at momentum $\vec{q}$ through

$$\Gamma^{\alpha}_{s}(\hat{k}, \hat{k}') = U + U^2 \Pi^{\alpha}_{ph}(\hat{k} + \hat{k}'), \tag{2.8}$$

and

$$\Gamma^{\alpha}_{t}(\hat{k}, \hat{k}') = -U^2 \Pi^{\alpha}_{ph}(\hat{k} - \hat{k}'), \tag{2.9}$$

where $\hat{k}^{(')}$ are the outgoing (incoming) momenta on the FS of band α. Now, the pairing tendency of band α in the singlet and triplet channels can be quantified by the most negative eigenvalue $\tilde{\lambda}^{\alpha}_{s/t} \equiv \lambda^{\alpha}_{s/t}(E = \Lambda_0)$ of a dimensionless matrix $g^{\alpha}_{s/t}(\hat{k}, \hat{k}')$, which is a product of the density of states ρ^{α} on the Fermi surface of the band α and the normalized effective pairing vertices at the energy scale Λ_0:

$$g^{\alpha}_{s/t}(\hat{k}, \hat{k}') = \rho^{\alpha} \sqrt{\frac{\bar{v_F}^{\alpha}}{v^{\alpha}_F(\hat{k})}} \Gamma^{\alpha}_{s/t}(\hat{k}, \hat{k}') \sqrt{\frac{\bar{v_F}^{\alpha}}{v^{\alpha}_F(\hat{k}')}}. \tag{2.10}$$

[5]Here for the second set of parameters, we have effectively assumed the bias in mass renormalization stays constant as the uniaxial strain increases though the ARPES data is yet not available.

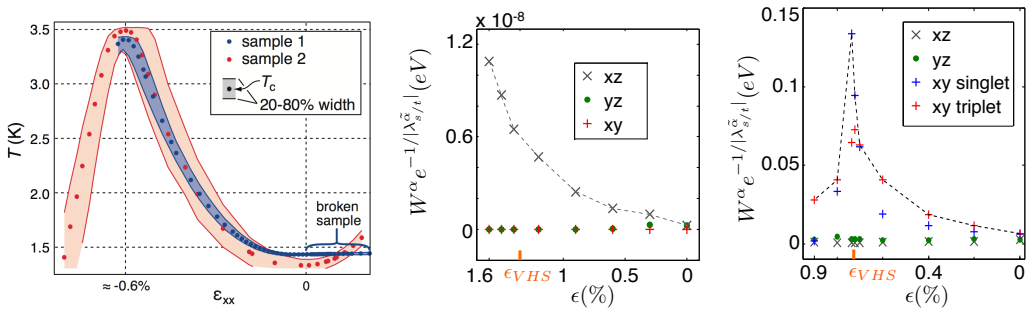

(a) (b) (c)

Figure 2.11: (a) The measured T_c as a function of uniaxial strain presented in Ref. [157]. (b-c) The estimate of $T_c \sim W^\alpha e^{-1/|\tilde{\lambda}^\alpha|}$ for different pairing channels as a function of uniaxial strain with $U = 1$ eV using tight-binding parameters based on (b) the DFT results and (c) the ARPES data. Here, ϵ_{VHS} is the strain amount at which the 2D band FS goes through Lifshitz transition, and the dashed line shows the expected transition temperature T_c.

Here, $v_F^\alpha(\hat{k})$ is the magnitude of Fermi velocity at $\hat{k}$, and $\frac{1}{\bar{v_F}^\alpha} \equiv \int \frac{d\hat{p}}{S_f^\alpha} \frac{1}{v_F^\alpha(\hat{p})}$ with $S_F^\alpha \equiv \int d\hat{p}$ being the FS 'area' of band α. In the second step, we study the evolution of the most negative eigenvalues $\lambda_{s/t}^\alpha(E)$ for different channels $(\alpha, s/t)$ as the energy E lowers from Λ_0 to 0. Given the well-known RG flow for the Cooper instability, $\frac{d\lambda_{s/t}^\alpha}{dy} = -(\lambda_{s/t}^\alpha)^2$ with the RG running parameter being $y \equiv \log(\Lambda_0/E)$[151], we can relate T_c to the critical energy scale at which the most divergent $\lambda_{s/t}^\alpha(y)$ among all channels diverges as[136]

$$T_c \sim W^\alpha e^{-1/|\tilde{\lambda}|}, \tag{2.11}$$

where W^α is the bandwidth of the dominant band α, and $\tilde{\lambda}$ is the most negative $\tilde{\lambda}_{s/t}^\alpha$ among all channels.

2.2.3 Results

Using the first set of tight-binding parameters obtained from DFT, we find the critical energy scale defined in Eq. (2.11) to increase *monotonically* with the compressive uniaxial strain in [100] direction $\epsilon < 0$ [see Fig. 2.11(b)]. This is because the active band is the yz-orbital-based 1D band whose density of states monotonically increase with the compressive strain, as opposed to that of the xy-orbital-based 2D band which peaks at the strain amount ϵ_{VHS}, where the 2D band FS goes through Lifshitz transition. The 1D band dominates over the 2D band despite the fact that the 2D band density of states ρ^{xy} is slightly larger than that of the 1D band ρ^{yz}. This is because the particle-hole susceptibility of the 1D band peaks sharply at $\vec{q} \sim (\pi, 2k_F)$ due to the high degree of nesting. This is a feature shared between our DFT-based band structure and the DFT-based band structure used by Ref. [157]. Similarly, Ref. [157] also found the 1D band to dominate the pairing instability. It was only through a substantial inter-orbital coupling U' could Ref. [157] find the T_c scaling to peak riding on the van Hove singularity touched by the 2D band FS.

By contrast, the T_c calculated using the second set of parameters based on ARPES data peaks as a function of strain even in the absence of any inter-orbital coupling. This is because the 2D band is now the active band due to the mass renormalization which is substantially more severe on the 2D band[17]. Hence, when the 2D FS goes through Lifshitz transition at the strain amount ϵ_{VHS}, T_c peaks [see the dashed line in Fig. 2.11(c)]. Note that in the close vicinity of the van Hove singularity at $(\pm\pi, 0)$, the parity-even singlet dominates over the parity-odd triplet pairing tendency as the latter is expected to be suppressed by

the symmetry[175, 123][6]. Interestingly, the prediction for the peak in T_c and the dominance of the singlet pairing in the close vicinity of the peak agrees with what was observed in the experiment [see Fig. 2.11 (a)]. The fact that key experimental features are robustly reproduced by the RG prediction with a simple model for interactions is rather appealing.

To summarize, we investigated how perturbative RG predictions for superconducting instability depends often on the understated aspects of the band structure beyond Fermi surface. We found that in a multi-band model, balance between mass renormalizations of different bands can change the balance between different pairing channels, and thus the qualitative trends of pairing properties under external knobs. Motivated by recent experimental findings (1) T_c peaking at a finite percentage of uniaxial strain, and (2) singlet pairing near the peak, we investigated the specific example of uniaxially strained Sr_2RuO_4 with two sets of band structures. We found the two band structures to host qualitatively different trends in T_c as a function of strain: while the DFT-based band structure fails to reproduce the observed peak in T_c in the absence of strong inter-orbital interaction[157], the ARPES-based band structure reproduces the observed peak even with a simple Hubbard type model. This shows band-selective mass renormalizations can affect balance between different superconducting channels, hence calls for realistic band-structure information to accompany strain engineering studies.

Acknowledgement – Y-TH was supported by the Cornell Center for Materials Research with funding from the NSF MRSEC program (DMR-1120296)

[6]The triplet tendency is expected to vanish right at ϵ_{VHS} which is not captured in Fig. 2.11(c) because the perturbative RG analysis cannot access the non-perturbative regime.

and E-AK was supported by U.S. Department of Energy, Office of Basic Energy Sciences, Division of Materials Science and Engineering under Award DE-SC0010313. E.-A.K. acknowledges Simons Fellow in Theoretical Physics Award #392182 and thanks hospitality of KITP supported by Grant No. NSF PHY11-25915. AFR and CJF acknowledge support from the NSF grant no. DMR-1056441.

2.3 Topological superconductivity in monolayer transition metal dichalcogenides

This section is adpated from Nature Communication 8, 14985 (2017), which was in collaboration with Dr. Abolhassan Vaezi, Dr. Mark H. Fischer, and Prof. Eun-Ah Kim.

Theoretically it has been known that breaking spin-degeneracy and effectively realizing spinless fermions is a promising path to topological superconductors. Yet, topological superconductors are rare to date. Here, my collaborators and I propose to realize spinless fermions by splitting the spin-degeneracy in the momentum space. Specifically, we identify lightly hole-doped monolayer transition metal dichalcogenide (TMD) semiconductors as candidates for topological superconductors out of such momentum-space-split spinless fermions. Although electron-doped TMDs have recently been found superconducting, the observed superconductivity is unlikely topological due to the near spin-degeneracy. Meanwhile, hole-doped TMDs with momentum-space-split spinless fermions remain unexplored. In this work, I carry out a renormalization group study to predict the dominant pairing

channel in lightly hole-doped monolayer TMDs. By further analyses on the symmetries and topological properties of the dominant pairing channels with the help of Abolhassan Vaezi and Mark Fischer, , I find that the unusual spin-valley locking in hole-doped TMDs together with repulsive interactions selectively favors two topological superconducting states: inter-pocket paired state with Chern number $|C| = 2$ and intra-pocket paired state with finite pair-momentum. A confirmation of our predictions will open up possibilities for manipulating topological superconductors on the device friendly platform of monolayer TMDs.

2.3.1 Introduction

The quest for material realizations of topological chiral superconductors with nontrivial Chern numbers[142, 73, 153, 134] is fueled by predictions of exotic signatures, such as Majorana zero modes and quantized Hall effects. Unfortunately, natural occurrence of bulk topological superconductors are rare with the best candidates being superfluid ^{3}He[168] and Sr_2RuO_4[71]. Instead, much recent experimental progress relied on proximity inducing pairing to a spin-orbit-coupled band structure building on the proposal of Fu and Kane[42]. Their key insight was that a paired state of spinless fermions is bound to be topological and that the surface states of topological insulators are spinless in that the spin-degeneracy is split in position-space (**r**-space): the two degenerate Dirac surface states with opposite spin textures are spatially separated. Nevertheless despite much experimental progress along this direction [185, 147, 165, 170, 24, 171, 173], the confinement of the helical paired state to the interface of the topological insulator and a superconductor limits experimental access to its potentially exotic

properties.

Another type of exotic paired states that desires material realization is the finite-momentum-paired states, which has long been pursued since the first proposals by Fulde and Ferrell[43] and by Larkin and Ovchinnikov[99]. Most efforts towards realization of such modulated superconductors[63, 189], however, relied on generating finite-momentum pairing using spin-imbalance under an (effective) magnetic field in close keeping with the original proposals. Exceptions to such a spin-imbalance-based approach are Ref. [1] and [23] that made use of spinless Fermi surfaces with shifted centers. More recently, there have been proposals suggesting modulated paired states in cuprate high-T_c superconductors[6, 102, 50]. However, unambiguous experimental detection of a purely modulated paired state in a solid-state system is lacking.

We note an alternative strategy that could lead to pairing possibilities for both topological and modulated superconductivity: to split the spin-degeneracy of fermions in momentum-space (**k**-space). This approach is essentially dual to the proposal of Fu and Kane and it can be realized in a time-reversal-invariant non-centrosymmetric system when a pair of Fermi surfaces centered at opposite momenta $\pm\mathbf{k}_0$ consist of oppositely spin-polarized electrons [see Fig. 1(a)]. When such a spin-valley-locked band structure is endowed with repulsive interactions, conventional pairing will be suppressed. Instead, there will be two distinct pairing possibilities: inter-pocket and intra-pocket pairings, where the latter will be spatially modulated with pairs carrying finite center-of-mass momentum $\pm 2\mathbf{k}_0$.

What is critical to the success of this strategy is the materialization of such **k**-space-split spinless fermions. A new opportunity has arisen with the discov-

ery of a family of superconducting two-dimensional (2D) materials, monolayer group-VI transition metal dichalcogenides (TMDs) MX_2 (M = Mo, W, X = S, Se)[177, 67, 152, 22]. Although the transition metal atom M and the chalcogen atom X form a 2D hexagonal lattice within a layer as in graphene, monolayer TMDs differ from graphene in two important ways. Firstly, TMD monolayers are non-centrosymmetric, i.e., inversion symmetry is broken [see Fig. 2.18(b) and (c)]. As a result, monolayer TMDs are direct-gap semiconductors[162] with a type of Dresselhaus spin-orbit coupling[159, 172] referred to as Ising spin-orbit coupling[107]. This spin-orbit-coupled band structure leads to the valley Hall effect[172, 114], which has established TMDs as experimental platforms for pursuing valleytronics applications[172, 20, 115, 68, 114, 113]. Our focus, however, is the fact that there is a sizable range of chemical potential in the valence band that could materialize the **k**-space spin-split band structure we desire [see Fig. 2.18(d)]. Secondly, the carriers in TMDs have strong d-orbital character and hence, correlation effects are expected to be important. Interestingly, both intrinsic and pressure-induced superconductivity has been reported in electron-doped (n-doped) TMDs [177, 67, 152, 22] with the debate regarding the nature of the observed superconducting states still on-going[144, 182, 181, 31, 145].

Here, we propose to obtain **k**-space-split spinless fermions by lightly hole-doping (p-doping) monolayer TMDs such that the chemical potential lies between the two spin-split valence bands. We investigate the possible paired states that can be driven by repulsive interactions[89] in such lightly p-doped TMDs using a perturbative renormalization group (RG) analysis going beyond mean-field theory[182, 154]. We find two distinct topological paired states to be the dominant pairing channels: an inter-pocket chiral (p/d)-wave paired state with Chern number $|C| = 2$ and an intra-pocket chiral p-wave paired state with a

spatial modulation in phase. The degeneracy can be split by the trigonal warping or Zeeman effect.

2.3.2 Results

Spin-valley locked fermions in lightly p-doped monolayer TMDs

The generic electronic structure of group IV monolayer TMDs is shown in Fig. 2.18(d). The system lacks inversion symmetry [see Fig. 2.18(b) and (c)], which leads to a gapped spectrum and a S_z-preserving spin-orbit coupling. Such Ising spin-orbit coupling[107] acts as opposite Zeeman fields on the two valleys that preserves time-reversal symmetry. Furthermore the spin-orbit coupling is orbital-selective[190] and selectively affects the valence band with a large spin-split [159].

By lightly p-doping the TMDs with the chemical potential μ *b*etween the spin-split valence bands, spin-valley locked fermions can be achieved near the two valleys [see Fig. 2.13(a) and (b)]. Assuming negligible trigonal warping at low doping, we can use a single label $\tau = \uparrow, \downarrow$ to denote the valley and the spin. Denoting the momentum measured from appropriate valley centers $\pm\mathbf{K}$ by $\mathbf{q}$, the kinetic part of the Hamiltonian density is

$$H_0^p = \sum_{\mathbf{q},\tau} \left(-\frac{q^2}{2m} - \mu \right) c^\dagger_{\mathbf{q},\tau} c_{\mathbf{q},\tau}, \tag{2.12}$$

where μ is the chemical potential, m is the effective mass of the valence band, and $c_{\mathbf{q},\uparrow} \equiv \psi_{\mathbf{K}+\mathbf{q},\uparrow}$ and $c_{\mathbf{q},\downarrow} \equiv \psi_{-\mathbf{K}+\mathbf{q},\downarrow}$ each annihilates a spin-up electron with momentum $\mathbf{q}$ relative to the valley center $\mathbf{K}$ or a spin-down electron with momentum $\mathbf{q}$ relative to the valley center $-\mathbf{K}$ [see Fig. 2.13(a)]. Hence, the spin-valley locked

two-valley problem is now mapped to a problem with a single spin-degenerate Fermi pocket. Nonetheless, the possible paired states with total spin $\tau_z = \pm 1$ and $\tau_z = 0$ in fact represent the novel possibilities of intra-pocket modulated pairings with total $\tau_z = \pm 1$ and inter-pocket pairing with total $\tau_z = 0$ respectively [see Fig. 2.13(a) and (b)].

Pairing possibilities

To discuss the pairing symmetries of the two pairing possibilities, it is convenient to define the partial-wave channels $\tilde{l}$ with respect to the two valley centers $\pm\mathbf{K}$. Since a total spin $\tau_z = \pm 1$ intra-pocket pair consists two electrons with equal spin, Pauli principle dictates such pairing to be in a state with odd partial wave $\tilde{l}$. Stepping back to microscopics, such pairs carry finite center-of-mass momentum $\pm 2\mathbf{K}$ and form two copies of phase-modulated superconductor[43]. This case may or may not break time-reversal symmetry due to the absence of locking between the $\tilde{l}$s of the two pockets $\tau = \uparrow, \downarrow$. For the total $\tau_z = 0$ inter-pocket pairing, the allowed symmetries of a superconducting state is further restricted by the underlying C_{3v} symmetry of the lattice. In particular, the absence of an inversion center allows the pairing wavefunction in each irreducible representation to be a mixture between parity-even and -odd functions with respect to the Γ point[37]. Specifically, s-wave mixes with f-wave and d-wave mixes with p-wave [see Fig. 2.13(c) and (d)]. Among the irreducible representations of C_{3v}, two fully gapped possibilities are the trivial A_1 representation which amounts to (s/f)-wave pairing ($\tilde{l} = 0$) and a chiral superposition of the two-dimensional E representation which amounts to a mixture of $p \pm ip$ and $d \mp id$ pairing ($|\tilde{l}| = 1$). The mixing implies that the non-topological f-wave channel that is typically dominant in trigonal systems as a way of avoiding repulsive interaction will be blocked together with s-wave by the repulsive interaction in the p-doped TMDs.

Hence it is clear that the pairing instability in $|\tilde{l}| = 1$ channel is all one needs for topological pairing in the p-doped TMDs.

Two distinct topological paired states

To investigate the effects of the repulsive interactions between transition metal *d*-orbitals, we take the microscopic interaction to be the Hubbard interaction, which is the most widely studied pardignamtic model of strongly correlated electronic systems

$$H'(W) = \sum_i U n_{i,\uparrow} n_{i,\downarrow}, \tag{2.13}$$

where W is the ultra-violet energy scale, $U > 0$, and $n_{i,s}$ is the density of electrons with spin s on site i. By now it is well-established that the interaction that is purely repulsive at the microscopic level can be attractive in anisotropic channels for low energy degrees of freedom, i.e., fermions near Fermi surface. The perturbative RG approach has been widely used to demonstrate this principle on various correlated superconductors. For the model of p-doped TMDs defined by Eqs. (2.12) and (2.13), the symmetry-allowed effective interactions at an intermediate energy scale $\Lambda_0 \gtrsim 0$ close to the Fermi level in the Cooper channel (see Supplementary Note 1) would be:

$$H'_{\text{eff}}(\Lambda_0) = \sum_{\mathbf{q},\mathbf{q}',\tau,\tau'} g^{(0)}_{\tau,\tau'}(\mathbf{q},\mathbf{q}') c^\dagger_{\mathbf{q}',\tau} c^\dagger_{-\mathbf{q}',\tau'} c_{-\mathbf{q},\tau'} c_{\mathbf{q},\tau}, \tag{2.14}$$

where $\mathbf{q}$ and $\mathbf{q}'$ are the incoming and outgoing momenta. Now, the remaining task is to derive the effective inter- and intra-pocket interactions $g_{\uparrow,\downarrow}(\mathbf{q},\mathbf{q}')$ and $g_{\uparrow,\uparrow}(\mathbf{q},\mathbf{q}')$ perturbatively in the microscopic repulsion U and check to see if attraction occur in the $|\tilde{l}| = 1$ channel (see Methods and Supplementary Note 2).

Before going into the details of calculation, it is important to note that isotropic pairing with $\tilde{l} = 0$ is forbidden by Pauli principle in the total $\tau_z = \pm 1$ channel and blocked by the bare repulsive interaction in the total $\tau_z = 0$ channel. Hence we need to look for attraction in the anisotropic $\tilde{l} \neq 0$ channel, which is given by the momentum-dependent part of $g^{(0)}_{\tau\tau'}$. With our assumption of isotropic dispersion at low-doping, one needs to go to the two-loop order to find momentum dependence in the effective interaction. Fortunately, it has been known for the model of Eqs. (2.12) and (2.13) that effective attraction is indeed found in anisotropic channels at the two-loop order [27]. Here, we carry out the calculation explicitly (see Methods and Supplementary Note 2) and find the effective interactions in the $|\tilde{l}| = 1$ channel to be attractive, i.e.,

$$\lambda^{(0),|\tilde{l}|=1}_{\tau,\tau'} = \frac{1}{\pi}\int_0^{\pi} d\theta g^{(0)}_{\tau,\tau'}(\theta)\Phi_1(\theta) < 0 \tag{2.15}$$

for $\tau, \tau' = \uparrow, \downarrow$, where $\theta \equiv 2\sin^{-1}(\frac{|\mathbf{q}\pm\mathbf{q}'|}{2q_F})$ is the angle associated with the momentum transfer, and $\Phi_1(\theta) = \sqrt{2}\cos(\theta)$ is the normalized angular-momentum-one eigenstate in 2D.

In the low energy limit, the effective attractions in the $|\tilde{l}| = 1$ channel at the intermediate energy scale Λ_0 in Eq. (2.15) will lead to the following two degenerate topological paired states (see Methods): the inter-pocket (p/d)-wave pairing which is expected to be chiral [see Fig. 2.14(a)] and the modulated intra-pocket pairing [see Fig. 2.14(b)]. The degeneracy is expected for the model of Eqs. (2.12) and (2.13) with its rotational symmetry in the pseudo spin τ. There are two ways this degeneracy can be lifted. Firstly, the trigonal warping will suppress intra-pocket pairing as the two points on the same pocket with opposing momenta will not be both on the Fermi surface any more [see Fig. 2.14(c)]. On the other

hand, a ferromagnetic substrate which will introduce an imbalance between the two pockets which promotes intra-pocket pairing[133] [see Fig. 2.14(d)].

2.3.3 Discussion

The distinct topological properties of the two predicted exotic superconducting states lead to unusual signatures. The inter-pocket $|\tilde{l}| = 1$ paired state [see Fig. 2.14(a)] is topological with Chern number $|C| = 2$ due to the two pockets (see Methods). The Chern number dictates for two chiral edge modes, which in this case are Majorana chiral edge modes each carrying central charge $\frac{1}{2}$[16, 142]. This is in contrast to $d+id$ paired state on a single spin-degenerate pocket which is another chiral superconducting state [140, 121, 78, 12, 38, 79] with four chiral Majorana edge modes. An unambiguous signature of two Majorana edge modes in the inter-pocket chiral $|\tilde{l}| = 1$ paired state will be a quantized thermal Hall conductivity[142] of

$$K_H = c\frac{\pi^2 k_B^2}{3h}T \tag{2.16}$$

at temperature T, where $c = 1$ is the total central charge. Additionally, signatures of the chiral nature of such state could be revealed by a detection of time-reversal symmetry breaking in polar Kerr effect and muon spin relaxation measurements. Finally, a sharp signature of anisotropy of the pairing will be the maximization of the critical current in a direct current superconducting quantum interference device (dc SQUID) interferometry setup of Fig. 2.15(a) at some finite flux $\Phi_{max} \neq 0$.

The intra-pocket $|\tilde{l}| = 1$ paired state [see Fig. 2.14(b)] is not only topological,

but also its phase of the gap is spatially modulated with $e^{i2\mathbf{K}\cdot\mathbf{r}}$ and $e^{-i2\mathbf{K}\cdot\mathbf{r}}$ for spin-up and -down pairs respectively, where $\mathbf{r}$ is the spatial coordinate of the center of mass of the pair (see Supplementary Note 3). Since the gaps on the two pockets are not tied to each other in principle, the system may be either helical respecting time-reversal symmetry ($C = 0$) or chiral ($C = 2$). Either way, there will be a Majorana zero mode of each spin species at a vortex core so long as τ_z is preserved. What makes the intra-pocket paired state distinct from existing candidate materials for topological superconductivity, however, is its spatial modulation. Smoking gun signature of the modulation in phase would be the halved period $\frac{hc}{4e}$ of the oscillating voltage across the dc SQUID setup in Fig. 2.15(b) in flux Φ due to the difference between the pair-momenta on the two sides of the junction. Another signature of the intra-pocket paired state will be the spatial profile of the modulated phase directly detected with an atomic resolution scanning Josephson tunneling microscopy (SJTM)[82, 50].

In summary, we propose the $\mathbf{k}$-space spin splitting as a new strategy for topological superconductivity. Specifically, we predict lightly p-doped monolayer TMDs with their spin-valley-locked band structure and correlations to exhibit topological superconductivity. Of the monolayer TMDs, WSe_2 may be the most promising as its large spin-splitting energy scale[100] allows for substantial carrier density within the spin-valley-locked range of doping[141]. The rationale for the proposed route is to use a lower symmetry to restrict the pairing channel. The merit of this approach is clear when we contrast the proposed setting to the situation of typical spin-degenerate trigonal systems. With a higher symmetry, trigonal systems typically deals with the need for anisotropic pairing due to the repulsive interaction by turning to the topologically trivial f-wave channel [140, 73]. The n-doped TMDs whose low-energy band structure is ap-

proximately spin-degenerate fall into this category. Hence, experimentally realized superconductivity in n-doped systems would likely be topologically trivial even if the superconductivity is driven by the same repulsive interaction we consider here. The predicted topological paired states in p-doped TMDs are a direct consequence of the spin-valley locking which breaks the spin-degeneracy in $\mathbf{k}$ space and creates two species of spinless fermions. Experimental confirmation of the predicted topological superconductivity in p-doped TMDs will open unprecedented opportunities in these highly tunable systems.

2.3.4 Methods

Perturbative renormalization group (RG) calculation

For the RG calculation, we follow the perturbative two-step RG procedure in Ref. [140], which has been used to study superconductivity in systems such as Sr_2RuO_4[137] and generic hexagonal lattices with spin-degeneracy[140]. Taking the Hubbard on-site repulsion in Eq. (2) as the microscopic interaction, the first step is to integrate out higher energy modes and obtain $g^{(0)}_{\tau,\tau'}$ in Eq. (3), the low-energy effective interactions in the Cooper channel at an intermediate energy $\Lambda_0 \gtrsim 0$ close to the Fermi level. The second step is to study the evolution of these effective interactions as the energy flows from Λ_0 to 0, which is governed by the RG equations.

In the first step, we calculate the inter- and intra-pocket effective interactions $g^{(0)}_{\text{inter}}(\mathbf{q},\mathbf{q}') \equiv g^{(0)}_{\tau,\bar{\tau}}(\mathbf{q},\mathbf{q}')$ and $g^{(0)}_{\text{intra}}(\mathbf{q},\mathbf{q}') \equiv g^{(0)}_{\tau,\tau}(\mathbf{q},\mathbf{q}')$ in terms of the incoming and outgoing momenta $\mathbf{q}$ and $\mathbf{q}'$ order by order in U until we obtain attraction in one of them in certain partial-wave channel $\tilde{l}$. Following Ref. [27], we find the

effective interactions to be (see Supplementary Note 2)

$$g^{(0)}_{\text{inter}}(\mathbf{q},\mathbf{q}') \sim C + \frac{m^2U^3}{2\pi^3}\frac{\sqrt{4q_F^2-p'^2}}{2q_F} - \frac{U^3m^2}{64\pi^3}(1-\frac{p^2}{4q_F^2})\log[1-\frac{p^2}{4q_F^2}], \tag{2.17}$$

and

$$g^{(0)}_{\text{intra}}(\mathbf{q},\mathbf{q}') \sim C' - \frac{m^2U^3}{2\pi^3}\frac{\sqrt{4q_F^2-p^2}}{2q_F} - \frac{U^3m^2}{64\pi^3}(1-\frac{p^2}{4q_F^2})\log[1-\frac{p^2}{4q_F^2}], \tag{2.18}$$

where $\mathbf{p} = \mathbf{q} \pm \mathbf{q}'$ is the momentum transfer, $C > 0$ and $C' < 0$ are momentum-independent constants coming from tree level and one-loop order, and the momentum-dependent terms come solely from two-loop order.

Each partial-wave $\tilde{l}$ component is given by the projection of $g^{(0)}_{\text{inter/intra}}(\mathbf{q},\mathbf{q}')$ on to the normalized angular momentum $\tilde{l}$ eigenstate in 2D, $\Phi_{\tilde{l}}(\theta) = \sqrt{2}\cos\tilde{l}\theta$, where $\theta \equiv 2\sin^{-1}(\frac{p}{2q_F})$ is the angle associated with the momentum transfer $\mathbf{p}$. We find

$$\lambda^{(0),\tilde{l}}_{\text{inter/intra}} = \frac{1}{\pi}\int_0^\pi d\theta g^{(0)}_{\text{inter/intra}}(\theta)\Phi_{\tilde{l}}(\theta) = \frac{2\sqrt{2}\alpha}{\pi}\frac{(\pm1)^{\tilde{l}+1}}{1-4\tilde{l}^2} - \frac{\beta}{\sqrt{2}\pi}\frac{H_{1-\tilde{l}}+H_{1+\tilde{l}}+2\log 2-3}{\tilde{l}(1-\tilde{l}^2)}\sin(\tilde{l}\pi), \tag{2.19}$$

where H_n is the n$^{\text{th}}$ harmonic number, and $\alpha \equiv \frac{U^3m^2}{2\pi^3}$ and $\beta \equiv \frac{U^3m^2}{64\pi^3}$ are postive constants related to density of states and interaction strength. Here, terms with α and β come from contributions with one particle-particle and one particle-hole bubble, and two particle-hole bubbles, respectively (see Supplementary Note 2). The α term in $\lambda^{(0),\tilde{l}}_{\text{intra}}$ acquires an extra minus sign on top of $(-1)^{\tilde{l}}$ from the closed fermion loops in Supplementary Fig.1 (3g) and (3h). Meanwhile, the

α term in $\lambda^{(0),\tilde{l}}_{\text{inter}}$ contains an implicit $(-1)^{\tilde{l}}$ factor due to the fact that the outgoing external momenta in Supplementary Fig.1 (3a) and (3b) are exchanged, which is equivalent to setting $\Phi_{\tilde{l}}(\theta) \to \Phi_{\tilde{l}}(\pi - \theta)$.

Note that $\lambda^{(0),\tilde{l}}_{\text{intra}}$ with even $\tilde{l}$s are forbidden since intra-pocket pairs have equal spin, and that $\lambda^{(0),\tilde{l}}_{\text{inter}} = \lambda^{(0),\tilde{l}}_{\text{intra}}$ for odd $\tilde{l}$s since they correspond to the spin-triplet states with $\tau_z = 0$ and ± 1 respectively. While $\lambda^{(0),0}_{\text{inter}} > 0$ as expected from the bare repulsion, the most negative values are $\lambda^{(0),\pm 1}_{\text{inter}} = \lambda^{(0),\pm 1}_{\text{inter}} \sim -0.3\alpha - 0.04\beta < 0$.

In the second step, we derive and solve the RG equations to study the evolutions of the effective interactions $\lambda^{\tilde{l}}_{\text{inter/intra}}(E)$ as the energy E lowers from Λ_0 to 0. Using $\lambda^{(0),\tilde{l}}_{\text{inter/intra}}$ in Eq. (2.19) as the initial values for the RG flows, the channel with the most relevant attraction in the low-energy limit $E \to 0$ is the dominant pairing channel. Under the assumption that the energy contours for $0 < E < \Lambda_0$ are isotropic, different partial-wave components do not mix while the inter- and intra-pocket interactions with the same $\tilde{l}$ can in principle mix. By a procedure similar to that in Ref. [121] and [112], we find the RG equations up to one-loop order to be

$$\frac{d\lambda^{\tilde{l}}_{\text{inter}}}{dy} = -(1 - d_2)(\lambda^{\tilde{l}}_{\text{inter}})^2 \tag{2.20}$$

and

$$\frac{d\lambda^{\tilde{l}}_{\text{intra}}}{dy} = -(d_1 - d_3)(\lambda^{\tilde{l}}_{\text{intra}})^2 - 2d_3(\lambda^{\tilde{l}}_{\text{inter}})^2, \tag{2.21}$$

where the inverse energy scale $y \equiv \Pi^{s\bar{s}}_{pp}(0) \sim \nu_0 \log(\Lambda_0/E)$ is the RG running parameter, $d_1(y) \equiv \frac{\partial \Pi^{ss}_{pp}(\pm 2\mathbf{K})}{\partial y}$, $d_2(y) \equiv \frac{\partial \Pi^{s\bar{s}}_{ph}(\pm 2\mathbf{K})}{\partial y}$, and $d_3(y) \equiv \frac{\partial \Pi^{ss}_{ph}(0)}{\partial y}$. Here, $\Pi^{ss'}_{pp/ph}(\mathbf{k})$ is the non-interacting static susceptibility at momentum $\mathbf{k}$ in the particle-particle

or particle-hole channel defined in Supplementary Note 1. Since the low-energy band structure is well-nested at $\pm 2\mathbf{K}$ in the particle-particle channel, the Cooper logarithmic divergence appears not only at $\mathbf{k} = 0$ but also $\pm 2\mathbf{K}$ (see Supplementary Note 1). Thus, $d_1(y) = 1$. On the other hand, since the low-energy band structure is poorly-nested at any $\mathbf{k}$ in the particle-hole channel and is far from van Hove singularity, the particle-hole susceptibilities do not diverge in the low-energy limit (see Supplementary Note 1). Thus, $d_2(y), d_3(y) \ll 1$ in the low-energy limit $y \to \infty$. Therefore with logarithmic accuracy, the inter- and intra-pocket interactions renormalize independently with the well-known RG equation in the Cooper channel

$$\frac{d\lambda_i^{\tilde{l}}}{dy} = -(\lambda_i^{\tilde{l}})^2 \tag{2.22}$$

with i = inter, intra. The RG flow $\lambda_i^{\tilde{l}}(y) = \frac{\lambda_i^{(0),\tilde{l}}}{1+\lambda_i^{(0),\tilde{l}} y}$ which solves the RG equation shows that the pairing interaction in channel $\tilde{l}$ becomes a marginally relevant attraction only if the initial value $\lambda_i^{(0),\tilde{l}} < 0$. Since we concluded that the most negative initial values occur in the $|\tilde{l}| = 1$ channels for both inter- and intra-pocket interactions in the first step of the RG procedure, we expect degenerate inter- and intra-pocket $|\tilde{l}| = 1$ pairings in the low-energy limit.

The Chern number of inter-pocket paired state

The inter-pocket chiral $|\tilde{l}| = 1$ paired state becomes just a spinful $p + ip$ paired state with total spin $\tau_z = 0$ when we map the spin-valley-locked two-pocket problem to a spin-degenerate singlet-pocket problem. The spinful $p + ip$ pairing comprises two copies of 'spinless' $p + ip$ pairings as the Bogoliubov-de Gennes (BdG) Hamiltonian of the former can be written as

$$H = \sum_{\mathbf{q}} \epsilon_{\mathbf{q}}(c^{\dagger}_{\mathbf{q},\uparrow}c_{\mathbf{q},\uparrow} + c^{\dagger}_{\mathbf{q},\downarrow}c_{\mathbf{q},\downarrow}) + \Delta_{\mathbf{q}}(c^{\dagger}_{\mathbf{q},\uparrow}c^{\dagger}_{-\mathbf{q},\downarrow} + c^{\dagger}_{\mathbf{q},\downarrow}c^{\dagger}_{-\mathbf{q},\uparrow}) + H.c.$$
$$= \sum_{\mathbf{q}}(\epsilon_{\mathbf{q}}c^{\dagger}_{\mathbf{q},+}c_{\mathbf{q},+} + \Delta_{\mathbf{q}}c^{\dagger}_{\mathbf{q},+}c^{\dagger}_{-\mathbf{q},+} + H.c.) + (\epsilon_{\mathbf{q}}c^{\dagger}_{\mathbf{q},-}c_{\mathbf{q},-} - \Delta_{\mathbf{q}}c^{\dagger}_{\mathbf{q},-}c^{\dagger}_{-\mathbf{q},-} + H.c.), \quad (2.23)$$

where the low-energy dispersion $\epsilon_{\mathbf{q}} = -\frac{q^2}{2m} - \mu$, the gap function $\Delta_{\mathbf{q}} \sim q_x \pm iq_y$, and $c_{\mathbf{q},\pm} \equiv (c_{\mathbf{q},\uparrow} \pm c_{\mathbf{q},\downarrow})/\sqrt{2}$. Since a spinless $p+ip$ paired state has Chern number $C = 1$, where $C = \frac{1}{8\pi}\int d^2q\ \hat{\mathbf{m}} \cdot [\partial_{q_x}\hat{\mathbf{m}} \times \partial_{q_y}\hat{\mathbf{m}}]$ with $\hat{\mathbf{m}} = (\mathrm{Re}[\Delta_{\mathbf{q}}],\ \mathrm{Im}[\Delta_{\mathbf{q}}],\ \epsilon_{\mathbf{q}})/\sqrt{\epsilon^2_{\mathbf{q}} + |\Delta_{\mathbf{q}}|^2}$, the $\tau_z = 0$ spinful $p + ip$ paired state in the single-pocket system has $C = 2$. Hence, the inter-pocket chiral $|\tilde{l}| = 1$ pairing in the two-pocket system has $C = 2$ as well.

Data Availability Statement The authors declare that the data supporting the findings of this study are available within the paper and its Supplementary Information file.

Acknowledgements

The authors thank Reza Asgari, Debdeep Jena, Katja Nowak, Grace Xing, K. T. Law, and Andrey Chubukov for helpful discussions. Y.-T.H. and E.-A.K. were supported by the Cornell Center for Materials Research with funding from the NSF MRSEC program (DMR-1120296). E.-A.K. was supported in part by by the National Science Foundation (Platform for the Accelerated Realization, Analysis, and Discovery of Interface Materials (PARADIM)) under Cooperative Agreement No. DMR-1539918. A. V. was supported by Gordon and Betty Moore Foundation and in part by Bethe postdoctoral fellowship. MHF acknowledges support from the Swiss Society of Friends of the Weizmann Institute.

Author Contributions

Y.-T.H. carried out the RG calculations to identify the dominant paired states. Y.-T.H. and A.V. analyzed the topological properties for the paired states. Y.-T.H. and MHF analyzed the pairing symmetries for the paired states. E.-A.K supervised the project and wrote the paper with contributions from Y.-T.H., A.V., and MHF.

* To whom correspondence should be addressed: eun-ah.kim@cornell.edu

Conflict of interest statement

The authors declare no competing financial interests.

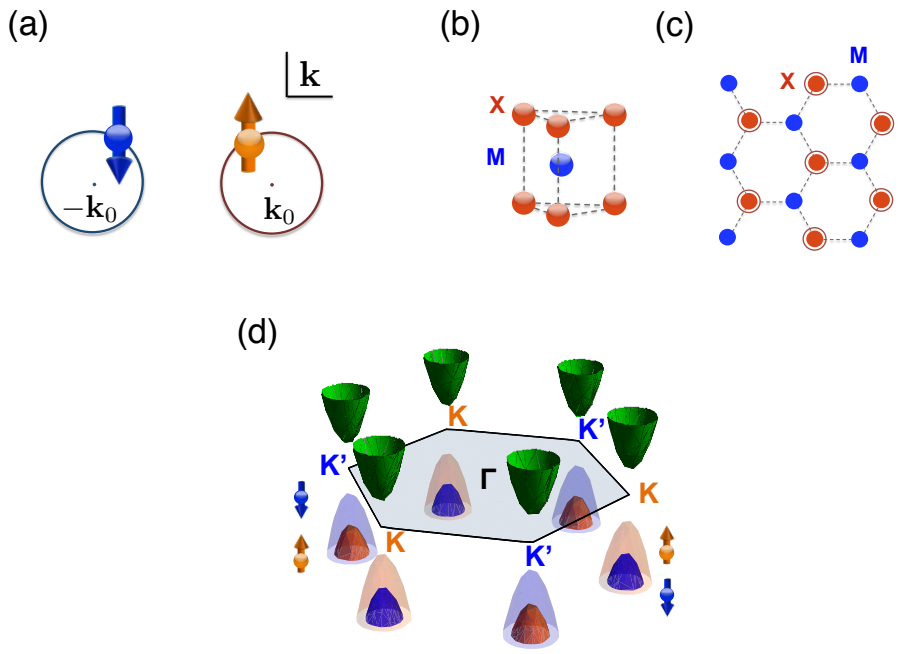

Figure 2.12: **k-space spin-split in the spin-valley-locked band structure of group IV monolayer TMDs.** (a) Schematic Fermi surface hosting **k**-space-split spinless fermions. Here, the two pockets centered at some opposite crystal momenta $\mathbf{k} = \pm\mathbf{k}_0$ host oppositely spin-polarized electrons (represented by the orange and blue arrows) in a time-reversal-symmetric fashion. (b) A sketch for a unit cell of a monolayer TMD. The blue and red spheres represent the transition-metal M atoms and the chalcogen atoms X respectively. (c) A sketch for the top view of the buckled honeycomb lattice of a monolayer TMD. The blue circles represent the transition-metal M atoms and the solid (hollow) red circles represent the chalcogen atoms X above (below) the plane of transition-metal atoms. (d) Schematic low-energy dispersion of a monolayer TMD. The hexagon represents the first Brillouin zone. The green paraboloids represent the nearly spin-degenerate conduction band, and the orange and blue paraboloids represent the spin-split valence bands for the spin-up and -down electrons respectively. This dispersion is time-reversal symmetric since the spin-splits are opposite near the two valleys K and K' which centered at opposite momenta $\pm\mathbf{K}$ with respect to the Γ point.

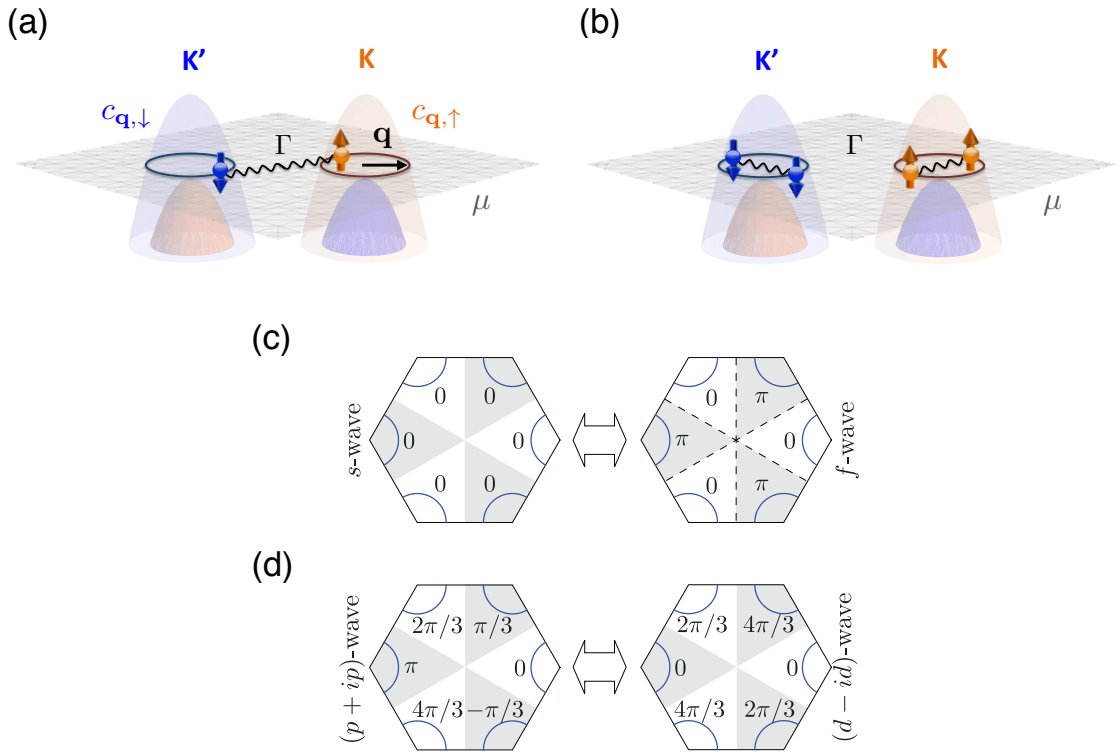

Figure 2.13: **Symmetry-distinct pairing channels in a lightly p-doped monolayer TMD.** The two oppositely spin-polarized Fermi surfaces centered at K and K' valleys (represented by the maroon and blue circles) can develop (a) inter-pocket pairing or (b) intra-pocket pairing. Here, $c_{\mathbf{q},\uparrow}$ ($c_{\mathbf{q},\downarrow}$) denotes the annihilation operator for spin-up (-down) electrons on the pocket at valley K (K'), and $\mathbf{q}$ denotes the momentum relative to the pocket centers. (c) and (d) are candidate gap functions for inter-pocket pairing allowed by the point group C_{3v}. Each hexagon represents the first Brillouin zone where the curves around the corners within the unshaded (shaded) wedges are segments of Fermi surfaces around valley K (K'). Due to the broken C_6 rotations (expressed by the shaded wedges), the gap structures of (c) s-wave and f-wave both belong to the same irreducible representation A_1 and can thus mix. Similarly, the gap structures of (d) p-wave and d-wave both belong to the two-dimensional irreducible representation E and can mix as well. The number in each wedge labels the angle corresponding to the phase of each gap function at the midpoint of the Fermi surface segment in the wedge. Note that the $(p+ip)$- and $(d-id)$-waves have the same phase-winding pattern on each pocket around respective valley centers.

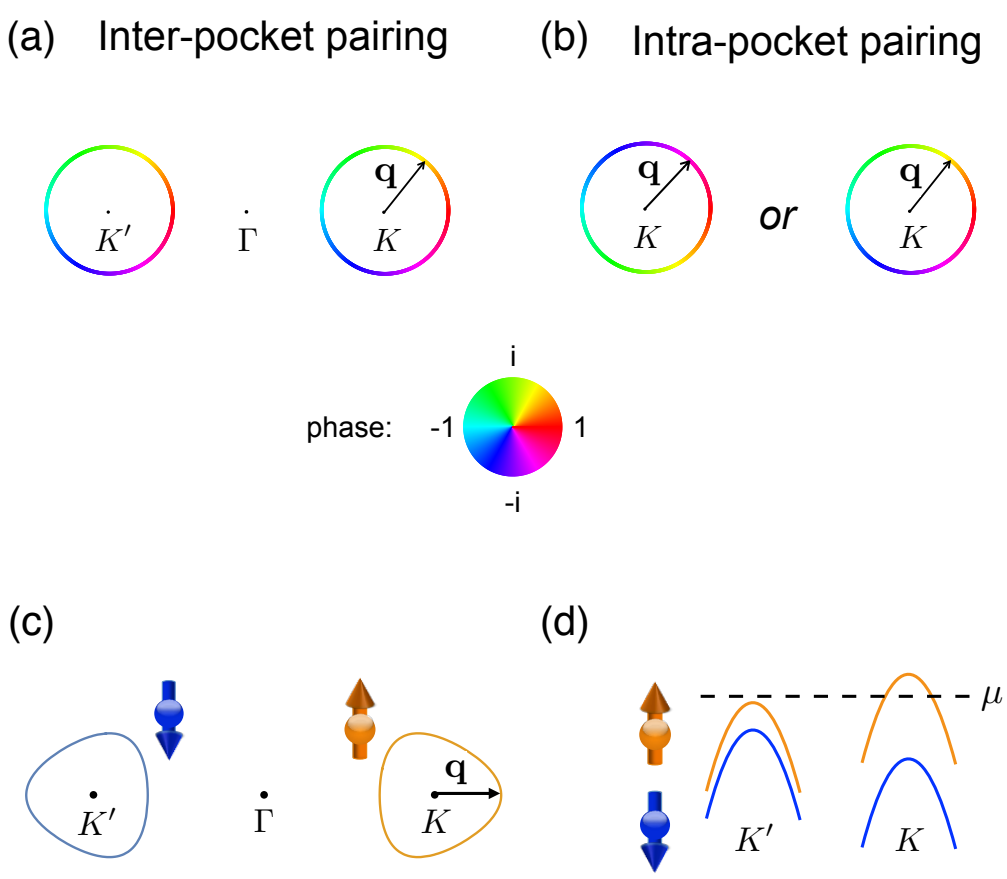

Figure 2.14: **The inter- and intra-pocket $|\tilde{l}| = 1$ paired states.** The gap functions of the $\tilde{l} = \pm 1$ paired states have the approximate form $q_x \pm iq_y$ on the two pockets (represented by hollow circles) centered at $\pm\mathbf{K}$ which we assume to be small and circular as discussed in the text. The color scheme on the circles represents the phase of the gap functions, as indicated by the color wheel. (a) For the inter-pocket pairing case, the phase winding on the two pockets are locked to each other. Overall, the paired state breaks time-reversal symmetry. (b) For the intra-pocket pairing case, each pocket can independently have either $\tilde{l} = 1$ or $\tilde{l} = -1$, which leads to a counterclockwise or clockwise phase winding of 2π. The possible factor and way to tilt the balance between the inter- and intra-pocket pairings: (c) A sketch for the trigonally warped Fermi pockets expected upon a heavier doping where the chemical potential still lies within the spin-split. Such trigonal warping is expected to suppress the intra-pocket pairing as an electron at $\mathbf{q}$ has no pairing partner on the same pocket at $-\mathbf{q}$. (d) The schematic low-energy dispersion near the two valleys for a monolayer TMD grown on a ferromagnetic substrate. As the chemical potential μ (represented by the dashed line) intersects only one band near one valley, the intra-pocket pairing is expected to be promoted.

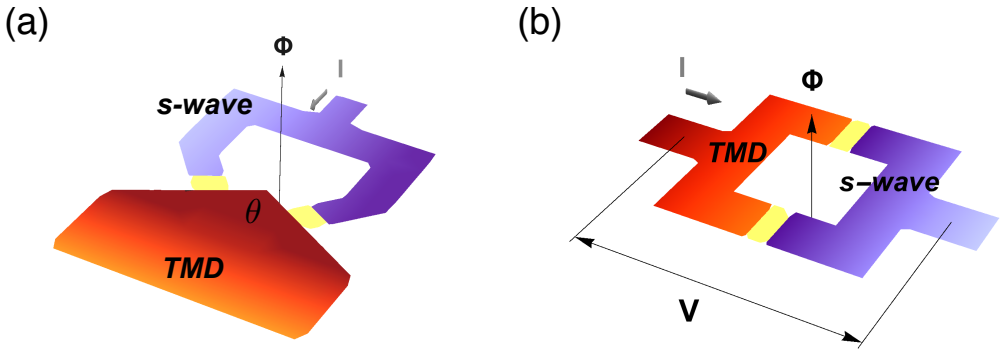

Figure 2.15: **Configurations of possible SQUID experiments for probing the two paired states.** In both (a) and (b), the red and blue parts indicate the lightly p-doped monolayer TMD and a uniform s-wave superconductor respectively, which are connected by two Josephson junctions represented by the yellow strips. I is the applied current and Φ is the magnetic flux through the loop. (a) shows the proposed dc SQUID interferometer set-up which can detect the anisotropy of the inter-pocket pairing symmetry. The flux-dependence of the critical current is expected to be insensitive and sensitive to the angle θ between the edges connected to the two junctions for isotropic and anisotropic pairing respectively. (b) shows the proposed dc SQUID interferometer set-up which can probe the finite pair-momentum of the intra-pocket pairs for the $C = 0$ case. The TMD is oriented in the direction such that the phase of the pairing wavefunction is spatially modulated along the junction. The period in flux Φ of the modulated voltage V across the SQUID loop is expected to be halved into $\frac{hc}{4e}$ since the difference between the pair-momenta on the two sides of a junction requires simultaneous tunneling of a spin-up and a spin-down intra-pocket pair, each carrying pair-momentum $2\mathbf{K}$ and $-2\mathbf{K}$, into the uniform superconductor.

2.3.5 Supplementary Note 1: Why only pairing instabilities?

In this work we consider only pairing instabilities but not particle-hole instabilities, e.g. spin density waves. In the following, we explain why the pairing instabilities are expected to dominate over particle-hole instabilities in the low energy limit. Whether instabilities in particle-hole channel or particle-particle (pairing) channel dominate depends on which of the non-interacting static susceptibilities in particle-hole channel $\Pi_{ph}(\mathbf{p})$ and particle-particle channel $\Pi_{pp}(\mathbf{p})$ diverges faster as approaching the low energy limit. These susceptibilities of electrons with spin s and low-energy dispersion $\epsilon^s(\mathbf{k})$ have the form

$$\Pi_{pp}^{ss'}(\mathbf{p}) \equiv \sum_n \int \frac{d^2k}{4\pi^2} G^s(i\omega_n, \mathbf{k}) G^{s'}(-i\omega_n, -\mathbf{k}+\mathbf{p}) = \int \frac{d^2k}{(2\pi)^2} \frac{1 - f(\epsilon^s_{-\mathbf{k}+\mathbf{p}}) - f(\epsilon^{s'}_{\mathbf{k}})}{\epsilon^s(-\mathbf{k}+\mathbf{p}) + \epsilon^{s'}(\mathbf{k})} \tag{2.24}$$

and

$$\Pi_{ph}^{ss'}(\mathbf{p}) \equiv -\sum_n \int \frac{d^2k}{4\pi^2} G^s(i\omega_n, \mathbf{k}) G^{s'}(i\omega_n, \mathbf{k}+\mathbf{p}) = -\int \frac{d^2k}{(2\pi)^2} \frac{f(\epsilon^s_{\mathbf{k}+\mathbf{p}}) - f(\epsilon^{s'}_{\mathbf{k}})}{\epsilon^s(\mathbf{k}+\mathbf{p}) - \epsilon^{s'}(\mathbf{k})}, \tag{2.25}$$

where spin $s, s' = \uparrow / \downarrow$, ω_n is the fermionic Matsubara frequency, $\mathbf{k}$ and $\mathbf{p}$ are momenta, $G^s(i\omega_n, \mathbf{k}) = \frac{1}{i\omega_n - \epsilon^s(\mathbf{k})}$ is the non-interacting Green's function, and $f(\epsilon^s_{\mathbf{k}})$ is the Fermi function at temerature T.

In general, $\Pi_{pp}^{ss'}(\mathbf{p})$ always diverges logarithmically at total-momentum $\mathbf{p} = 0$ despite the low-energy dispersion $\epsilon^s_{\mathbf{k}}$, which indicates pair-momentum 0 superconductivity if dominates. On the other hand, $\Pi_{ph}^{ss'}(\mathbf{p})$ typically diverges at momentum-transfer $\mathbf{p} = 0$ when the density of states diverges, i.e. near the van Hover singularity, or at some finite momentum-transfer $\mathbf{p} = \mathbf{Q}$ when the Fermi surface is nested in the particle-hole channel at $\mathbf{Q}$. The former and latter indicate instabilities such as ferromagnetism and density-waves respectively when they each dominates. In a two-pocket system, this requires a hole and an elec-

tron pocket to have the same low-energy dispersion (but opposite in energy). In the case where susceptibilities in the two channels diverge equally fast, one needs to further compare their corresponding driving interactions to determine the dominant instability.

In the current lightly p-doped monolayer TMD case, note that both pockets are hole pockets though they have the same low-energy dispersion $\epsilon^{\uparrow}(\mathbf{k}) = -\frac{(\mathbf{k}-\mathbf{K})^2}{2m}$ and $\epsilon^{\downarrow}(\mathbf{k}) = -\frac{(\mathbf{k}+\mathbf{K})^2}{2m}$ with respect to their own valley centers $\mathbf{K}$ and $-\mathbf{K}$ upon low-doping. Thus, the Fermi surface is in fact poorly nested at $2\mathbf{K}$ in the particle-hole channel. To be precise, since $\epsilon^{\downarrow}(\mathbf{p}) = \epsilon^{\uparrow}(\mathbf{p} + 2\mathbf{K})$, the particle-hole susceptibility has the relation

$$\Pi_{ph}^{s\bar{s}}(2\mathbf{K}+\mathbf{p}) = -\int \frac{d^2k}{4\pi^2} \frac{f^{s}_{\mathbf{k}+2\mathbf{K}+\mathbf{p}} - f^{\bar{s}}_{\mathbf{p}}}{\epsilon^{s}(\mathbf{k}+2\mathbf{K}+\mathbf{p}) - \epsilon^{\bar{s}}(\mathbf{k})} = -\int \frac{d^2k}{4\pi^2} \frac{f^{\bar{s}}_{\mathbf{k}+\mathbf{p}} - f^{\bar{s}}_{\mathbf{k}}}{\epsilon^{\bar{s}}(\mathbf{k}+\mathbf{p}) - \epsilon^{\bar{s}}(\mathbf{k})} = \Pi_{ph}^{\bar{s}\bar{s}}(\mathbf{p}) \tag{2.26}$$

for $s = \uparrow$ and $\bar{s} = -s$. Thus,

$$\Pi_{ph}^{s\bar{s}}(\pm 2\mathbf{K}) = \Pi_{ph}^{ss}(0) \sim \nu_0 \tag{2.27}$$

is not diverging in the low energy limit as long as the density of states on the Fermi surface ν_0 is finite. Therefore, we do not consider particle-hole susceptibilities in this work.

On the other hand, since the Fermi surface is perfectly nested at $2\mathbf{K}$ in the particle-particle channel, the particle-particle susceptibility

$$\Pi_{pp}^{s\bar{s}}(0) = \Pi_{pp}^{ss}(\pm 2\mathbf{K}) \sim \nu_0 \mathrm{Log}(\frac{\Lambda}{E}) \tag{2.28}$$

diverges logarithmically as approaching the low-energy limit $E \to 0$ with Λ being the UV cutoff scale. Note that the Cooper logarithmic divergence does not occur only at the usual $\mathbf{p} = 0$, but also at $\mathbf{p} = 2\mathbf{K}$. This indicates that the superconductivity with pair momentum 0 (spatially uniform) and $2\mathbf{K}$ (spatially

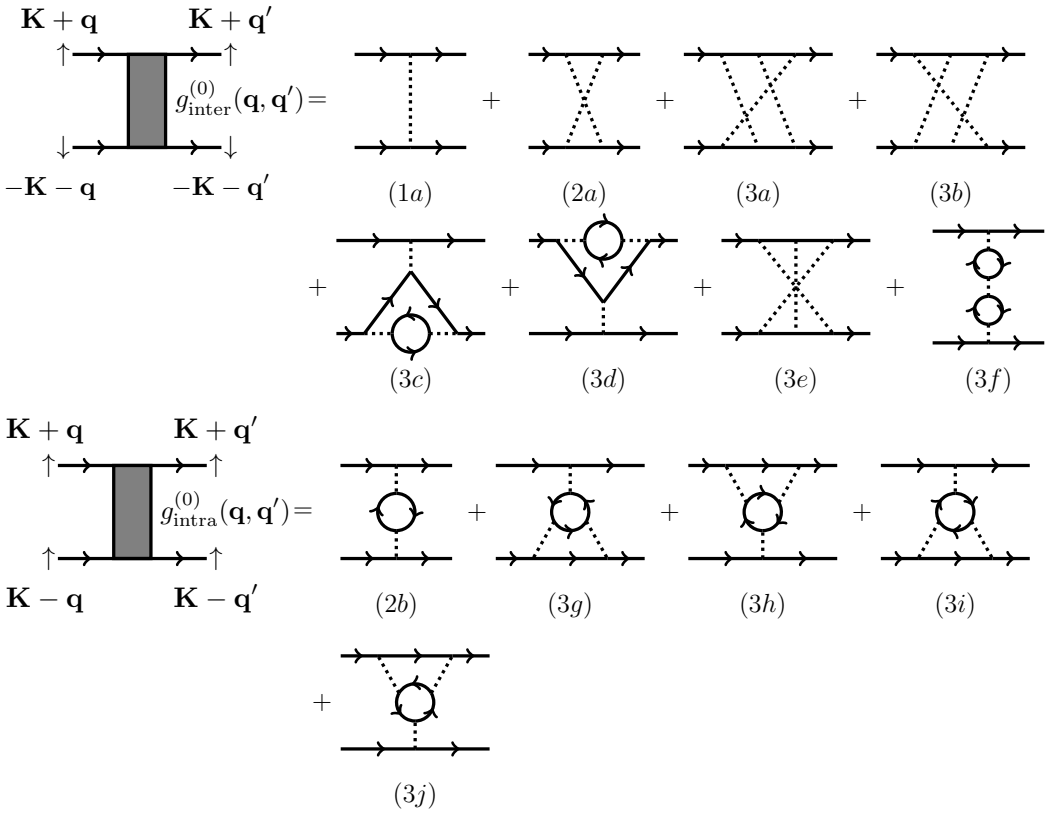

Figure 2.16: Feymann diagrams for the contributions up to two-loop order to the inter- and intra-pocket effective interactions $g^{(0)}_{\text{inter/intra}}(\mathbf{q},\mathbf{q}')$ at the intermediate energy scale $E = \Lambda_0$. The solid and dotted lines represent fermions and repulsive Hubbard interaction U respectively.

modulated at $2\mathbf{K}$) could be equally dominant in the low energy. To determine which is truly more dominant, we need to study their pairing interactions using the RG analysis in the following subsection.

2.3.6 Supplementary Note 2: Inter- and intra-pocket effecitve interactions

We will calculate the inter- and intra-valley effective interactions $g^{(0)}_{\text{inter}}(\mathbf{q},\mathbf{q}') \equiv g^{(0)}_{\tau,\bar{\tau}}(\mathbf{q},\mathbf{q}')$ and $g^{(0)}_{\text{intra}}(\mathbf{q},\mathbf{q}') \equiv g^{(0)}_{\tau,\tau}(\mathbf{q},\mathbf{q}')$ at energy Λ_0 in terms of the incoming and outgoing momenta $\mathbf{q}$ and $\mathbf{q}'$ order by order in U until we obtain attraction in one of them in certain partial-wave channel $\tilde{l}$. Before we start, notice that by omitting the valley index, which is inter-locked with the spin index τ for the low-energy fermions, the inter- and intra-valley interactions in the spin-valley locked two-pocket picture are just the opposite- and equal-spin interactions in a spin-degenerate single-pocket picture. Fortunately, Ref. [27] has already studied the pairing problem in a spin-degenerate single-pocket system under repulsive Hubbard interaction described by Eq. (1) and Eq. (2). Thus, we expect the same result as Ref. [27], i.e. the largest attraction occuring in the angular-momentum-one channel, but with a different physical meaning when mapping back to the spin-valley locked two-pocket picture. To make the mapping between the two pictures explicit, we will follow Ref. [27] to calculate $g^{(0)}_{\text{inter}}(\mathbf{q},\mathbf{q}')$ and $g^{(0)}_{\text{intra}}(\mathbf{q},\mathbf{q}')$ in the two-pocket picture and denote the spin s and valley $\pm\mathbf{K}$ separately.

2.1 Tree level

At the tree level, the on-site repulsion $U > 0$ only contribute to the inter-pocket interaction because U acts between only electrons with opposite spins

due to Pauli exclusive principle. Thus,

$$g^{(0),1}_{\text{inter}}(\mathbf{q}, \mathbf{q}') = U \tag{2.29}$$

with the superscript 1 denoting the tree-level contribution [see Supplementary Fig. 2.16(1a)]. This bare repulsion contributes to only the $\tilde{l} = 0$ component of $g^{(0)}_{\text{inter}}$ because U is independent of the incoming and outgoing momenta $\mathbf{q}$ and $\mathbf{q}'$. Since this is a perturbative analysis, the inter-pocket $\tilde{l} = 0$ pairing is suppressed regardless what the higher order contributions to $\tilde{l} = 0$ channel are. To have any finite contribution to aisotropic channels ($\tilde{l} \neq 0$) requires momentum-dependence from loop corrections.

2.2 Second order

The U^2 (one-loop) order contributions to inter- and intra-pocket interactions are

$$g^{(0),2}_{\text{inter}}(\mathbf{q}, \mathbf{q}') = U^2 \Pi^{s\bar{s}}_{ph}(\pm\mathbf{Q} + \mathbf{q} + \mathbf{q}'), \tag{2.30}$$

and

$$g^{(0),2}_{\text{intra}}(\mathbf{q}, \mathbf{q}') = -U^2 \Pi^{ss}_{ph}(\mathbf{q} - \mathbf{q}') \tag{2.31}$$

respectively for $s = \uparrow / \downarrow$, where the superscript 2 denotes corrections from the second order [see Supplementary Fig. 2.16(2a) and (2b)]. The particle-hole susceptibilies defined in Supplementary Eq. (2.25) can be calculated as

$$\Pi^{ss}_{ph}(\mathbf{p}) = \frac{m}{2\pi^2} \int_{-\pi/2}^{\pi/2} d\phi \int_{k_2}^{k_1} dk \frac{k}{kp\cos\phi} = \frac{m}{2\pi} = \Pi^{\bar{s}s}_{ph}(\mathbf{p}) \tag{2.32}$$

where $k_{1/2} \equiv \pm\frac{p}{2}\cos\phi + \frac{\sqrt{4q_F^2 - p^2\sin^2\phi}}{2}$. Thus, the one-loop corrections are still momentum-independent and contribute to only the $\tilde{l} = 0$ channel. This is a

consequence of isotropic parabolic dispersion in 2D[27, 140]. Note that though $g_{\text{intra}}^{(0),2}$ seems to imply $\tilde{l} = 0$ intra-pocket pairing, pairings in even $\tilde{l}$ channels are not allowed since these are equal-spin pairs. Thus, if either the inter- or intra-pocket pairing were to occur at all, the effective attraction has to come from at least two-loop order.

2.3 Third order

The U^3 (two-loop) contribution of short-range repulsion for a spin-degenerate rotational-invariant 2D system with a single pocket and parabolic dispersion has been proven to facilitate p-wave (angular momentum 1) pairing[27]. Since both pockets in p-doped TMDs have the same low-energy effective dispersion which is parabolic upon light doping, we can map this spin-valley locked two-pocket system to the spin-degenerate single-pocket system studied in Ref. [27] by bringing the pocket centers K and K′ both to $\mathbf{k} = 0$. Thus, we expect to obtain the largest attractions in the partial-wave channel $\tilde{l} = 1$ as well, but the partial-wave channels here are with respect to K and K′ instead of Γ. This indicates degenerate inter- and intra-pocket pairings with $\tilde{l} = 1$ after we map back to the two-pocket system. In the following, we will show the calculations of $g_{\text{intra/inter}}^{(0)}$ following Ref. [27] to comfirm our expectation.

From the corresponding diagrammatic expressions shown in Supplementary Fig. 2.16(3a)-(3j), we can see that the two-loop contributions can be divided into two groups: the ones with one particle-particle and one particle-hole bubble (diagram 3a, 3b, 3g and 3h), and the ones with two particle-hole bubbles (diagram 3c, 3d, 3e, 3f, 3i, and 3j). We first calculate the former contributions to

intra-pocket interaction, i.e. diagram (3g) and (3h). In the static limit,

$$
\begin{aligned}
g^{pp}_{\text{intra}}(\mathbf{q},\mathbf{q}') &= g_{3g}(\mathbf{q},\mathbf{q}') + g_{3h}(\mathbf{q},\mathbf{q}') \\
&= -U^3 \sum_{n,\tilde{n}} \int \frac{d^2l}{4\pi^2} \int \frac{d^2\tilde{l}}{4\pi^2} G^{\uparrow}(i\omega_{\tilde{n}},\tilde{\mathbf{l}}) G^{\downarrow}(-i\omega_{\tilde{n}},-\tilde{\mathbf{l}}+\mathbf{t}_+) G^{\downarrow}(i\omega_n,\mathbf{l}+\frac{\mathbf{p}}{2}) G^{\downarrow}(i\omega_n,\mathbf{l}-\frac{\mathbf{p}}{2}) \\
&+ (\mathbf{t}_+ \to \mathbf{t}_-)
\end{aligned} \tag{2.33}
$$

where $\omega_{n(\tilde{n})}$ is the fermionic Matsubara frequency, $G^s(i\omega_n,\mathbf{l}) = \frac{1}{i\omega_n - \epsilon^s(\mathbf{l})}$ is the non-interacting Green's function, $\mathbf{t}_\pm \equiv \mathbf{l} \pm \frac{\mathbf{q}+\mathbf{q}'}{2}$, $\mathbf{p} \equiv \mathbf{q}' - \mathbf{q}$, and $\mathbf{q}$ and $\mathbf{q}'$ are the external incoming and outgoing momenta relative to the valley center $\mathbf{K}$. As the electrons have energy $E = \Lambda_0 \gtrsim 0$, $|\mathbf{q}| = |\mathbf{q}'| \sim q_F$ with q_F being the Fermi momentum of a single pocket. The over-all minus sign results from the closed fermion loop. The particle-particle loop integral can be calculated as

$$
\begin{aligned}
&\sum_{\tilde{n}} \int \frac{d^2\tilde{l}}{4\pi^2} G^{\uparrow}(i\omega_{\tilde{n}},\tilde{\mathbf{l}}) G^{\downarrow}(-i\omega_{\tilde{n}},-\tilde{\mathbf{l}}+\mathbf{t}_+) = \int \frac{d^2\tilde{l}}{4\pi^2} \frac{1-f(\epsilon^{\uparrow}_{\tilde{\mathbf{l}}}) - f(\epsilon^{\downarrow}_{-\tilde{\mathbf{l}}+\mathbf{t}_+})}{\epsilon^{\uparrow}_{\tilde{\mathbf{l}}} + \epsilon^{\downarrow}_{-\tilde{\mathbf{l}}+\mathbf{t}_+}} = \int \frac{d^2\tilde{l}}{4\pi^2} \frac{1-f(\epsilon^{\uparrow}_{\tilde{\mathbf{l}}}) - f(\epsilon^{\uparrow}_{\tilde{\mathbf{l}}-\mathbf{t}_+})}{\epsilon^{\uparrow}_{\tilde{\mathbf{l}}} + \epsilon^{\uparrow}_{\tilde{\mathbf{l}}-\mathbf{t}_+}} \\
&= -2m \int \frac{d^2\tilde{l}}{4\pi^2} \frac{1-f(\epsilon^{\uparrow}_{\tilde{\mathbf{l}}+\mathbf{K}+\frac{\mathbf{t}_+}{2}}) - f(\epsilon^{\uparrow}_{\tilde{\mathbf{l}}+\mathbf{K}-\frac{\mathbf{t}_+}{2}})}{(\tilde{\mathbf{l}}+\frac{\mathbf{t}_+}{2})^2 + (\tilde{\mathbf{l}}-\frac{\mathbf{t}_+}{2})^2 - 2q_F^2} = -\frac{2m}{4\pi^2} \int_{-\pi/2}^{\pi/2} d\tilde{\phi} \left(\int_0^{\tilde{l}_2} - \int_{\tilde{l}_1}^{r_0^{-1}} \right) d\tilde{l} \frac{\tilde{l}}{\tilde{l}^2 + \frac{t_+^2}{4} - q_F^2} \\
&\sim -\frac{m}{2\pi} (\ln[\frac{t_+^2}{q_F^2}] + c_0)
\end{aligned} \tag{2.34}
$$

assuming $t_\pm \ll 2q_F$, which is the regime where the main momentum-dependence comes from[27]. Here, $\tilde{\phi}$ is the angle between the loop momentum $\tilde{\mathbf{l}}$ and $\mathbf{t}_+$, r_0^{-1} the UV cutoff for momentum integral, $\tilde{l}_{1/2} \equiv \pm\frac{t_+\cos\tilde{\phi}}{2} + \frac{t_+}{2}\sqrt{\frac{4q_F^2}{t_+^2} - \sin^2\tilde{\phi}}$, and c_0 contains terms independent of $\mathbf{t}_\pm$. We will drop c_0 in the following since our purpose is to obtain the momentum-dependent part. Plugging Supplementary Eq. (2.34) back to Supplementary Eq. (2.33), we obtain the second loop

integral

$$
\begin{aligned}
g^{pp}_{\text{intra}}(\mathbf{q},\mathbf{q}') &= \frac{+mU^3}{2\pi}\sum_n \int \frac{d^2l}{4\pi^2}\ln[\frac{t_+^2 t_-^2}{q_F^4}]G^{\downarrow}(i\omega_n,\mathbf{l}+\frac{\mathbf{p}}{2})G^{\downarrow}(i\omega_n,\mathbf{l}-\frac{\mathbf{p}}{2}) \\
&= \frac{-2m^2U^3}{2\pi}\int \frac{d^2l}{4\pi^2}\ln[\frac{t_+^2 t_-^2}{q_F^4}]\frac{f_{\mathbf{l}+\frac{\mathbf{p}}{2}}-f_{\mathbf{l}-\frac{\mathbf{p}}{2}}}{(\mathbf{l}+\frac{\mathbf{p}}{2})^2-(\mathbf{l}-\frac{\mathbf{p}}{2})^2} \\
&\sim \frac{-m^2U^3}{4\pi^3}\int_0^{\pi/2}\frac{d\phi}{\cos\phi}\int_{\bar{l}_2}^{\bar{l}_1} d\bar{l}\ln[(\bar{l}^2-\epsilon^2)^2+4\epsilon^2\bar{l}^2\cos^2\phi] \qquad (2.35)
\end{aligned}
$$

where ϕ is the angle between $\mathbf{p}$ and $\mathbf{l}$, $\epsilon^2 \equiv \frac{4q_F^2-p^2}{p^2}$, $\bar{l} \equiv \frac{2l}{p}$, and $\bar{l}_{1/2} \equiv \pm\cos\phi + \sqrt{\epsilon^2+\cos^2\phi}$. Here, $\epsilon \ll 1$ is a small parameter as we assumed $t_+/q_F \ll 1$ in the first loop, which corresponds to the regime where the external momenta statisfy $p \sim 2q_F$ and the loop momentum $l/q_F \sim \bar{l} \ll 1$. Notice that the integral is dominated by the regime of ϕ where $\cos\phi = O(\epsilon)$ is another small parameter besides ϵ. Since we are interested in the portion of scattering amplitude which depends on the external momenta, we will calculate $g^{pp}_{\text{intra}}(\mathbf{q},\mathbf{q}') - g^{pp}_{\text{intra}}(p=2q_F)$ up to the leading order in the small parameters ϵ and $\cos\phi$. By keeping the small parameters in the upper and lower limits $\bar{l}_{1/2}$ while dropping those in the slowly varying logarithmic integrand, we obtain

$$
g^{pp}_{\text{intra}}(\mathbf{q},\mathbf{q}') - g^{pp}_{\text{intra}}(p=2q_F) \sim -\frac{m^2U^3}{4\pi}\frac{\sqrt{4q_F^2-p^2}}{2q_F} \qquad (2.36)
$$

for the regime of external momenta satisfying $\epsilon \ll 1$.

The two-loop contributions to intra-pocket interaction involving only particle-hole bubbles, i.e. diagram (3i) and (3j), can be calculated in a similar way. In the same regime where the external momenta satisfy $\epsilon \ll 1$, we obtain

$$
\begin{aligned}
g^{ph}_{\text{intra}}(\mathbf{q},\mathbf{q}') &= g_{3i}(\mathbf{q},\mathbf{q}') + g_{3j}(\mathbf{q},\mathbf{q}') \\
&\propto -\frac{U^3m^2}{64\pi^3}(1-\frac{p^2}{4q_F^2})\log[1-\frac{p^2}{4q_F^2}], \qquad (2.37)
\end{aligned}
$$

where the minus sign is due to the closed fermion loop.

We then turn to the inter-pocket interaction. Among all the third-order contributions to $g^{(0)}_{\text{inter}}$, diagram (3e) and (3f) in Supplementary Fig. 2.16 are both just the product of two second-order corrections and do not contribute to momentum-dependence. Thus, we will focus only on diagram (3a)~ (3d). Note that similar to the case of intra-pocket interaction, diagram (3a) and (3b) involve vertex corrections from one particle-particle and one particle-hole bubble just like (3g) and (3h), while diagram (3c) and (3d) involve corrections from two particle-hole bubbles just like (3i) and (3j). Thus, diagram (3a) and (3b) have similar amplitudes as diagram (3c) and (3d) except the momentum-transfer in the particle-hole bubble and the absence of closed fermion loop:

$$g^{pp}_{\text{inter}}(\mathbf{q},\mathbf{q}') - g^{pp}_{\text{inter}}(p = 2q_F) \sim \frac{m^2U^3}{4\pi}\frac{\sqrt{4q_F^2 - p'^2}}{2q_F}, \tag{2.38}$$

where $\mathbf{p}' \equiv \mathbf{q}' + \mathbf{q}$. On the other hand, diagram (3c) and (3d) have the same amplitudes as diagram (3i) and (3j) such that

$$g^{ph}_{\text{inter}}(\mathbf{q},\mathbf{q}') = g_{3c}(\mathbf{q},\mathbf{q}') + g_{3d}(\mathbf{q},\mathbf{q}') \propto -\frac{U^3m^2}{64\pi^3}(1 - \frac{p^2}{4q_F^2})\log[1 - \frac{p^2}{4q_F^2}] \tag{2.39}$$

in the regime where ϵ is small. After collecting all the contributions, the U^3 corrections to the effective inter- and intra-pocket interactions at $E = \Lambda_0$ read

$$\begin{aligned} g^{(0),3}_{\text{inter}}(\mathbf{q},\mathbf{q}') &= g^{pp}_{\text{inter}}(\mathbf{q},\mathbf{q}') + g^{ph}_{\text{inter}}(\mathbf{q},\mathbf{q}') \\ &\sim \frac{m^2U^3}{2\pi^3}\frac{\sqrt{4q_F^2 - p'^2}}{2q_F} - \frac{U^3m^2}{64\pi^3}(1 - \frac{p^2}{4q_F^2})\log[1 - \frac{p^2}{4q_F^2}] \end{aligned} \tag{2.40}$$

and

$$\begin{aligned} g^{(0),3}_{\text{intra}}(\mathbf{q},\mathbf{q}') &= g^{pp}_{\text{intra}}(\mathbf{q},\mathbf{q}') + g^{ph}_{\text{intra}}(\mathbf{q},\mathbf{q}') \\ &\sim -\frac{m^2U^3}{2\pi^3}\frac{\sqrt{4q_F^2 - p^2}}{2q_F} - \frac{U^3m^2}{64\pi^3}(1 - \frac{p^2}{4q_F^2})\log[1 - \frac{p^2}{4q_F^2}]. \end{aligned} \tag{2.41}$$

In summary, we have derived the effective inter- and intra-pocket interactions at $E = \Lambda_0$ from the bare repulsion $U > 0$ up to two-loop order:

$$g^{(0)}_{\text{inter}}(\mathbf{q}, \mathbf{q}') = g^{(0),1}_{\text{inter}}(\mathbf{q}, \mathbf{q}') + g^{(0),2}_{\text{inter}}(\mathbf{q}, \mathbf{q}') + g^{(0),3}_{\text{inter}}(\mathbf{q}, \mathbf{q}')$$
$$\sim C + \frac{m^2U^3}{2\pi^3}\frac{\sqrt{4q_F^2 - p'^2}}{2q_F} - \frac{U^3m^2}{64\pi^3}(1 - \frac{p^2}{4q_F^2})\log[1 - \frac{p^2}{4q_F^2}], \tag{2.42}$$

and

$$g^{(0)}_{\text{intra}}(\mathbf{q}, \mathbf{q}') = g^{(0),1}_{\text{intra}}(\mathbf{q}, \mathbf{q}') + g^{(0),2}_{\text{intra}}(\mathbf{q}, \mathbf{q}') + g^{(0),3}_{\text{intra}}(\mathbf{q}, \mathbf{q}')$$
$$\sim C' - \frac{m^2U^3}{2\pi^3}\frac{\sqrt{4q_F^2 - p^2}}{2q_F} - \frac{U^3m^2}{64\pi^3}(1 - \frac{p^2}{4q_F^2})\log[1 - \frac{p^2}{4q_F^2}], \tag{2.43}$$

where $C > 0$ and $C' < 0$ are momentum-independent constants.

2.3.7 Supplementary Note 3: The real-space profile of the phase of the intra-pocket pairing wavefunction

Since the intra-pocket pairs are spinless and the intra-pocket interaction is attractive in the $\tilde{l} = 1$ channel, the intra-pocket pairing wavefunction on the spin-up pocket is expected to be $\Delta^{\uparrow\uparrow}_{\mathbf{q}} = \langle \psi_{\mathbf{K}+\mathbf{q},\uparrow}\psi_{\mathbf{K}-\mathbf{q},\uparrow}\rangle \propto q_x \pm iq_y$ in terms of separate spin and valley indices. The p-wave pairing is expected to be chiral to avoid nodes due to energetics. The pairing wavefunction in real space can then be obtained by doing the following Fourier transform:

$$\langle \psi_{\mathbf{r}+\frac{d}{2},\uparrow}\psi_{\mathbf{r}-\frac{d}{2},\uparrow}\rangle = \sum_{\mathbf{q}}\langle \psi_{\mathbf{K}+\mathbf{q},\uparrow}\psi_{\mathbf{K}-\mathbf{q},\uparrow}\rangle e^{i2\mathbf{K}\cdot\mathbf{r}}e^{i\mathbf{q}\cdot\mathbf{d}} = e^{i2\mathbf{K}\cdot\mathbf{r}}\sum_{\theta_{\mathbf{q}}} q_F e^{\pm i\theta_{\mathbf{q}}}e^{iqd\cos(\theta_{\mathbf{q}}-\theta_{\mathbf{d}})} \propto e^{i2\mathbf{K}\cdot\mathbf{r}}e^{i\theta_{\mathbf{d}}} \tag{2.44}$$

where $\mathbf{r}$ and $\mathbf{d} = d(\cos\theta_{\mathbf{d}}, \sin\theta_{\mathbf{d}})$ are the center-of-mass and relative positions of the pair repectively, the relative momentum $\mathbf{q} = q_F(\cos\theta_{\mathbf{q}}, \sin\theta_{\mathbf{q}})$ is confined on

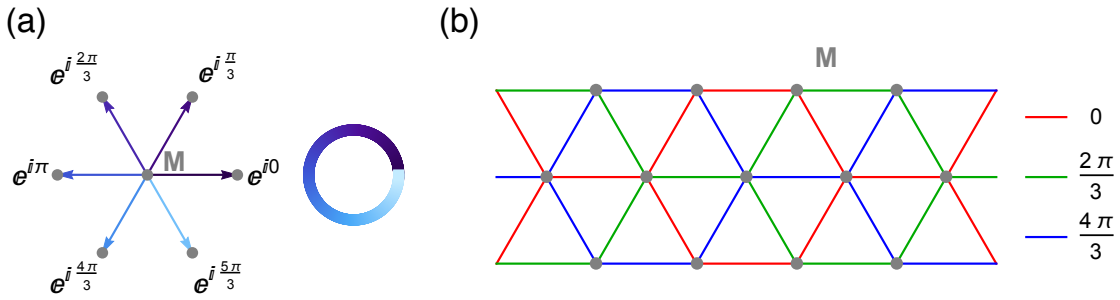

Figure 2.17: The phase of the intra-pocket pairing wave function in real space: (a) shows the phase $e^{i\theta_{\mathbf{d}}}$ in Supplementary Eq. (2.44) which accounts for the chiral $\tilde{l} = 1$ phase-winding within a pocket. The arrows represent $\mathbf{d}$ for the nearest-neightboring transition metal ions M (the grey dots). (b) shows the spatially modulated phase $e^{i2\mathbf{K}\cdot\mathbf{r}}$ due to the finite pair-momentum $2\mathbf{K}$ for a spin-up pair. We consider only pairing between electrons from nearest-neightboring sites. Thus, the phase of the pairing wave function is defined on each bond. The colors on the bonds represent different values of $2\mathbf{K}\cdot\mathbf{r}$.

the circular pocket centered at $\mathbf{K}$ with q_F being the Fermi momentum, and $\theta_{\mathbf{d}}(\theta_{\mathbf{q}})$ is the angle between $\mathbf{d}(\mathbf{q})$ and $\mathbf{K}$. While the phase winding from $e^{i\theta_{\mathbf{d}}}$ [see Supplementary Fig. 2.17(a)] accounts for the $q_x + iq_y$ pairing symmetry on a pocket, the spatial modulation in phase from $e^{i2\mathbf{K}\cdot\mathbf{r}}$ [see Supplementary Fig. 2.17(b)] is a consequence of the finite pair-momentum $2\mathbf{K}$.

2.4 Proximity-induced nematic odd-parity superconductivity in monolayer transition metal dichalcogenides by cuprate

This section is currently being written up for publication in a peer-reviewed journal, and is in collaboration with Dr. Kyungmin Lee and Prof. Eun-Ah Kim.

As discussed in the previous section, lightly hole-doped monolayer transition metal dichalcogenides (p-doped TMDs) are a family of noncentrosymmetric materials that host opposite spin species of low-energy electrons in the two valleys due to the intrinsic Ising spin-orbit coupling. Thanks to such spin-valley locked low-energy band structure, in the previous work my collaborators and I found the intrinsic superconductivity mediated by electronic correlations to be topological[62]. While experimental efforts in local groups towards realizing our proposal are still at the stage of sample fabrication, a possible obstable that could occur in the path is the situation where the lightly hole-doped monolayer TMDs do not intrinsically superconduct. Therefore in this work, my collaborators and I propose proximitizing as an alternative approach to obtain unconventional pairings besides hoping for intrinsic superconductivity. With the help from Kyungmin Lee, I study the pairing symmetry of the induced superconductivity in a p-doped TMD proximitized by a non-chiral d-wave superconductor, such as cuprates. By solving the Bogoliubov-de Gennes (BdG) equation on the interface of this heterostructure self-consistently, we find that sizable odd-parity pairing that breaks rotational symmetry is induced. This proposed setup offers a platform to experimentally study high-temperature two-dimensional superconductivity with odd parity.

2.4.1 Introduction

Odd-parity superconductors are a class of unconventional superconductors that exhibits rich and intriguing phenomena such as possessing Majorana zero modes[142], and breaking time-reversal[73] or point-group symmetries[180].

Existing candidate materials include the chiral f-wave heavy fermion superconductor UPt_3[69] and chiral p-wave transition-metal oxide Sr_2RuO_4[71]. In particular, superconductors with a two-component odd-parity order parameter that breaks rotational symmetry by choosing a certain combination of the two components are dubbed nematic[166]. Leading candidates of this kind are Cu-doped Bi_2Se_3[180] and uniaxially strained Sr_2RuO_4[157]. Although odd-parity superconductors have drawn extensive interests, they are unfortunately very rare[69, 71] and the leading candidates have low transition temperatures (T_c). Our goal in this work is to obtain odd-parity superconductivity with a higher T_c.

One place to look for odd-parity pairing is noncentrosymmetric metals since even- and odd-parity components are allowed to mix in a pair wavefunction when parity is not a good quantum number. Nonetheless their relative magnitude is not dictated by symmetry when the Fermi surface (FS) is spin-degenerate, so the odd-parity component could be vanishingly small. For instance, the proximity-induced pairing in graphene by a spin-singlet superconductor is predominantly spin-singlet with only a tiny triplet component resulting from the interfacial Rashba SOC[104, 33]. In contrast, non-vanishing odd-parity component is guaranteed on FS with certain spin-texture that dictates a substantial spin-triplet magnitude due to fermionic statistics. For instance, for oppositely spin-polarized pockets centered at opposite momenta shown in Fig. 2.18(a), the spin part of the interpocket pair wavefunction is an equal mixture of spin-singlet and -triplet with $s_z = 0$.

Important to this strategy for obtaining odd-parity pairing is the material that has FS with the desired spin texture. A suitable candidate is mono-

layer group IV transition metal dichalcogenides (TMD), the two-dimensional (2D) noncentrosymmetric semiconductors that have attracted rapidly growing attention[177, 67, 152]. The inversion-asymmetric lattice of monolayer TMDs leads to the orbital-selective[172, 190] Ising SOC[107] such that the Fermi pockets are nearly spin-degenerate upon electron-doping (n-doping), but strictly spin-valley locked upon hole-doping (p-doping) with chemical potential lying between the two spin-split valence bands [see Fig.2.18 (b) and (c)]. These spin-valley locked pockets resemble that we showed in Fig. 2.18(a), and thus suggest at least the same order of even- and odd-parity components in the inter-pocket pair wavefunction[62, 154]. Thanks to this spin-valley locking, such lightly p-doped monolayer TMDs have been predicted to host topological superconductivity if intrinsically superconducting under repulsive interaction[62]. Nonetheless, cases where low density of states or weak interaction strength prevent p-doped TMDs from superconducting or result in low T_c cannot be ruled out until experimentally tested. Hence here we instead study the proximity-induced pairing, where substantial odd-parity component is expected due to the spin-valley locking, by a spin-singlet superconductor.

To optimize the T_c of the induced pairing in TMD, we propose cuprate as the proximiting superconductor. In fact, cuprate-induced unconventional superconductivity has been experimentally observed in 1T-TaS_2[103] and graphene[33] at 40K and above 4K respectively despite the short coherence length of cuprates. Besides the possibly large difference in T_c, the induced pairings by a cuprate and by a conventional s-wave superconductor could also differ in the pairing symmetries as shown by the following crude guess: For cuprates with $d_{x^2-y^2}$-wave pairing symmetry, the induced triplet pairing is likely p-wave since they both belong to the 2D irreducible representation E of the

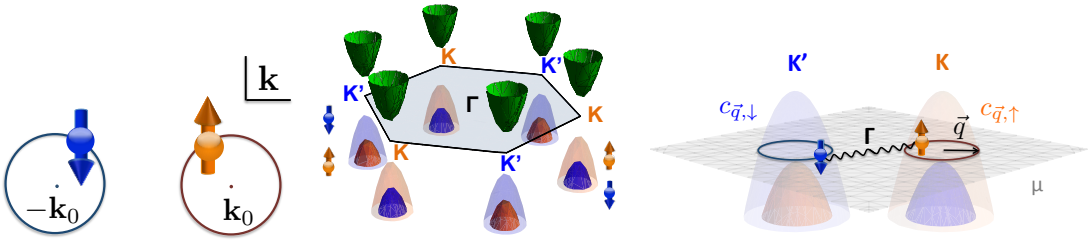

(a) (b) (c)

Figure 2.18: (a) Schematic FS with spin-splitting in momentum **k** space that could host inter-pocket pairs with pair wavefunctions being an equal mixture of spin-singlet and -triplet components. Here the two pockets centered at some opposite momenta $\pm\mathbf{k}_0$ host oppositely spin-polarized electrons (represented by the orange and blue arrows) in a time-reversal-symmetric manner. (b) Schematic low-energy dispersion of a monolayer TMD. The hexagon represents the first Brillouin zone boundary. The green paraboloids represent the nearly spin-degenerate conduction band, and the orange and blue paraboloids represent the spin-split valence bands for the spin-up and -down electrons, respectively. (c) A sketch for an inter-pocket pair formed on the pair of spin-valley locked pockets (represented by the red and blue circles) centered at $\pm\mathbf{K}$ in a lightly hole-doped monolayer TMD. The orange and blue paraboloids are the spin-up and -down valance bands and the the grey plane represents the chemical potential. The above figures were presented in Ref. [62].

point group C_{3v} for a pristine monolayer TMD. Note that this is different from existing proposals involving s-wave superconductors[169, 45, 154], where the induced triplet component was predicted to be f-wave that belongs to the trivial representation A_1 as s-wave does. Moreover, we expect this p-wave pairing to be nematic[180, 166] as one of the two components is suppressed by the absence of the d_{xy}-wave component in the cuprates.

To confirm our hypothesis, in this work we numerically study the induced pairing symmetry in the bilayer of lightly p-doped monolayer TMD and a layer of cuprate [see Fig. 2.19(a)] by solving the self-consistent gap equations. The

rest of the article is structured as follows: In section II, we construct the model for the bilayer and describe a method. In section III, we present and discuss the obtained pairing in the TMD layer from the calculation. We then summarize the findings in section IV.

2.4.2 Model and method

We focus on the interface of the cuprate-TMD heterostructure, which is a bilayer effectively comprising a CuO_4 layer and a lightly p-doped monolayer TMD with $N = L \times L$ lattice sites [see Fig. 2.19(a)]. We describe the kinetic terms of the cuprate and TMD layer respectively by the tight-binding models

$$H^{sc} = \sum_{\mathbf{x}} \sum_{i=1}^{2} -t\psi^{\dagger}_{\sigma,\mathbf{x}\pm\mathbf{a}_i}\psi_{\sigma,\mathbf{x}} - t'\psi^{\dagger}_{\sigma,\mathbf{x}\pm\mathbf{b}_i}\psi_{\sigma,\mathbf{x}} - \mu_{sc}\psi^{\dagger}_{\sigma,\mathbf{x}}\psi_{\sigma,\mathbf{x}} \tag{2.45}$$

and

$$\begin{aligned} H^{m} = \sum_{\mathbf{x}} & - \tilde{t}\phi^{\dagger}_{\uparrow,\mathbf{x}\pm\mathbf{c}_1}\phi_{\uparrow,\mathbf{x}} - \tilde{t}\phi^{\dagger}_{\uparrow,\mathbf{x}\pm\mathbf{c}_3}\phi_{\uparrow,\mathbf{x}} - \tilde{t}^{*}\phi^{\dagger}_{\uparrow,\mathbf{x}\pm\mathbf{c}_2}\phi_{\uparrow,\mathbf{x}} \\ & - \mu_m\phi^{\dagger}_{\uparrow,\mathbf{x}}\phi_{\uparrow,\mathbf{x}} + (\uparrow\rightarrow\downarrow, \tilde{t} \leftrightarrow \tilde{t}^{*}), \end{aligned} \tag{2.46}$$

where $\psi_{\sigma,\mathbf{x}}$ and $\phi_{\sigma,\mathbf{x}}$ annihilate an electron at site $\mathbf{x}$ with spin $\sigma =\uparrow,\downarrow$ on the square lattice of the copper atoms and the triangular lattice of the transition metal atoms respectively. $\mathbf{a}_i$ and $\mathbf{b}_i$ connect the nearest-neighbor (nn) and the next-nearest-neighbor (nnn) copper sites respectively, and $\mathbf{c}_i$ connect the nn transition metal sites [see Fig. 2.19(c)]. H^{sc} leads to a spin-degenerate large hole pocket whereas the effective two-band model H^{m} produces the desired Fermi pockets with spin-valley locking [see Fig. 2.19(b)].

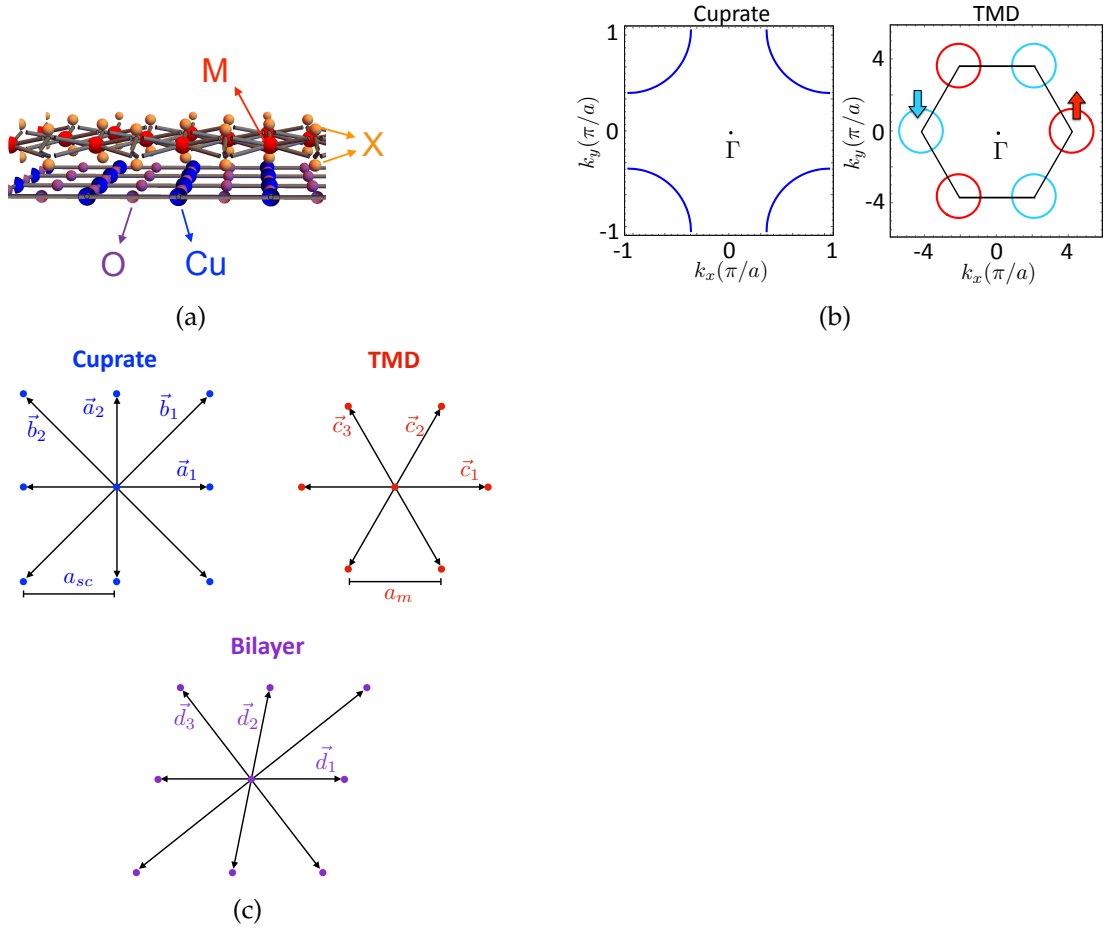

Figure 2.19: (a) A schematic for the bilayer of a monolayer TMD and the superconducting plane of the cuprate. (b) FSs of cuprate and TMD obtained from the tight-binding models Eq. (2.45) and (2.46) with parameter $\mu_c = -0.8$, $t = 1$, $t' = -0.3$, $\mu_m = 4.6$, and $\tilde{t} = \frac{1}{\sqrt{3}} + i$ in the unit of eV. (c) A sketch for the lattices of the cuprate and TMD layer in the absence of lattice straining (upper panel) and the sheared lattice of the bilayer in the presence of lattice straining (lower panel).

Due to the lattice mismatch between two lattices, certain amount of lattice strain is expected. To allow for the simplest microscopic form of interlayer coupling, we assume that the two layers share the same lattice with lattice vectors $\mathbf{d}_i$ under mutual lattice shearing such that $\mathbf{a}_1, \mathbf{c}_1 \rightarrow \mathbf{d}_1$, $\mathbf{a}_2, \mathbf{c}_2 \rightarrow \mathbf{d}_2$, and $\mathbf{b}_2, \mathbf{c}_3 \rightarrow \mathbf{d}_3$ [see Fig. 2.19(c)]. This sheared lattice with a reduced point group symmetry of C_s has four nn sites denoted by $\pm\mathbf{d}_1$, $\pm\mathbf{d}_2$ and two nnn sites denoted by $\pm\mathbf{d}_3$. We then introduce on-site, nn, and nnn interlayer hopping terms at the same magnitude $H' = \sum_{\mathbf{x}} \lambda \phi^{\dagger}_{\sigma,\mathbf{x}} \psi_{\sigma,\mathbf{x}} + \lambda \sum_{i=1}^{3} \phi^{\dagger}_{\sigma,\mathbf{x}\pm\mathbf{d}_i} \psi_{\sigma,\mathbf{x}} + h.c.$.

Together with the kinetic terms H^{sc}, H^{m}, and H', we can write down the Bogoliubov de Genn Hamiltonian for the bilayer by including the nn and nnn pairing terms $\sum_{\mathbf{x}} \Delta^{sc}_{\mathbf{xy}} \psi_{\uparrow\mathbf{x}} \psi_{\downarrow\mathbf{y}} + \Delta^{m}_{\mathbf{xy}} \phi_{\uparrow\mathbf{x}} \phi_{\downarrow\mathbf{y}} + h.c.$ with $\mathbf{y} = \mathbf{x} \pm \mathbf{d}_i$, $i = 1, 2, 3$. With this mean-field Hamiltonian, we then self-consistently solve the gap equations

$$\begin{aligned} \Delta^{sc}_{\mathbf{xy}} &= U \langle \psi_{\downarrow\mathbf{y}} \psi_{\uparrow\mathbf{x}} \rangle \\ \Delta^{m}_{\mathbf{xy}} &= U \langle \phi_{\downarrow\mathbf{y}} \phi_{\uparrow\mathbf{x}} \rangle, \end{aligned} \tag{2.47}$$

where $U < 0$ is the nearest-neighbor attraction. The initial pairing are set to be random but preserving time-reversal symmetry in both the cuprate and TMD layers.

2.4.3 Result

The calculated gap function of the induced pairing in TMD is shown in Fig. 2.20(a). Despite that the gap function in the cuprate layer is predominantly spin-singlet, the induced pairing contains a non-vanishing odd-parity component as it looks odd in $x+y$ direction with respective to Γ. In fact, the odd-parity

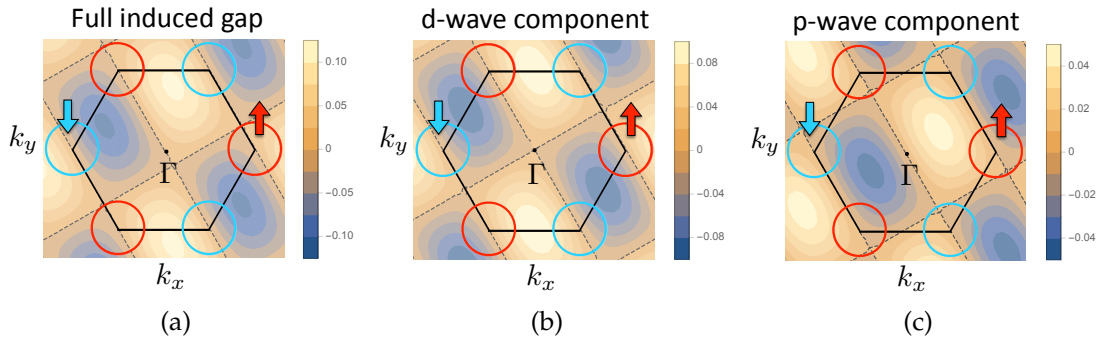

Figure 2.20: The proximity-induced pairing gap in the TMD layer obtained from the self-consistent calculation with system size $L = 25$, $\lambda = 0.5t$, $U = \ldots$ for ? reason. The hexagon and the red (cyan) circle represent the first Brillouin zone and the spin-up (-down) pocket of the TMD. The dashed black lines represent the nodal lines where gap vanishes. (a) The full induced gap. (b) and (c) The parity-even and -odd component of the induced gap.

component magnitude is about one-third of that of the even-parity component.

If we look at each parity component separately, the resulting singlet and triplet components shown in Fig. 2.20(b) and (c) have the form

$$\Delta_{\mathbf{k}}^{m,s} = 2\eta_s(\cos k_1 - \cos k_2) \tag{2.48}$$

and

$$\Delta_{\mathbf{k}}^{m,t} = -2\eta_t(\sin k_1 + \sin k_2), \tag{2.49}$$

where $k_i = \mathbf{k} \cdot \mathbf{d}_i$ for $i = 1, 2, 3$ and $\eta_s \sim 3\eta_t$. The absence of k_3 term in the induced gap in TMD $\Delta_{\mathbf{k}}^{m}$ indicates a pair of nodes on a pocket [see Fig. 2.20(a)], which means both components have partial wave $\tilde{l} = 1$ with respect to the valley centers. Nonetheless in terms of the angular momentum with respect to Γ point, the singlet component $\Delta_{\mathbf{k}}^{m,s}$ has even-parity with $d_{x^2-y^2}$-wave and the triplet component $\Delta_{\mathbf{k}}^{m,t}$ has odd-parity with $(p_x + p_y)$-wave. To be more precise, we should characterize the pairing symmetry from the point group of the bilayer, C_s. C_s has

one trivial irreducible representation A_1 and only one nontrivial one A_1', which differ by even or odd under the reflection with respect to the $(1\bar{1}0)$ plane. The obtained $(p+d)$-wave belongs to the non-trivial A_1' representation, whereas if a conventional s-wave superconductor were used instead of cuprate, the induced pairing would belong to the trivial representation A_1.

The obtained $(p+d)$-wave pairing preserves time-reversal symmetry due to the absence of the d_{xy}- and $(p_x - p_y)$-wave components, which is different from the chiral $\tilde{l} = 1$ pairing predicted intrinsically in p-doped TMDs under repulsive interaction. Moreover, by choosing k_3 to be the nodal direction, this $(p+d)$-wave pairing breaks rotational symmetry and is thus nematic. Hence, we have numerically obtained the induced pairing in the TMD layer to be nematic $(p+d)$-wave.

2.4.4 Summary and discussion

By self-consistently solving the gap equations, we found a sizable nematic odd-parity component in the induced superconductivity in a lightly hole-doped monolayer TMD proximitized by a cuprate. This induced odd-parity superconductivity could have a higher T_c than existing candidates for odd-parity superconductors. We emphasize that our result of obtaining nematic odd-parity superconductivity is robust so long as the bilayer lattice preserves an in-plane mirror symmetry under lattice straining. The exact lattice matching that was introduced here for calculation convenience is not essential. Although the lattice constants of the families of cuprates are much larger than that of 2H-TMD semiconductors, a lattice strain near a feasible scale could occur in suitable material

choices. For example, the lattice-constant mismatch between a 2H-WTe_2 and $HgBa_2CuO_{4+\delta}$ is $\sim 6\%$. The existence of the induced odd-parity superconductivity could be detected by a phase-sensitive detection, such as a superconducting quantum interference device (SQUID) loop formed by the proximitized TMD and an s-wave superconductor.

CHAPTER 3

TOPOLOGICAL INSULATORS

3.1 Effects of surface-bulk hybridization in three-dimensional topological metals

This section is adapted from Physical Review B 89, 205438 (2014), which was in collaboration with Prof. Kyungwha Park, Prof. Taylor Hughes, and Prof. Eun-Ah Kim.

Dirac surface states are signatures of time-reversal-symmetric three-dimensional (3D) topological insulators (TIs). These surface states with Rashba-type spin textures[57, 59] have attracted extensive attention in the past decade not only because they are direct consequences of the topological nature of 3D TIs, but also because of their potential application in spintronics[19, 29, 132, 39, 118, 34]. While Dirac surface states are expected to be robust in ideal TIs, many available materials for 3D TIs are in fact naturally electron-doped, which makes these materials topological *metals* rather than insulators[11, 57]. Therefore, identifying the effects of surface-bulk couplings becomes a key challenge in exploiting these surface states in 3D topological "metals". Here my collaborators and I combine an effective-model calculation and an ab-initio slab calculation to study the effects of the lowest order surface-bulk interaction: hybridization. In the effective-model study, I discretize an established low-energy effective four-band model and introduce hybridization between surface bands and bulk bands in the spirit of the Fano model. I find that hybridization enhances the energy gap between bulk

and Dirac surface states and preserves the latter's spin texture qualitatively albeit with a reduced spin-polarization magnitude. On the other hand, our ab-initio study done by Kyungwha Park finds the energy gap between the bulk and the surface states to grow upon an increase in the slab thickness, which is very much in qualitative agreement with my effective model study. Comparing the results of our two approaches, we deduce that the experimentally observed low magnitude of the spin polarization can be attributed to a hybridization-type surface-bulk interaction. We also discuss evidence for such hybridization in existing ARPES data.

3.1.1 Introduction

Many discrepancies between experimental measurements and theoretical predictions of ideal topological insulators (TI's) are attributed to the fact that the chemical potential lies in the conduction band and the bulk band interferes with measurements [80, 129, 11, 156]. That is, many available TI materials are actually metallic. Recent developments in thin-film experiments[188, 156, 4, 105, 81] further call for studies of surface-bulk electron interaction in films. However, explicit first-principles calculations on TI films are limited to very thin slabs with thickness less than 10 nm due to the computational cost. Therefore, there is a need for a simple microscopic model which incorporates surface-bulk interactions that can be used to study how physical properties depend on the film thickness.

One important question such a model should address is the effect of surface-bulk interaction on the spin-texture. The surface spin-texture is a key physi-

cal characteristic of topological surface states in ideal TIs. While low-energy effective theories guided by symmetries predict perfect spin-momentum locking for topological surface states within the bulk gap, spin- and angle-resolved photoemission spectroscopfy (SARPES) data show lower in-plane spin polarization and total spin magnitude[57, 127, 176]. On the other hand, an ab-initio calculation on a few-quintuple-layer (QL) slab[176] found both the spin polarization and the total spin magnitude to be much smaller. Although reduction in spin polarization and total spin magnitude are to be anticipated at large surface Fermi-momenta where hexagonal warping manifests[21, 41, 98], little is understood about the reduction observed at small Fermi-momenta and how the surface-bulk interaction affects the spin texture. However, such understanding is crucial for pursuing technical applications of spin-momentum locking in thin films of topological insulators in the metallic regime[44, 179, 39].

Our starting point is the observation made by Ref. [8] that the lowest order electron-electron interaction term between the surface state and the bulk states can be viewed as a hybridization term in the Fano model[110]. The key effect of hybridization in this low-energy effective theory is to spectroscopically separate surface states localized on the surface from the extended metallic bands. Building on the principles underlying this low-energy effective theory, we study the hybridization effects with a microscopic model of 3D time-reversal invariant strong topological insulators to address the thickness dependence of physical quantities and connect the results to ab-initio slab calculations. Specifically, we study TI slabs with finite thickness in the presence of surface-bulk interaction from two complementary perspectives: a simple microscopic model including the lowest order surface-bulk interaction and an ab-initio calculation of a few-QL Bi_2Se_3. We focus on how the spectroscopic properties and the spin texture

evolve as a function of film thickness.

The paper is structured as follows. In subsection 3.1.2 we construct a lattice model for a slab with surface-bulk hybridization (S-B hybridization) and study the spectroscopic properties of the model as well as the effects of the S-B hybridization on the spin texture. In subsection 3.1.3 we present an ab-initio study on 4,5,6-QL Bi_2Se_3 using density functional theory (DFT) and discuss the insight the simple hybridization model offers in understanding the ab-initio results. We then conclude in subsection 3.1.4 with discussions of implications of our results and open questions.

3.1.2 Lattice model for a slab with s-b hybridization

The Model

In order to introduce surface-bulk hybridization as a perturbation in the spirit of the Fano model[8] and study its effects on a slab with finite thickness, we first need a lattice model for a slab. For this, we discretize[1] the effective continuum model by Ref. [187], which is a four band $\mathbf{k} \cdot \mathbf{p}$ Hamiltonian guided by symmetries and first-principle-calculation results. We then make the system size finite along the vertical axis, i.e., the film growth direction.

The low-energy effective four-band model in Ref. [187] describes a strong 3D TI with rhombohedral crystal structure such as Bi_2Se_3. In this effective model each QL is treated as a layer since the inter-QL coupling is weak, and the four lowest-lying spin-orbital bands come from the mixing of the two P_z atomic or-

[1] A similar discretization was used in other papers, e.g., G. Rosenberg and M. Franz, Phys. Rev. B **85**, 195119 (2012).

bitals from Bi and Se referred to as P_1 and P_2 and the two spins $\uparrow, \downarrow$. We take this effective model written in terms of 4×4 Γ-matrices and discretize it following the discretization scheme used for 2D TIs in Ref. [90] such that the lattice Hamiltonian reduces to the low-energy effective $\mathbf{k} \cdot \mathbf{p}$ Hamiltonian in Ref. [187] in the limit $|\mathbf{k}| \to 0$. The resulting lattice model in the rotated spin-orbital basis $\{|P_1, \uparrow\rangle, -i|P_2, \uparrow\rangle, |P_1, \downarrow\rangle, i|P_2, \downarrow\rangle\}$ is

$$H_0 = \sum_{\mathbf{k}_\parallel, k_z} h_0(\mathbf{k}_\parallel, k_z) c^\dagger_{\mathbf{k}_\parallel, k_z} c_{\mathbf{k}_\parallel, k_z}, \tag{3.1}$$

where $c^\dagger_{\mathbf{k}_\parallel, k_z}$ is an operator creating a four spinor in the rotated spin-orbital basis with an in-plane momentum $\mathbf{k}_\parallel = (k_x, k_y)$ and perpendicular momentum k_z, and the lattice Hamiltonian[2] is

$$\begin{aligned} h_0(\mathbf{k}_\parallel, k_z) = \epsilon_1(\mathbf{k}_\parallel, k_z)\mathbb{I}_{4\times4} + \frac{A_1}{a_z}\sin(k_z a_z)\Gamma^1 \\ + \frac{A_2}{a_x}\sin(k_x a_x)\Gamma^3 + \frac{A_2}{a_y}\sin(k_y a_y)\Gamma^4 + M_1(\mathbf{k}_\parallel, k_z)\Gamma^5, \end{aligned} \tag{3.2}$$

with

$$\begin{aligned} \epsilon_1(\mathbf{k}_\parallel, k_z) \equiv & C + \frac{2D_1}{a_z^2}[1 - \cos(k_z a_z)] + \frac{2D_2}{a_x^2}[1 - \cos(k_x a_x)] \\ & + \frac{2D_2}{a_y^2}[1 - \cos(k_y a_y)], \end{aligned} \tag{3.3}$$

$$\begin{aligned} M_1(\mathbf{k}_\parallel, k_z) \equiv & m - \frac{2B_1}{a_z^2}[1 - \cos(k_z a_z)] - \frac{2B_2}{a_x^2}[1 - \cos(k_x a_x)] \\ & - \frac{2B_2}{a_y^2}[1 - \cos(k_y a_y)]. \end{aligned} \tag{3.4}$$

The Gamma matrices are defined as $\Gamma^1 = \sigma^z \otimes \tau^x$, $\Gamma^2 = -\mathbb{I}_{2\times2} \otimes \tau^y$, $\Gamma^3 = \sigma^x \otimes \tau^x$, $\Gamma^4 = \sigma^y \otimes \tau^x$, and $\Gamma^5 = \mathbb{I}_{2\times2} \otimes \tau^z$, where σ^j and τ^j are Pauli matrices acting on $(\uparrow, \downarrow)$ and (P_1, P_2) spaces, respectively. a_x, a_y and a_z are the lattice constants in x,

[2]The lattice Hamiltonian $h_0(\mathbf{k}_\parallel, k_z)$ does not have in-plane three-fold rotational symmetry of the continuum Hamiltonian. However, we do not expect this to change any of our conclusions in a qualitative manner.

y, z directions respectively. We use the parameters for Bi_2Se_3 obtained by fitting the continuum model to ab-initio calculations[187]: $m = 0.28$ eV, $A_1 = 2.2$ eV, $A_2 = 4.1$ eV, $B_1 = 10$ eV^2, $B_2 = 56.6$ eV^2, $C = -0.0068$ eV, $D_1 = 1.3$ eV^2 and $D_2 = 19.6$ eV^2.

We model a slab of Bi_2Se_3 by imposing open boundary conditions at the top and the bottom surfaces which break the translational symmetry along the z-axis. Since k_z is no longer a good quantum number, while $\mathbf{k}_\parallel$ still is, we substitute $c_{\mathbf{k}_\parallel,k_z} = \frac{1}{\sqrt{N}} \sum_j e^{ik_z j a_z} c_{\mathbf{k}_\parallel,j}$ in Eq. (3.1) and label the four-spinor operators by the in-plane momentum $\mathbf{k}_\parallel = (k_x, k_y)$ and the index of layers j stacking in the z direction. Now the Hamiltonian for a slab with N layers is

$$H_0(N) = \sum_{\mathbf{k}_\parallel} H_0(\mathbf{k}_\parallel, N), \tag{3.5}$$

where

$$H_0(\mathbf{k}_\parallel, N) = \sum_{j=1}^{N} \mathbb{M}\, c^\dagger_{\mathbf{k}_\parallel,j} c_{\mathbf{k}_\parallel,j} + \mathbb{T} c^\dagger_{\mathbf{k}_\parallel,j+1} c_{\mathbf{k}_\parallel,j} + \mathbb{T}^\dagger c^\dagger_{\mathbf{k}_\parallel,j} c_{\mathbf{k}_\parallel,j+1} \tag{3.6}$$

and the 4×4 matrices $\mathbb{T}$ and $\mathbb{M}$ are defined as

$$\mathbb{T} \equiv -\frac{D_1}{a_z^2}\mathbb{I}_{4\times4} + \frac{B_1}{a_z^2}\Gamma^5 - \frac{iA_1}{2a_z}\Gamma^1, \tag{3.7}$$

and

$$\mathbb{M} \equiv \epsilon_2(\mathbf{k}_\parallel)\mathbb{I}_{4\times4} + \frac{A_2}{a_x}\sin(k_x a_x)\Gamma^3 + \frac{A_2}{a_y}\sin(k_y a_y)\Gamma^4 + M_2(\mathbf{k}_\parallel)\Gamma^5 \tag{3.8}$$

where

$$\epsilon_2(\mathbf{k}_\parallel) \equiv C + \frac{2D_1}{a_z^2} + \frac{2D_2}{a_x^2}[1 - \cos(k_x a_x)] + \frac{2D_2}{a_y^2}[1 - \cos(k_y a_y)] \tag{3.9}$$

and

$$M_2(\mathbf{k}_\parallel) \equiv m - \frac{2B_1}{a_z^2} - \frac{2B_2}{a_x^2}[1 - \cos(k_x a_x)] - \frac{2B_2}{a_y^2}[1 - \cos(k_y a_y)]. \tag{3.10}$$

For the sake of simplicity, the results presented in the remainder of this subsection are calculated with $a_x = a_y = a_z = 1$Å.

We can diagonalize $H_0(\mathbf{k}_\parallel, N)$ as

$$H_0(\mathbf{k}_\parallel, N) = \sum_{\alpha=1}^{4N-4} E^0_{B,\alpha}(\mathbf{k}_\parallel) b^{0\dagger}_{\alpha,\mathbf{k}_\parallel} b^0_{\alpha,\mathbf{k}_\parallel} + \sum_{\beta=1}^{4} E^0_{D,\beta}(\mathbf{k}_\parallel) d^{0\dagger}_{\beta,\mathbf{k}_\parallel} d^0_{\beta,\mathbf{k}_\parallel}, \tag{3.11}$$

where $b^0_{\alpha,\mathbf{k}_\parallel}$ and $d^0_{\beta,\mathbf{k}_\parallel}$ are four-spinor annihilation operators for bulk and surface states (henceforth referred to as the "Dirac" states) respectively in the absence of hybridization, $E^0_{B,\alpha}$ and $E^0_{D,\beta}$ are their corresponding eigenenergies. Here, α and β label the unhybridized bulk and Dirac states respectively. All energy eigenstates are two-fold degenerate as required by inversion (P) and time-reversal (T) symmetries. For each in-plane momentum $\mathbf{k}_\parallel$, four energy eigenstates with their energies closest to the Dirac point are labeled to be valence ($\beta = 1, 2$) and conduction ($\beta = 3, 4$) Dirac states. α label the remaining $4N - 4$ bulk states. A natural choice for the labeling is to let $\alpha = 1, \cdots, 2N - 2$ denote valence bulk states and let $\alpha = 2N - 1, \cdots, 4N - 4$ denote conduction bulk states with the eigenenergies increasing monotonically with α. As the model is derived from a low-energy effective model near the Dirac point, it will break down at large energies. However, we expect qualitatively correct results when it comes to trends of physical properties over the hybridization strength and film thickness which only require knowledge of the low-energy physics near the insulating gap.

Now we introduce the S-B hybridization term that is allowed by symmetries in the spirit of Fano model[110]. The Fano model is a generic model describing the mixing between extended states c_k with energy ϵ_k and a localized state b with energy ϵ through Hamiltonian $H_F = \epsilon b^\dagger b + \sum_k [\epsilon_k c_k^\dagger c_k + A_k (c_k^\dagger b + b^\dagger c_k)]$, where A_k represents scattering strength. Ref. [8] pointed out that H_F can be used to describe the lowest order interaction between a helical surface state and a metallic bulk band, i.e. hybridization. They studied effects of hybridization in a field theoretic approach. Here we use a symmetry-preserving form of the surface-

bulk hybridization term in the spirit of H_F for the microscopic model of Bi_2Se_3 shown in Eq. (3.23) to study the effects of mixing between Dirac states and bulk states.

For simplicity we consider the case where the hybridization strength preserves in-plane momenta $\mathbf{k}_\parallel$ and is independent of energy and $\mathbf{k}_\parallel$, i.e.

$$h'(\mathbf{k}_\parallel) = \sum_{\alpha,\beta} g\ b^{0\dagger}_{\alpha,\mathbf{k}_\parallel} d^{0}_{\beta,\mathbf{k}_\parallel} + H.c.. \tag{3.12}$$

We then impose T and P symmetries on the full hybridization perturbation $H'(\mathbf{k}_\parallel)$ by constructing $H'(\mathbf{k}_\parallel)$ through

$$\begin{aligned} H'(\mathbf{k}_\parallel) = h'(\mathbf{k}_\parallel) + Ph'(\mathbf{k}_\parallel)P^\dagger + Th'(\mathbf{k}_\parallel)T^\dagger \\ + PTh'(\mathbf{k}_\parallel)(PT)^\dagger, \end{aligned} \tag{3.13}$$

where the representations for T and P symmetry operators with the spatial inversion center at the middle point of the slab in the current $4N$ tight-binding spin-orbital basis are $T = K\ i\sigma^y \otimes \mathbb{I}_{2\times2} \otimes \mathbb{I}_{N\times N}$ with $\mathbf{k}_\parallel \leftrightarrow -\mathbf{k}_\parallel$, and $P = \mathbb{I}_{2\times2} \otimes \tau^z$ with $z : [0, N/2] \leftrightarrow [N/2, N]$ and $\mathbf{k}_\parallel \leftrightarrow -\mathbf{k}_\parallel$, respectively. Here, K is the usual complex conjugation operator. Finally, the full Hamiltonian including hybridization at a given in-plane momentum $\mathbf{k}_\parallel$ reads

$$H(\mathbf{k}_\parallel) = H_0(\mathbf{k}_\parallel, N) + H'(\mathbf{k}_\parallel). \tag{3.14}$$

After diagonalizing the full Hamiltonian in the tight-binding spin-orbital bases, we can write

$$\begin{aligned} H(\mathbf{k}_\parallel) = \sum_{\alpha=1}^{4N-4} E_{B,\alpha}(\mathbf{k}_\parallel) b^\dagger_{\alpha,\mathbf{k}_\parallel} b_{\alpha,\mathbf{k}_\parallel} \\ + \sum_{\beta=1}^{4} E_{D,\beta}(\mathbf{k}_\parallel) d^\dagger_{\beta,\mathbf{k}_\parallel} d_{\beta,\mathbf{k}_\parallel}, \end{aligned} \tag{3.15}$$

where $b_{\alpha,\mathbf{k}_\parallel}$, $d_{\beta,\mathbf{k}_\parallel}$, $E_{B,\alpha}$ and $E_{D,\beta}$ are defined similarly to the corresponding symbols with a superscript 0 in Eq. (3.23) but in the presence of hybridization.

$E_{B,\alpha}$ and $E_{D,\beta}$ are again two-fold degenerate as $H(\mathbf{k}_\parallel)$ preserves parity and time-reversal symmetries by design. α and β label the bulk and Dirac states for $H(\mathbf{k}_\parallel)$, where the terms bulk and Dirac states are defined in the same fashion as for $H_0(\mathbf{k}_\parallel, N)$ in the absence of hybridization.

Topological Metal Regime

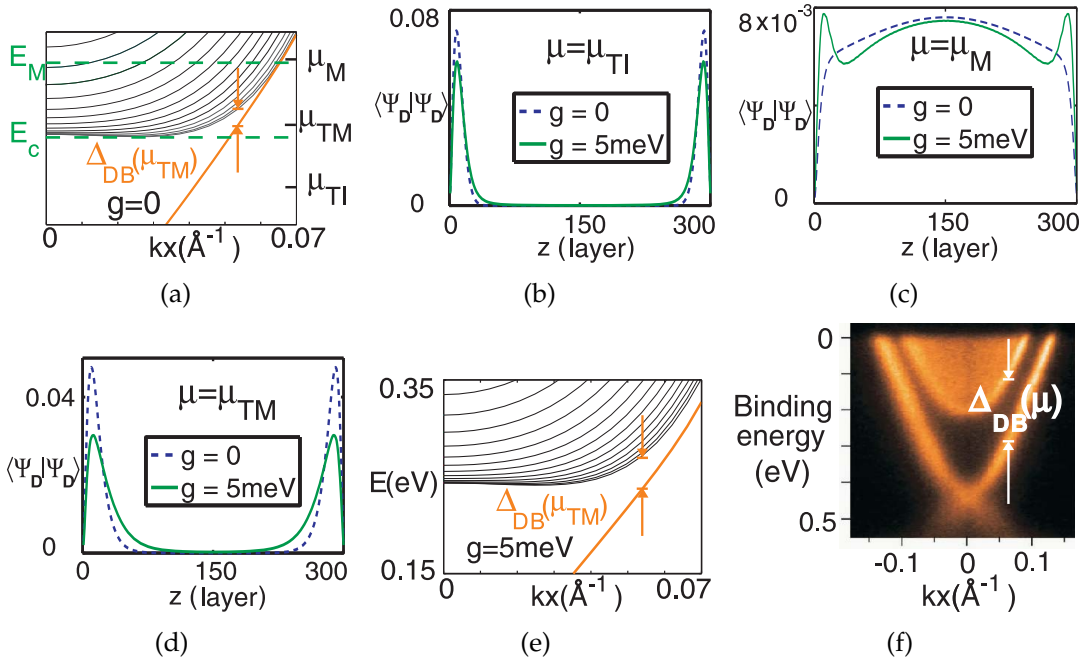

Figure 3.1: (a) Spectra of the model on a 300-layer-thick slab. The three chemical potentials μ_{TI}, μ_{TM} and μ_M are taken as representative points for the three regimes TI($\mu \leq E_c$), M ($\mu \gtrsim E_M$), and TM($E_c \leq \mu \lesssim E_M$) as defined in the text, respectively. (b)-(d)The corresponding unhybridized(dashed, blue) and hybridized(solid, green) spatial profiles of the pair of degenerate conduction Dirac states $|\Psi_{D,\mathbf{k}_\parallel}(z)|^2$ at $\mathbf{k}_\parallel = \mathbf{k}_{\parallel,\mu}$ with $\mu = \mu_{TI}, \mu_{TM}$, and μ_M, respectively. (e) Effect of the hybridization on the spectra. (f)ARPES data on Bi_2Se_3[11].

We begin our numerical study with no hybridization. In the absence of hybridization, depending on the chemical potential μ, we now define three

regimes: topological insulator(TI), metal(M), and topological metal(TM)(see Fig. 3.1(a)). The familiar topological insulator (TI) regime is where the chemical potential lies within the bulk gap and the system is actually a bulk band insulator, i.e., $E_v \leq \mu \leq E_c$ with E_c being the bottom of the conduction band and E_v the top of the valence band. Within the TI regime, the Dirac states feature Rashba-type spin-momentum locking and a spatial profile localized on the surfaces. Of our particular interest is the distinction we will draw between M and TM regimes based on whether the Dirac states retain the spin-momentum locking and the surface localization when being away from the TI regime.

In order to examine the above two properties of Dirac states, we define $|\psi_{D,\mathbf{k}_\parallel}\rangle \equiv d^\dagger_{3,\mathbf{k}_\parallel}|0\rangle$ ($d^{0\dagger}_{3,\mathbf{k}_\parallel}|0\rangle$) and $|\tilde{\psi}_{D,\mathbf{k}_\parallel}\rangle \equiv d^\dagger_{4,\mathbf{k}_\parallel}|0\rangle$ ($d^{0\dagger}_{4,\mathbf{k}_\parallel}|0\rangle$) in the presence(absence) of hybridization to represent the pair of degenerate Dirac states above the Dirac point. Now the spatial profile of the conduction Dirac states is $|\Psi_{D,\mathbf{k}_\parallel}(z)|^2 \equiv |\psi_{D,\mathbf{k}_\parallel}(z)|^2 + |\tilde{\psi}_{D,\mathbf{k}_\parallel}(z)|^2$ which is a function of z measured from the bottom of the slab along the finite dimension of the slab. This quantity will show whether the Dirac states are localized on the surfaces or not. Let us identify a particular $\mathbf{k}_\parallel$ of interest for a given value of chemical potential as the in-plane momentum at which the chemical potential μ intersects the Dirac branch; we denote such in-plane momentum by $\mathbf{k}_{\parallel,\mu}$. To illustrate the features defining the three regimes, we will now show the spatial profiles and the spin polarizations of the Dirac states in the three regimes in the absence of hybridization. In the next subsection we will add the hybridization and examine its effects.

Inspecting $|\Psi_{D,\mathbf{k}_\parallel}(z)|^2$ at $\mathbf{k}_\parallel = \mathbf{k}_{\parallel,\mu}$ at the representative values of chemical potential for the three regimes $\mu_{TI}, \mu_M, \mu_{TM}$ shown in Fig. 3.1, we find that the spatial profile of the Dirac states $|\Psi_{D,\mathbf{k}_\parallel}(z)|^2$ indicates surface localized states of the

slab in the TI regime as expected (see Fig. 3.1(b)). On the other hand, in the M regime, where the chemical potential is well within the bulk conduction band, $|\Psi_{D,\mathbf{k}_\parallel}(z)|^2$ is fully delocalized over the entire slab (see Fig. 3.1(c)). In this regime, the system cannot be distinguished from an ordinary metal. However, even with $\mu > E_c$ there is an energy window between E_c and a crossover energy scale E_M, where the Dirac states are still spatially localized on the surfaces in the sense that $|\Psi_{D,\mathbf{k}_\parallel}(z)|^2$ is peaked on each surface of the slab and decays away from the surfaces (see Fig. 3.1(d)). The crossover energy scale E_M is a threshold energy, where, within the regime $\mu \gtrsim E_M$ (regime M), wavefunctions for all states at in-plane momentum $\mathbf{k}_{\parallel,\mu}$ delocalize. We define the system to behave as a topological metal(TM) when the chemical potential lies within this window, i.e. $E_c < \mu < E_M$, represented by μ_{TM}.

A detectable characteristic of TI and TM regimes is the spin-momentum locking. One measure to quantify spin-momentum locking at the surface is through the so-called "spin polarization" which is the expectation value of the spin component perpendicular to the in-plane momentum of a Dirac state, i.e.,

$$\langle S_{\hat{\mathbf{n}}} \rangle(\mathbf{k}_\parallel) \equiv \langle \psi_{D,\mathbf{k}_\parallel} | S_{\hat{\mathbf{n}}} | \psi_{D,\mathbf{k}_\parallel} \rangle \tag{3.16}$$

with $\hat{\mathbf{n}} \cdot \mathbf{k}_\parallel = 0$. Here the $\hat{\mathbf{n}}$ component of the quantum spin operator is defined as $S_{\hat{\mathbf{n}}} \equiv \frac{\hbar}{2} \vec{\sigma} \cdot \hat{\mathbf{n}} \otimes \mathbb{I}_{2\text{x}2} \otimes \mathbb{I}_{\text{NxN}}$, where $\vec{\sigma} = (\sigma_x, \sigma_y, \sigma_z)$ are Pauli matrices acting on spin, $\mathbb{I}_{2\text{x}2}$ acts on the orbital degree of freedom , and $\mathbb{I}_{\text{NxN}}$ acts on the layer index. $\langle S_y \rangle(k_x \hat{x})$ is evaluated at $k_x \hat{x} = k_{x,\mu} \hat{x}$ and shown for $\mu = \mu_{TI}, \mu_{TM}, \mu_M$ in Fig. 3.2(a). We see here that, in the absence of hybridization(g=0), the spin polarization stays maximal in the TI and TM regimes while rapidly dropping upon entering the M regime. Another quantity of experimental interest is the total spin magnitude associated with the Dirac states with in-plane momentum $\mathbf{k}_\parallel$ defined in terms of

spin polarization as

$$S(\mathbf{k}_{\|}) \equiv \sqrt{\sum_{i=x,y,z} [\langle S_i \rangle(\mathbf{k}_{\|})]^2}. \tag{3.17}$$

Fig. 3.2(a) and 3.2(b) show that the spin-momentum locking quantified using these measures clearly distinguishes the TM regime from the ordinary metal regime (M) in the absence of hybridization.

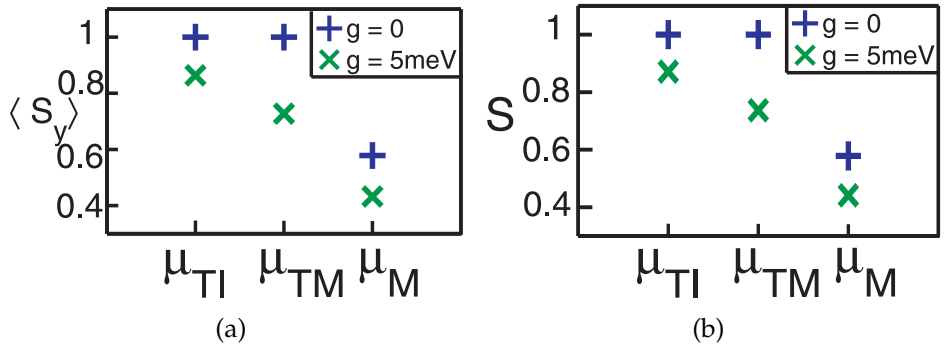

Figure 3.2: The effect of hybridization on the degree of spin-momentum locking in different regimes. The spin expectation values are calculated for a 300-layer-thick slab using a conduction Dirac state $|\psi_{D,k_x\hat{x}}\rangle$ with $k_x = k_{x,\mu}$ at different representative chemical potentials $\mu = \mu_{TI}$, μ_{TM} and μ_M. (a)Spin polarization $\langle S_y \rangle(k_x\hat{x})$. (b)Total spin magnitude $S(k_x\hat{x})$(defined in the text).

Effects of S-B Hybridization

We now turn to the effects of hybridization. One effect of hybridization that is manifest in the experimental detection of Dirac surface states in the TM regime is an increase in the bulk-Dirac state energy gap. We quantify this energy gap, for a given chemical potential μ, using the energy difference between a Dirac state above the Dirac point and the energetically closest bulk state defined by

$$\Delta_{DB}(\mu) \equiv E^{(0)}_{B,2N-1}(k_{\|,\mu}) - E^{(0)}_{D,3}(k_{\|,\mu}) \tag{3.18}$$

in the presence(absence) of hybridization. Comparing Fig. 3.1(a) to (e), we find that the key effect of hybridization that is spectroscopically detectable is the increase in $\Delta_{DB}(\mu)$ in both TM and M regimes compared to the TI regime. Otherwise the spectra in the absence or presence of hybridization look similar. Note that most ARPES data on 3D TIs exhibit a clear energy gap between the Dirac branch and the bulk states at a chemical potential well into the bulk band as shown in Fig. 3.1(f). This experimental trend hints at the possibility that a sizable hybridization between Dirac states and the bulk states is common in 3D TI materials. In order to demonstrate the effect of hybridization, we choose a value of g = 5meV that is subdominant to all the hopping terms yet substantial in this paper. However, key effects of hybridization do not depend qualitatively on the value of g.

Another effect of hybridization is to broaden the Dirac state wavefunctions in the TI and TM regimes. The degree of broadening depends on the chemical potential μ, hybridization strength g, and the slab thickness N. However, as long as g is the smallest energy scale in the total Hamiltonian as is the case for Figs. 3.1(b-d), the Dirac states in the TI and TM regimes remain localized on the surfaces. A tangible consequence of the wavefunction broadening is the quantitative suppression of the spin-momentum locking. As mentioned earlier, in the absence of hybridization the Dirac states of TI and TM exhibit a maximal degree of spin-momentum locking. However, hybridization rotates the spin vectors of different atomic orbitals and layers away from the direction perpendicular to the in-plane momentum. Hence, both measures of spin-momentum locking shown in Fig. 3.2 show quantitative reduction upon hybridization. This is in qualitative agreement with the low values of spin polarization and total spin magnitude found in a first-principle calculation of a thin slab in a previous

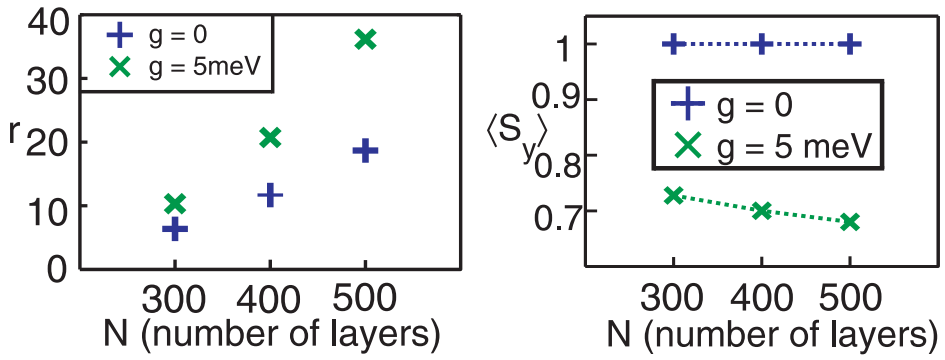

Figure 3.3: Thickness dependence of the hybridization effects. (a)Dimensionless measure of bulk-Dirac energy gap $r = \Delta_{DB}/\Delta_{BB}$(defined in the text) at different slab thickness for $\mu = \mu_{TM}$. (b)The spin polarization of a conduction Dirac state $\langle S_y \rangle(k_x\hat{x})$ at $\mu = \mu_{TM}$.

work[176] and our DFT results in the next subsection. Note that the hybridization still preserves the spin-texture winding despite the quantitative reduction in the spin polarization.

Finally, we study how the effects of hybridization on the two experimentally accessible characteristics of the TM regime, namely how the bulk-Dirac energy gap $\Delta_{DB}(\mu)$ and the spin polarization $\langle S_{\hat{n}} \rangle(\mathbf{k}_{\|})$ of a Dirac state, vary with the slab thickness. Since the quantized energy spacings due to finite size effects decreases with increasing slab thickness, we consider a dimensionless measure that quantifies the bulk-Dirac energy gap:

$$r(\mu) \equiv \Delta_{DB}(\mu)/\Delta_{BB}(\mu), \tag{3.19}$$

where $\Delta_{BB}(\mu) \equiv E^{(0)}_{B,2N+1}(k_{\|,\mu}) - E^{(0)}_{B,2N-1}(k_{\|,\mu})$ is the energy spacing in the presence(absence) of hybridization between the two lowest lying conduction bulk branches measured at the same in-plane momentum $\mathbf{k}_{\|,\mu}$ where $\Delta_{DB}(\mu)$ is calculated. This dimensionless quantity $r(\mu)$ allows us to compensate for finite size effects though Δ_{BB} would be hard to measure experimentally for realistic bulk

samples due to the lack of the required energy resolution. Fig. 3.3(a) shows that the hybridization induced enhancement in the bulk-Dirac energy gap becomes more prominent with increasing slab thickness. Comparing the existing ARPES data on bulk samples[11] and on thin films[188], we find the Dirac branch to be better separated from the bulk states in the bulk samples than in the thin films, which is consistent with the hybridization effect shown in Fig. 3.3(a). Finally Fig. 3.3(b) shows that the reduction in spin-polarization magnitude $|\langle S_y \rangle(k_x \hat{x})|$ is also intensified with increasing thickness. Such an enhancement in the impact of hybridization with the increase in slab thickness can be explained from the fact that a thicker slab implies a larger number of bulk states that mix with a fixed number of Dirac surface states for a given strength of hybridization g.

3.1.3 DFT calculations of thin Bi_2Se_3 slabs

Now we turn to an ab-initio study of thin slabs to compare with the simple phenomenological model of hybridization we explored in the previous subsection. The approach of the previous subsection is limited, in the sense that it builds on a low-energy effective description of the band structure, and that there is no detailed knowledge of the hybridization strength g which could in principle be $\mathbf{k}_{\|}$-dependent. On the other hand, the DFT approach on slabs, which does not require calculating surface and bulk separately as in the calculations of semi-infinite systems[187], is limited to very thin films of several QLs due to computational limits. By combining the two approaches, we extract a more robust understanding of the effects of hybridization in the TM regime and implications on their trends over film thickness.

We calculate the electronic structure of Bi_2Se_3(111) slabs of 4-6 QLs using the VASP code [95, 92] with the projector-augmented-wave method [15], within the generalized-gradient approximation (GGA) [130]. Spin-orbit coupling is included self-consistently. We use experimental lattice constants [120] and an energy cutoff of 420 eV with a $31 \times 31 \times 1$ k-point grid. Our DFT calculations are limited up to 6 QLs. For 5-6 QLs, the overlap between top and bottom surface states is already very small yielding an energy gap of the order of meV at Γ. Expectation values of spin components $\langle S_x \rangle$, $\langle S_y \rangle$, $\langle S_z \rangle$ are calculated from the summation of the expectation values of each atom.

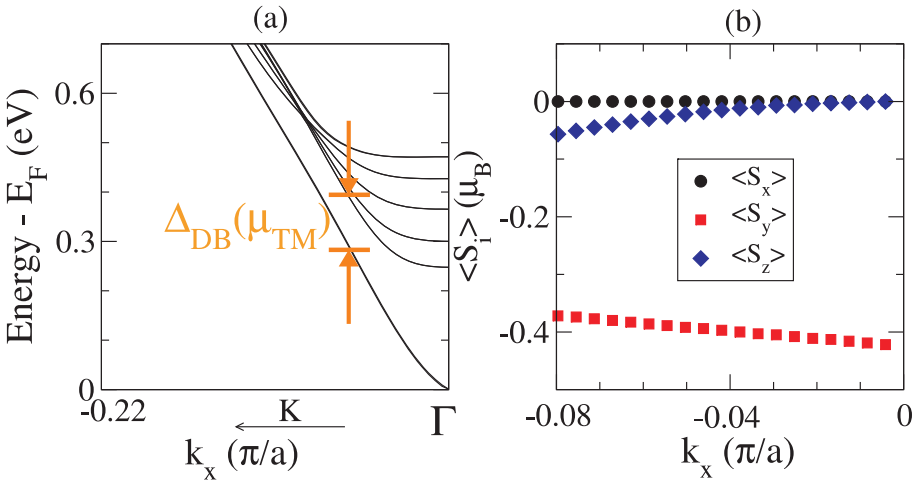

Figure 3.4: (a) DFT-calculated band structure of a 6-QL slab of Bi_2Se_3. (b)DFT-calculated spin expectation values of the conduction Dirac state $\langle S_i \rangle (k_x \hat{x})$ for a 6-QL Bi_2Se_3 slab.

Figure 3.4 shows the DFT-calculated band structure and spin expectation values $\langle S_i \rangle (k_x \hat{x})$ of a 6-QL slab. The surface states are doubly degenerate and have a Dirac dispersion and we show five confined states in the bulk conduction band region [Fig. 3.4(a)]. For small $|k_x|$ values, $\langle S_y \rangle$ of a Dirac conduction state is clearly dominant over other components and exhibits spin-momentum locking [Fig. 3.4(b)]. As $|k_x|$ increases, a small z component of spin expectation

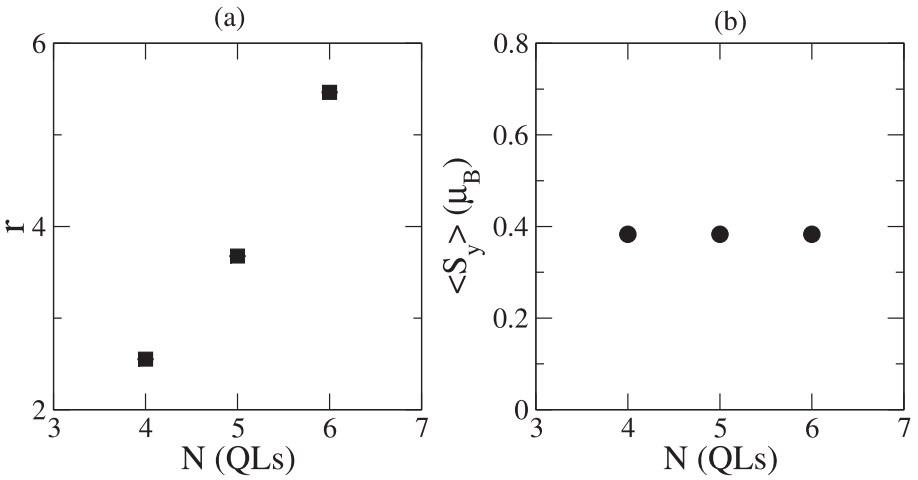

Figure 3.5: (a) Ratio $r = \Delta_{DB}/\Delta_{BB}$ within the TM regime, calculated at a fixed $\mathbf{k}_{\|}$. (b) $\langle S_y \rangle$ of the conduction Dirac state calculated using DFT as a function of slab thickness N.

value develops. However, over the entire range of k_x, $\langle S_y \rangle$ is much less than the maximal value, in agreement with previous DFT study[176]. A comparison between Fig. 3.2 and Fig. 3.4(b) indicates that our hybridization model is an effective way to capture the broadening of the Dirac surface state wavefunction and the resulting reduction in the spin polarization and the total spin magnitude[3].

Now we discuss the thickness dependence in the bulk-Dirac energy gap measure and the spin polarization. We calculate the dimensionless measure of bulk-Dirac energy gap $r = \Delta_{DB}/\Delta_{BB}$ in the TM regime at the $\mathbf{k}_{\|}$ point where the Dirac surface state branch has slightly higher energy than the bottom of the conduction band E_c, as indicated in Fig. 3.4(a). We find that the ratio $\Delta_{BB}(N_1)/\Delta_{BB}(N_2)$ is close to $(N_2/N_1)^2$ at the $k_{\|}$ point of interest as expected of finite-size-effect origin of the scale $\Delta_{BB}(N)$. Surprisingly, despite the small range of thickness accessible to the slab DFT calculation, the dimensionless measure of

[3]Our DFT calculations also show evidence of the hexagonal warping effect[41, 98] for $k_x \geq 0.08\pi/a$

bulk-Dirac energy gap $r = \Delta_{DB}/\Delta_{BB}$ in Fig. 3.5(a) shows a significant increase upon an increase in the slab thickness. This is qualitatively consistent with observations from the effective model and hybridization effects in Sec. 3.1.2. On the other hand, the range of thickness in the present calculation appears to be too small to show any change in the $\langle S_y \rangle$ as a function of slab thickness [Fig. 3.5(b)].

3.1.4 Conclusion

We combined a Fano-type hybridization model calculation with an ab-initio slab calculation to study the lowest order effects of surface-bulk interaction in topological insulators with a particular focus in the TM regime. We defined the TM regime of a topological insulator to be where the Dirac surface states and bulk states coexist and interact, yet the spin-winding is preserved albeit with a reduced spin-polarization magnitude. The hybridization model presented in Sec. 3.1.2 captures the spin-polarization reduction of the Dirac states originating from the hybridization with bulk states. Given the metallic behavior of most TIs, and the experimental evidence of reduced spin polarization, our simple model offers a useful starting point for applications of TIs which need to take real materials in the TM regime into account. Moreover, the hybridization-driven bulk-Dirac energy gap explains why the Dirac branch shows up so well separated from bulk states in ARPES experiments. Note that this energy gap and the suppression of total spin magnitudes are both experimentally observed phenomena that cannot be accessed by the typical approach of coupling a single "surface layer" to a bulk electronic structure to include surface states in semi-infinite systems as in Ref. [187]. We propose SARPES experiments for films of

varying thickness to test our predictions for hybridization-driven suppression of spin polarization for further vindication of the model.

Promising future directions include DFT tools to study slightly thicker systems. This might reveal thickness dependence in spin polarization and compared to the results of the simple model. Also this would reveal more detailed knowledge of the magnitude and $\mathbf{k}_{\|}$-dependence of the hybridization strength g. Preliminary DFT results show that $g(\mathbf{k}_{\|})$ has a significant $\mathbf{k}_{\|}$-dependence. Another interesting direction will be to study consequences of the hybridization effect on transport properties. Many puzzling aspects of transport experiments[156, 81, 4, 105] have been attributed to the presence of bulk states or surface-bulk interaction. There is growing theoretical interest on the transport properties of topological edge states in the presence of metallic bulk states[7, 5, 75, 70] as well. Our microscopic model offers a simple starting point to theoretically address effects of surface-bulk interaction on transport in 3D TIs.

Acknowledgements. We thank S. Oh for stimulating discussions. E.-A.K., Y.-T.H., and M.H.F. were supported in part by NSF CAREER grant DMR-095582 and in part by the Cornell Center for Materials Research with funding from the NSF MRSEC program (DMR-1120296). K.P. was supported by NSF DMR-0804665, DMR-1206354, and San Diego Supercomputer Center (DMR-060009N). TLH was supported by US DOE under QMN DE-FG02-07ER46453.

3.2 Hybridization-induced interface states in a topological-magnetic metal bilayer

This section is currently being written up for publication in a peer-reviewed journal, and is in collaboration with Prof. Kyungwha Park and Prof. Eun-Ah Kim.

As mentioned in the previous section, the Dirac surface states of three-dimensional (3D) topological insulators (TIs) have attracted extensive attention for their potential application in spintronics. While these surface states are expected to be robust in ideal TIs, however, their stability could be in question in realistic TI materials or TI-based structures. In the previous section I illustrated my study on the former case, where surface-bulk couplings become important in the naturally electron-doped topological "metals". In this section I will discuss my study on the latter case, in particular TI-ferromagnetic metal(FM) heterostructures. I focus on TI-FM bilayers because recent experiments have demonstrated large spin-transfer torques in such bilayers[118]. The source of the observed spin-transfer torque, however, remains unclear. This is because the large charge transfer from the FM to TI layer would prevent the Dirac cone on the interface from being anywhere near the Fermi level to contribute to the observed spin-transfer torque. Moreover, there is yet little understanding on the impact on the Dirac cone on the interface from the metallic bands overlapping in energy and momentum, where strong hybridization could take place. Here my collaborators and I investigate the fate of these Dirac interface states in TI-FM heterostructures from two complementary prospectives: I build a simple microscopic model

and Kyungwha Park perform first-principles-based simulations for such heterostructure, considering both the strong hybridization and charge transfer effects. We find that the original Dirac cone is destroyed by the hybridization as expected. Instead, we find a new interface state which we dub 'descendent state' to form near the Fermi level due to the strong hybridization with the FM states at the same momentum. Such 'descendent state' carries a sizable weight of the original Dirac interface state and thus inherit the localization on the interface and the same Rashba-type spin-momentum locking. We propose that the 'descendent state' may be an important source of the experimentally observed large spin-transfer torque in the TI-FM heterostructure.

3.2.1 Introduction

Topological insulator(TI)-based heterostructures have become appealing candidates for spintronics due to the Dirac surface states which exhibit the spin-momentum locking with opposite Rashba spin-windings on opposite surfaces[58]. In particular, large spin-transfer torques comparable to conventional heavy-metal-based structures have been reported in three-dimensional (3D) TI-based bilayers[118, 34]. Although large signals from the spin-momentum-locked Dirac surface states on the interface have been predicted in TI-ferromagnetic insulator heterostructures[111], the materials involved in experiments are often ferromagnetic metals (FM)[118] since ferromagnetic insulators are rare. While data analysis attributed the observed spin-transfer torques to an interface state with a spin-winding in the same direction as the Dirac state in pristine TI on the surface in contact with ferromagnetic layer[118, 35], the identity of this state remains elusive. This is because this Dirac surface state is

very likely to be buried way below the raised chemical potential or even destroyed when hybridized with a large amount of FM states under an Ohmic contact.

The impacts on the primitive Dirac surface state localized at the interface (henceforth referred to as the 'Dirac interface state') from heterostructure formation have been investigated for various materials. In the cases of TI-insulator bilayers, first-principles studies have found that interface states localized a bit deeper into the interface appear near the Fermi level E_F with Dirac-like dispersion, while the original Dirac surface states are shifted way below E_F due to band-bending potentials, which are induced by the mismatch between chemical potentials [101, 119, 46, 128]. As for TI-metal heterostructures, effective model studies have found Dirac interface states becoming diffusive under weak TI-metal coupling[29] while first-principles studies have reported no spin-momentum-locked interface states for various metals[155]. In particular, severe hybridization is expected for cases where electrons in the Dirac interface states are coupled to many itinerant electrons with similar momenta and energies from a metal slab with much higher chemical potential. Such a scenario where itinerant electrons couple with a localized state has been generically described by the Fano-Anderson model to the lowest order[110, 9, 61]. Fano coupling involving enough extended states can produce a new long-lived localized state sitting outside of the metal band which carries substantial weight of the original localized state[110]. This 'descendent state' suggests the identity of the interface state with the same spin-winding as the Dirac interface state which lead to the large spin-transfer torque probed in the TI-FM heterostructure.

Our goal is to study the fate of the Dirac interface state in contact with an FM slab that has a much higher E_F and many states overlapping with the Dirac interface state in energy and momentum. In this article, we take two complementary approaches: we construct a simple microscopic model and perform first-principles calculations, including the hybridization between the metal states and the Dirac cone in such a TI-FM bilayer. By examining spectroscopic properties, we identify the new interface state near E_F as the 'descendent' state, which is localized slightly deeper into the TI layer and inherits the spin texture of the original Dirac cone. The features obtained from the microscopic model agree with those from the first-principles-based simulations of the TI-FM bilayer. We propose that the descendent states may be an important source of the recently observed large spin-transfer torque in Bi_2Se_3-Py heterostructure[118]. The article is structured as follows: In Sec. II, we construct a lattice model for a TI-FM heterostructure with hybridization in the spirit of Fano-Anderson model. In Sec. III, we study the spectroscopic properties of the model and the properties of the newly formed interface states. In Secs. IV and V, we present a first-principles study on Bi_2Se_3-Ni bilayer using density functional theory (DFT) and compare the results to those from our lattice model. In Sec. VI, we summarize our results and address open questions.

3.2.2 Lattice model for a TI-FM bilayer in the presence of hybridization

Generically the coupling between a localized state f with energy ϵ^0 and itinerant electrons c_k with energy E_k can be described by Fano model[110] $H_F = \epsilon^0 f^\dagger f +$

$\sum_k E_k^0 c_k^\dagger c_k + g_k(c_k^\dagger f + f^\dagger c_k)$, where g_k is the coupling strength. Ref. [9] pointed out that H_F can be used to model the lowest order interaction between a helical surface state and a metal bulk band, i.e. hybridization. The hybridized spectral function of the surface state f shows that the surface state not only acquire a finite lifetime, but also 'give birth to' one new long-lived surface state next to each of the metal band edge. We thus dub the new surface states the 'descendent states' of the mother surface state. As the hybridization strength g_k increases, the lifetime of the original surface state shortens while both the weights of the mother state carried by the descendent states and the gap to the metal band edges increase.

To examine the formation of descendent states in a TI-FM bilayer, we construct a tight-binding model capturing the coupling between the Dirac interface state with the extended states in the spirit of Fano model. The model for an $(N_{TI} + N_{FM})$-layer heterostructure reads $H_0 = \sum_{\mathbf{k}_\parallel} H_0(\mathbf{k}_\parallel)$ with

$$H_0(\mathbf{k}_\parallel) = \sum_{j=1}^{N_{TI}} H_{TI}(\mathbf{k}_\parallel, j) + \sum_{j=N_{TI}+1}^{N_{TI}+N_{FM}} H_{FM}(\mathbf{k}_\parallel, j), \tag{3.20}$$

where $\mathbf{k}_\parallel = (k_x, k_y)$ is the in-plane momentum, j labels the layers stacked in z direction, H_{TI} and H_M are Hamiltonians for a N_{TI}-layer TI slab and a N_{FM}-layer FM slab stacked in z direction.

$H_{TI}(\mathbf{k}_\parallel, j)$ is a four-band microscopic model descibing a quintuple layer j of pristine TI[61] in the presence of a band-bending potential created by the mismatch between the Fermi levels of the TI and FM:

$$H_{TI}(\mathbf{k}_\parallel, j) = (\mathbb{M} + \mathbb{V})\, c^\dagger_{\mathbf{k}_\parallel, j} c_{\mathbf{k}_\parallel, j} + \mathbb{T} c^\dagger_{\mathbf{k}_\parallel, j+1} c_{\mathbf{k}_\parallel, j} + H.c., \tag{3.21}$$

where $\mathbb{M}$, $\mathbb{T}$ and $\mathbb{V}$ are 4×4 matrices in the basis of $|\uparrow, P_1\rangle$, $|\uparrow, P_2\rangle$, $|\downarrow, P_1\rangle$, and $|\downarrow, P_2\rangle$ with $\uparrow/\downarrow$ being spin and $P_{1/2}$ being P_z orbitals of Bi/Se atoms. Here $\mathbb{M}$

and $\mathbb{T}$ contain tight-binding parameterization for pure Bi_2Se_3 [61, 186], while $\mathbb{V} = V(\mathbf{k}_\parallel, j)\mathbb{I}_{4\times4}$ is the potential well which forms near the interface when the TI has a lower Fermi level than the FM. For simplicity, we assume the potential to be momentum $\mathbf{k}_\parallel$-independent and has a spatial profile of $V(j) = V_0 e^{-\eta(N_{TI}-j)}$ based on the potential shapes in various TI-based bilayers obtained in ab initio calculations[155]. The depth of the well V_0 is approximately the Fermi level-difference between the two materials. For our purpose of demonstrating the hybridization effect on the Dirac interface state, we choose the width $1/\eta$ to be small enough such that no additional quantum well state forms.

As for the FM slab, we model each layer j by a simple two-band model

$$H_M(\mathbf{k}_\parallel, j) = \mathbf{m}\, c^\dagger_{\mathbf{k}_\parallel,j} c_{\mathbf{k}_\parallel,j} + \mathbf{t}\, c^\dagger_{\mathbf{k}_\parallel,j+1} c_{\mathbf{k}_\parallel,j}, \tag{3.22}$$

where $\mathbf{m} = (m_{\mathbf{k}_\parallel,j} - \mu_{FM})\mathbf{1}_{2\times2} + \Delta\sigma_x$ and $\mathbf{t} = t_z\mathbf{1}_{2\times2}$ are 2×2 matrices in spin basis. Here, $m_{\mathbf{k}_\parallel,j} = -t_\parallel \cos(k_\parallel a)$ is the dispersion given by in-plane hopping $t_\parallel$ with in-plane lattice constant a, μ_{FM} is the Fermi level, t_z is the hopping in z direction, and Δ is the exchange energy where we choose the magnetization to be in the x direction. The parameters of the FM layer are chosen such that the FM bands overlap with the Dirac interface branch in both momentum $\mathbf{k}_\parallel$ and energy [see Fig. 3.6(b)].

In the absence of hybridization, the bilayer Hamiltonian $H_0(\mathbf{k}_\parallel)$ can be diagonalized into

$$\begin{aligned} H_0(\mathbf{k}_\parallel) =& (\epsilon^0_{\mathbf{k}_\parallel} - \mu_{TI}) d^{0\dagger}_{\mathbf{k}_\parallel} d^0_{\mathbf{k}_\parallel} \\ &+ \sum_{\alpha=1}^{4N_{TI}-1} (E^0_{TI,\alpha,\mathbf{k}_\parallel} - \mu_{TI}) b^{0\dagger}_{\alpha,\mathbf{k}_\parallel} b^0_{\alpha,\mathbf{k}_\parallel} \\ &+ \sum_{\beta=1}^{2N_{FM}} (E^0_{FM,\beta,\mathbf{k}_\parallel} - \mu_{FM}) f^{0\dagger}_{\beta,\mathbf{k}_\parallel} f^0_{\beta,\mathbf{k}_\parallel}, \end{aligned} \tag{3.23}$$

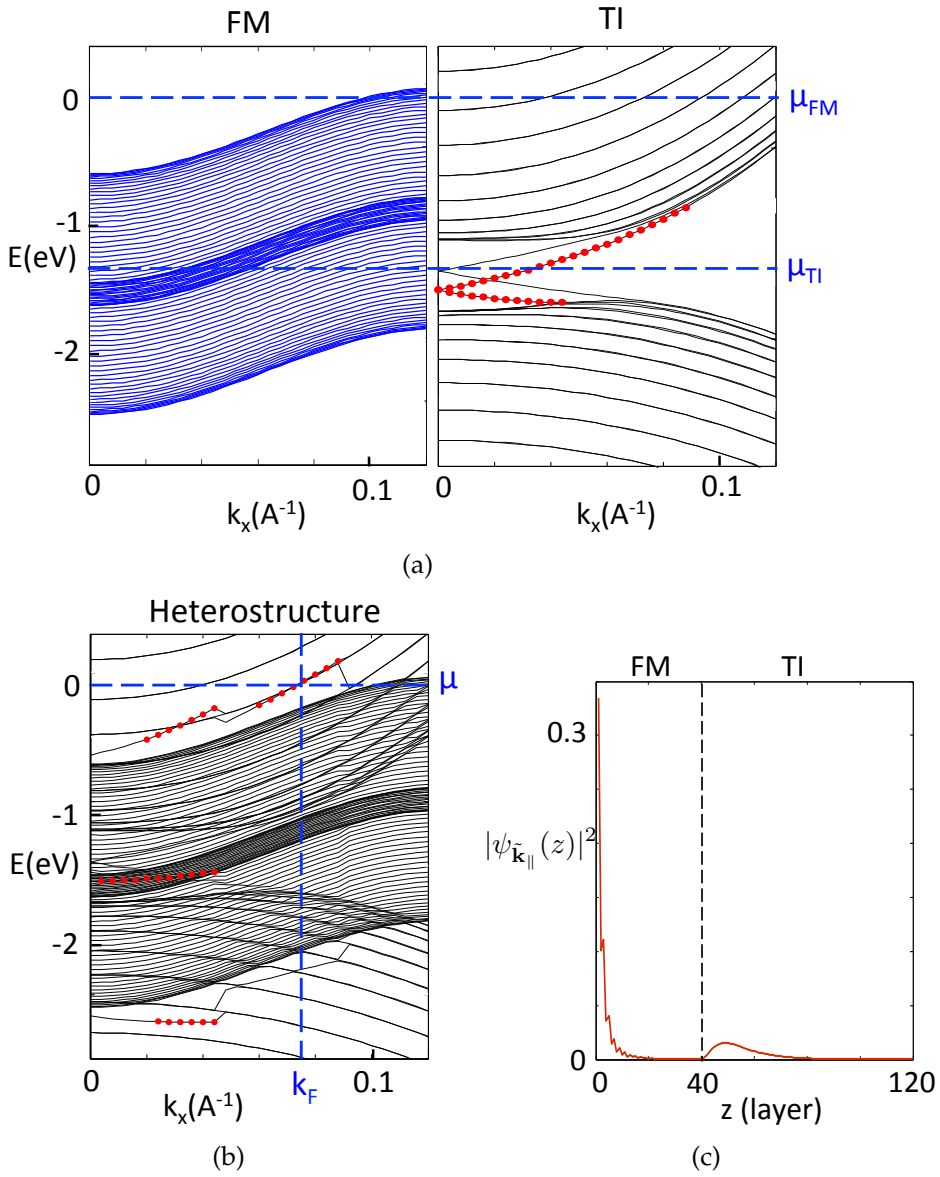

Figure 3.6: (a) The unhybridized dispersions of the FM slab (the left panel) and the TI slab (the right panel) of our lattice model along in-plane momentum $\mathbf{k}_\parallel = (k_x, 0)$. The upper and lower dashed lines represent the Fermi levels of the FM (μ_{FM}) and TI slab (μ_{TI}) respectively. (b) The band structure of the heterostructure in the presence of hybridization. The vertical and horizontal dashed lines represent Fermi level μ and the Fermi momentum $\tilde{\mathbf{k}}_\parallel = (k_F, 0)$ respectively. The hybridization strength $g_\beta(\mathbf{k}_\parallel)$ is given in the text with $\tilde{g}_0 = 0.078$ eV and $\tilde{g}_1 = 0.098$ eV. The red dots in (a) and (b) label the interface states consisting of a substantial weight $> 48\%$ on the TI side that has more than 80% of weight localized in the first 30% of the TI slab away from the interface. (c) The wavefunction of the interface state in the heterostructure (red dots in (b)) at the Fermi level μ with momentum (k_F,0). For all subfigures the slab thicknesses are $N_{TI} = 80$, $N_m = 40$, and the band-bending potential parameters are $V_0 = 1$ eV and $\eta = 0.3$ respectively.

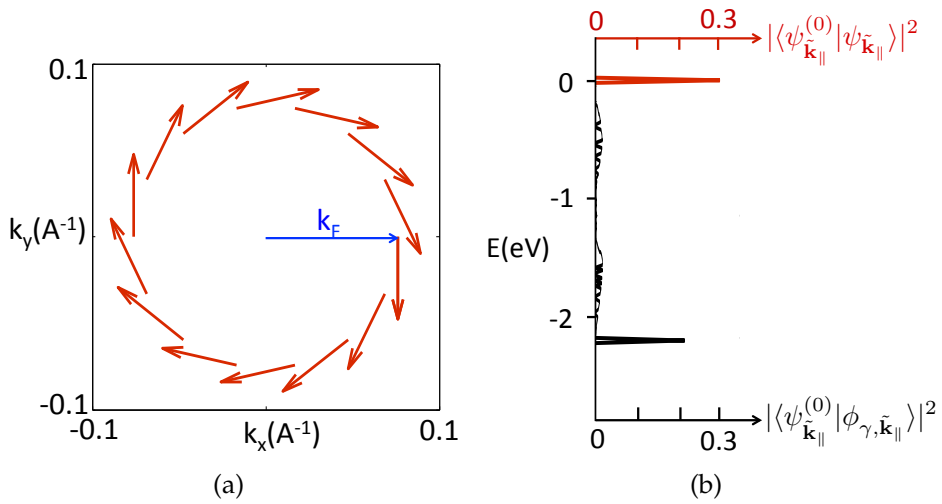

Figure 3.7: (a) The spin texture $(S_{x,\tilde{\mathbf{k}}_\parallel}, S_{y,\tilde{\mathbf{k}}_\parallel})$ of the interface state in the hybridized heterostructure at Fermi level μ with Fermi momenta $\tilde{\mathbf{k}}_\parallel = k_F(\cos\theta_k, \sin\theta_k)$. (b) The weight of the original Dirac interface state $|\psi^{(0)}_{\tilde{\mathbf{k}}_\parallel}\rangle$ carried by the eigenstates of the heterostructure along the momentum-cut at $\tilde{\mathbf{k}}_\parallel = (k_F, 0)$ (the verticle dashed line in Fig. 3.6(b)). The red (upper) horizontal axis and red curve are for the new interface state $|\psi_{\tilde{\mathbf{k}}_\parallel}\rangle$ at the Fermi level μ, and the black (lower) horizontal axis and black curve are for the rest of the eigenstates $|\phi_{\gamma,\tilde{\mathbf{k}}_\parallel}\rangle$.

where the four-spinors $d^0_{\mathbf{k}_\parallel}$ and $b^0_{\alpha,\mathbf{k}_\parallel}$ annihilate the Dirac interface state with energy $\epsilon^0_{\mathbf{k}_\parallel}$ [see red dots in Fig. 3.6(b)] and the rest of the eigenstates in the TI with energy $E^0_{TI,\alpha,\mathbf{k}_\parallel}$ [see black lines in Fig. 3.6(b)] respectively, and the two spinor $f^0_{\beta,\mathbf{k}_\parallel}$ annihilates the FM states with energy $E^0_{FM,\beta,\mathbf{k}_\parallel}$ [see blue lines in Fig. 3.6(b)]. Here, α and β label the TI states besides the Dirac interface state and the FM states respectively. The effect of the band-bending potential is to break the degeneracy between the two TI surfaces and shifts the dispersion of the Dirac interface state downwards [see Fig. 3.6(b)], which is expected when the localization length is smaller than the well width $1/\eta$[119].

Now we introduce the hybridization term which preserves in-plane mo-

menta $\mathbf{k}_\parallel$ and spin:

$$H'(\mathbf{k}_\parallel) = \sum_{\beta=1}^{2N_{FM}} g_\beta(\mathbf{k}_\parallel)\, f^{0\dagger}_{\beta,\mathbf{k}_\parallel} d^0_{\mathbf{k}_\parallel} + H.c., \tag{3.24}$$

where β runs over all the FM states at $\mathbf{k}_\parallel$. Here, we expect the strength $g_\beta(\mathbf{k}_\parallel)$ to be proportional to the 'spin-overlap' between the FM states and the spin-momentum-locked Dirac interface state:

$$g_\beta(\mathbf{k}_\parallel) = \tilde{g}_\beta(\mathbf{k}_\parallel)\langle\Psi^0_{\mathbf{k}_\parallel}|\Phi^0_{\beta,\mathbf{k}_\parallel}\rangle, \tag{3.25}$$

where $|\Phi^0_{\beta,\mathbf{k}_\parallel}\rangle \equiv \sum_{z'}\langle z'|\phi^0_{\beta,\mathbf{k}_\parallel}\rangle$ and $|\Psi^0_{\mathbf{k}_\parallel}\rangle \equiv \sum_{z,a}\langle z,a|\psi^0_{\mathbf{k}_\parallel}\rangle$ are 'coarse-grained' two-component ket spinors in spin basis for the FM and unhybridized Dirac interface states respectively. Here we define $|\phi^0_{\beta,\mathbf{k}_\parallel}\rangle \equiv f^{0\dagger}_{\beta,\mathbf{k}_\parallel}|0\rangle$, $|\psi^0_{\mathbf{k}_\parallel}\rangle \equiv d^{0\dagger}_{\mathbf{k}_\parallel}|0\rangle$, $z^{(\prime)}$ runs over the TI (FM) layers, and $a = P_1, P_2$ labels the TI atomic orbitals. For simplicity, we assume $\tilde{g}_\beta(\mathbf{k}_\parallel) = \tilde{g}(\mathbf{k}_\parallel)$ to be identical for all FM states β. To mimic our first-principle-calculated band structure later shown in Fig. 3.8(a), we further assume $\tilde{g}(\mathbf{k}_\parallel)$ to increase with the momentum and take $\tilde{g}_{\mathbf{k}_\parallel} = \tilde{g}_0 + \tilde{g}_1 k_\parallel$ with $\tilde{g}_0, \tilde{g}_1 > 0$. Finally, the full Hamiltonian including hybridization reads $H = \sum_{\mathbf{k}_\parallel} H(\mathbf{k}_\parallel)$ where

$$H(\mathbf{k}_\parallel) = H_0(\mathbf{k}_\parallel) + H'(\mathbf{k}_\parallel) \tag{3.26}$$

is given by Eq. (3.23) and (3.24).

3.2.3 The descendent state at the interface from the lattice model

The dispersion of H [see Fig. 3.6 (b)] shows that new interface states form above and below the FM bands with "remnant states", what are remaining of the Dirac interface states that survives within the FM bands, in between. Since the upper new interface branch emerges right above the upper band edge of FM, it

is likely to intersect the Fermi level μ of the heterostructure, which is approximately given by that of the FM slab μ_{FM}. We will thus focus only on this upper new interface branch for the rest of the article. To examine the properties of these states, we write the diagonalized full Hamiltonian at each $\mathbf{k}_\parallel$ as

$$H(\mathbf{k}_\parallel) = (\epsilon_{\mathbf{k}_\parallel} - \mu) d^\dagger_{\mathbf{k}_\parallel} d_{\mathbf{k}_\parallel} + \sum_{\gamma=1}^{4N_{TI}+2N_{FM}-1} (E_{\gamma,\mathbf{k}_\parallel} - \mu) b^\dagger_{\gamma,\mathbf{k}_\parallel} b_{\gamma,\mathbf{k}_\parallel}, \tag{3.27}$$

where $d_{\mathbf{k}_\parallel}$ annihilates the new interface state with energy $\epsilon_{\mathbf{k}_\parallel}$ above the FM upper band edge, and $b_{\gamma,\mathbf{k}_\parallel}$ annihilate the rest of the eigenstates labeled by γ with energy $E_{\gamma,\mathbf{k}_\parallel}$. Here we define $|\psi_{\mathbf{k}_\parallel}\rangle \equiv d^\dagger_{\mathbf{k}_\parallel}|0\rangle$, $|\phi_{\gamma,\mathbf{k}_\parallel}\rangle \equiv b^\dagger_{\gamma,\mathbf{k}_\parallel}|0\rangle$. The spatial profile of the upper new interface state is then given by $|\psi_{\mathbf{k}_\parallel}(z)|^2$, which is a function of z measured from the bottom of the FM slab along the finite dimension of the heterostructure. $|\psi_{\mathbf{k}_\parallel}(z)|^2$ at the Fermi momentum $\tilde{\mathbf{k}}_\parallel = (k_F, 0)$ [see Fig. 3.6(c)] shows that the TI portion of the upper new interface at the Fermi level localizes near the interface.

The new interface states at the Fermi level also has a clockwise Rashba-type spin-winding just as the origianl Dirac interface state, as shown by the in-plane spin expectation values $(S_{x,\tilde{\mathbf{k}}_\parallel}, S_{y,\tilde{\mathbf{k}}_\parallel})$ in Fig. 3.7(a). Here, $S_{x/y,\tilde{\mathbf{k}}_\parallel} \equiv \langle\psi_{\tilde{\mathbf{k}}_\parallel}|\hat{S}_{x/y}|\psi_{\tilde{\mathbf{k}}_\parallel}\rangle$ where $\hat{S}_{x/y} \equiv (\mathbb{1}_{2\times2} \otimes \mathbb{1}_{N_{FM}\times N_{FM}}) \oplus (\sigma_{x/y} \otimes \mathbb{1}_{2\times2} \otimes \mathbb{1}_{N_{TI}\times N_{TI}})$ are the spin operators projected onto the TI side. The spin magnitude of states with negative k_y is slightly smaller than that with positive k_y due to the spin-dependence of hybridization strength in Eq. (3.25), which vanishes in the limit where the ferromagnetic exchange energy Δ vanishes.

Finally, to determine the origin of this new interface state $|\psi_{\mathbf{k}_\parallel}\rangle$, we examine the weight of the original Dirac interface state $|\psi^0_{\mathbf{k}_\parallel}\rangle$ carried by the heterostructure eigenstates $|\psi_{\mathbf{k}_\parallel}\rangle$ and $|\phi_{\gamma,\mathbf{k}_\parallel}\rangle$. Fig. 3.7(b) shows the spectral distribution of the weight $\langle\psi^0_{\tilde{\mathbf{k}}_\parallel}|\psi_{\tilde{\mathbf{k}}_\parallel}\rangle$ and $\langle\psi^0_{\tilde{\mathbf{k}}_\parallel}|\phi_{\gamma,\tilde{\mathbf{k}}_\parallel}\rangle$ along the momentum-cut at $\tilde{\mathbf{k}}_\parallel = (k_F, 0)$ where two

peaks form outside of the FM band, which resembles that of the generic Fano model[110]. Specifically, the stronger peak is contributed by the new interface state on the Fermi level $|\psi_{\tilde{\mathbf{k}}_\parallel}\rangle$ [see the red curve] while the weaker peak buried below the Fermi level μ and the residues within the band are contributed by the rest of the states $|\phi_{\gamma,\tilde{\mathbf{k}}_\parallel}\rangle$ [see the black curve]. Hence we have demonstrated that the hybridization-induced new interface state on the Fermi level is the 'descendent state' of the original Dirac interface state, which thus inherits the wavefunction localization and spin texture of the mother state.

3.2.4 First-principles-based simulation of TI-FM bilayer

We simulate a TI-FM bilayer within density-functional theory (DFT) by using DFT code `VASP` [96]. We use the generalized gradient approximation (GGA) [131] for the exchange-correlation functional and projector-augmented wave (PAW) pseudopotentials [15, 96] Spin-orbit coupling (SOC) is included self-consistently with the DFT calculation. We construct a TI-FM bilayer by using a supercell consisting of a $1 \times 1\times$ 5-QL slab of Bi_2Se_3(111) beneath a Ni(111) slab of $\sqrt{3} \times \sqrt{3} \times L_z$, where L_z is 4 atomic layers. The in-plane lattice constant of the supercell is fixed as the experimental lattice constant of the TI, 4.143 [120]. This gives rise to a 4% compressive strain onto the Ni slab. The z coordinates of the QL nearest to the interface and the x, y, and z coordinates of all the Ni atoms in the supercell are relaxed until the residual forces are lower than 0.1 eV/, while keeping the atomic coordinates of the rest of the QLs in the TI remain fixed. The average distance between the TI and Ni layer is found to be 2.05 after the relaxation, which agrees well with the previous DFT calculation of the TI-FM bilayer [155]. A thick vacuum layer of 36.7 is added to the TI-FM bilayer and $11 \times 11 \times 1$

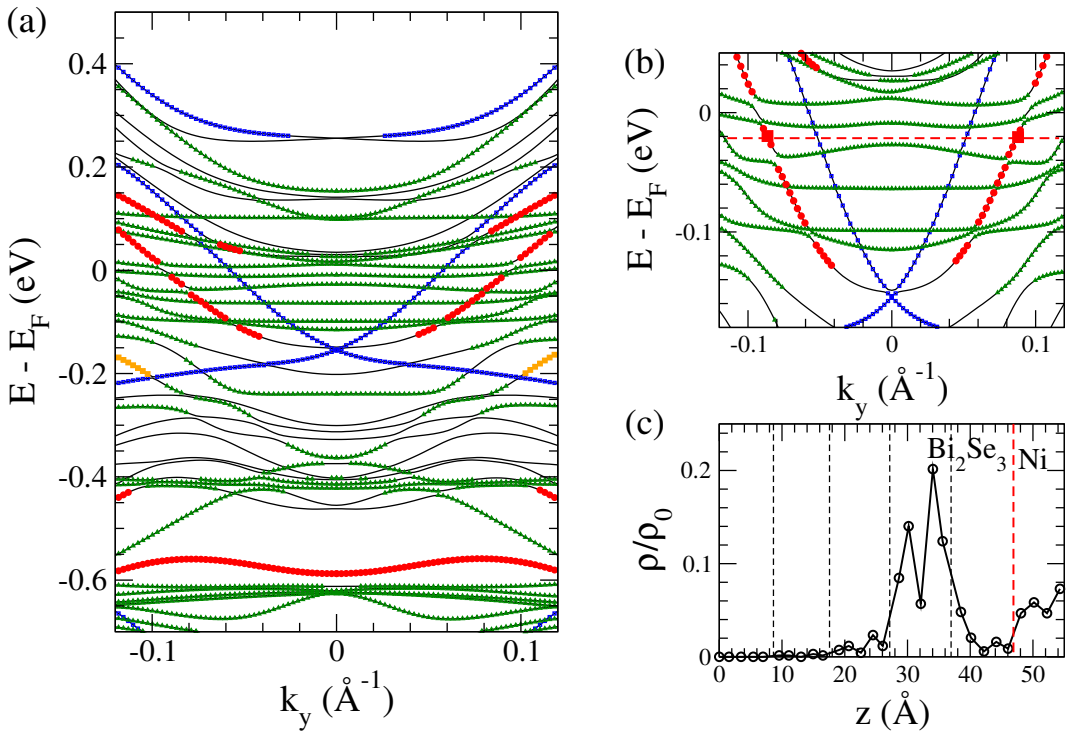

Figure 3.8: (a) DFT-calculated band structure of the TI-FM bilayer along the k_y axis and (b) zoom-in of (a) when the magnetization is along the y axis. (c) Electron density profile along the vertical direction computed at the k_y points marked as large red squares in (b). In (a) and (b), green triangles (blue squares) represent states localized into the Ni slab (the bottommost QL in contact to vacuum), while red circles are for states localized deeper into the TI slab as shown in (c), like "descendent states." Orange squares are for the states localized at the topmost QL.

k points are sampled in the geometry relaxation and calculations of electronic structure. The z axis is along the [111] direction and the y axis is along the [11$\bar{2}$] direction in the TI rhombohedral structure. In our simulation the magnetization of the Ni slab is in plane, such as parallel to the y axis.

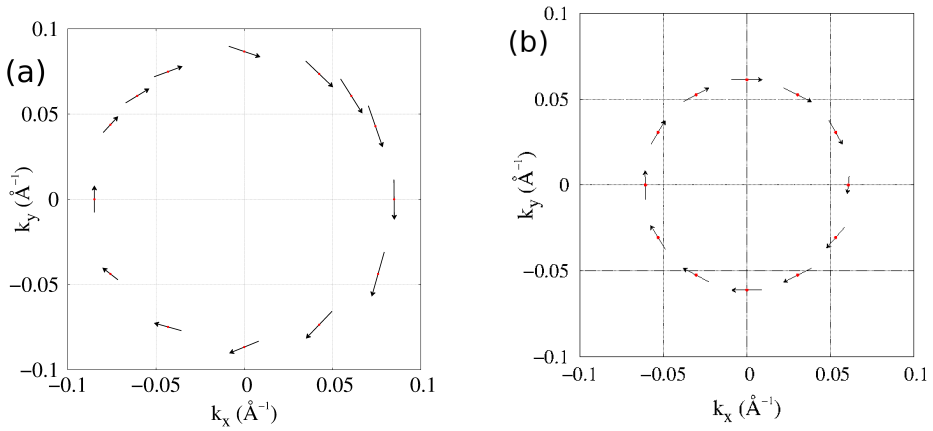

Figure 3.9: (a) DFT-calculated spin texture of the putative descendent state at the constant energy contour of 20 meV below E_F indicated as the red dashed line in Fig. 3.8(b) when the magnetization is along the y axis. (b) DFT-calculated spin texture of the descendent state at the constant energy contour of 50 meV below E_F when the magnetization is along the z axis.

3.2.5 The descendent state from the simulation

We calculate band structure of the TI-FM bilayer along different directions in the $k_x - k_y$ plane such as ϕ_k=0, $\pm\pi/6$, $\pi/4$, $\pm\pi/3$, $\pm 2\pi/3$, $3\pi/4$, $\pm 5\pi/6$, $\pm\pi/2$, and π, where ϕ_k is the azimuthal angle in the $k_x - k_y$ plane. The band structure along the k_y axis is shown in Fig. 3.8(a). In the vicinity of E_F the Dirac cone localized at the QL closest to the interface (topmost QL) are not found, although many bands from the Ni slab [green bands in Fig. 3.8(a)] appear. This absence of any Dirac state near E_F us distinct from the DFT results on TI-insulator bilayers [101, 46, 128]. Our DFT+SOC calculations show some charge transfer from the Ni slab to the TI slab, which is caused by the difference between the chemical potential of the TI and Ni slabs. This charge transfer shifts the Dirac surface states at the interface downward far below E_F and causes very strong hybridization with the Ni states. In addition, the strong hybridization also induces significant relaxations

in the z coordinates of the topmost QL due to the Ni slab. These two factors make it difficult to discern the original Dirac interface-state, which is consistent with the result of the hybridization model.

There are two classes of states near E_F. One class of states (orange squares in Fig. 3.8(a) and (b)) are localized at the top-most QL with energies in the vicinity of -0.2 eV. But these states extend only along k_y direction near $k_y = \pm 0.1^{-1}$. These states are reminiscent of the "remnant states" found in the hybridization model. The other more prominent class of states (red squares in Fig. 3.8(a) and (b), wave function distribution shown in Fig. 3.8(a) and (b)) spanning all directions are localized into the topmost-1 QL along with a small contribution from the Ni slab. These states group into two subclasses: one with energy above that of the "remnant states" and the other with energy below the "remnant states". By contrast, DFT calculation on the TI-insulator bilayers found a single group of states localized into the topmost-1 QL, at energies higher that those of the top-most states. Moreover, these states that were interpreted to be originating from the quantum well states showed Dirac-like dispersion for unknown reasons. On the other hand, the states localized into topmost-1 QL in the present TI-FM bilayer resembles the descendent states of the hybridization model in that 2) they do not exhibit Dirac-like dispersion, 2) they come in two sub-classes with an energy separation.

In addition, we examine the spin texture of the descendent state at a constant energy contour of 20 meV below E_F by computing expectation values of the x and y components of spin, $\langle S_{x,\tilde{\mathbf{k}}_\parallel} \rangle$ and $\langle S_{y,\tilde{\mathbf{k}}_\parallel} \rangle$ at the aforementioned different θ_k values, within DFT. As shown in Fig. 3.9(a), the DFT-calculated spin texture shows two main features: (i) almost spin-momentum locking with a small de-

viation along the k_y axis; (ii) the magnitude of the spin polarization depending on in-plane momentum. Both features are due to the in-plane magnetization of the Ni slab. We find that the contribution of the Ni slab to the descendent state varies from 10% to 30% with the in-plane momentum, which leads to the in-plane momentum dependent coupling to the Ni slab. Our DFT-calculated spin texture is comparable to that from the tight-binding model [Fig. 3.7(a)], considering that the in-plane magnetization of the Ni side in the tight-binding model is along the x axis.

We briefly discuss comparison of our DFT calculation to the previous DFT calculations of a TI-Ni bilayer [155] and TI-Co bilayer [117]. In these previous studies the spin-momentum locking we found above was either not reported [155] or found well below E_F [117]. There are two main differences between ours and the previous DFT calculations in addition to a different FM layer in Ref. [117]: (i) a different magnetization direction of the FM layer and (ii) different spatial localization of the state investigated for the spin-momentum locking. Between the two differences, the second is a major factor. We propose that the descendent state near E_F contributes to the large enhancement of the spin-transfer torque in the TI-FM bilayer in experiment [118], while the previous studies were searching for the states localized at the topmost QL. We use the in-plane magnetization taking the recent experiment [118] into account, while the latter studies [155, 117] considered out-of-plane magnetization due different experimental set-ups. In our DFT+SOC calculation, when the magnetization is out of plane, we find that the similar descendent state appears near 50 meV below E_F with the similar electron localization to that shown in Fig. 3.9(a), and that the descendent state has the spin-momentum locking as shown in Fig. 3.9(b).

3.2.6 Conclusion

We build a simple lattice model in the spirit of Fano-Anderson model and perform first-principles-based simulations in order to address the fate of the primitive Dirac interface state in TI-FM bilayers under large charge transfer and severe hybridization with many metallic states overlapping in momentum and energy. Both the tight-binding model and simulations showed that while destroying the Dirac interface state, a large enough hybridization could also create a new 'descendent' state near the Fermi level which inherits both the spatial localization on the interface and the Rashba-type spin-winding (spin-momentum locking). Our finding suggests the hybridization-induced 'descendent' state to be a possible candidate for the source which contributes to the experimentally observed large spin-transfer torque in TI-FM bilayers. While the hybridization strength is material-dependent, our simple model provides a generic way to describe the hybridization effect for the experimentally relevant cases where the Dirac interface state overlaps with many FM states.

BIBLIOGRAPHY

[1] D. F. Agterberg and R. P. Kaur. Magnetic-field-induced helical and stripe phases in rashba superconductors. *Phys. Rev. B*, 75:064511, Feb 2007.

[2] Jason Alicea. Majorana fermions in a tunable semiconductor device. *Phys. Rev. B*, 81:125318, Mar 2010.

[3] Carmine Autieri, Mario Cuoco, and Canio Noce. Collective properties of eutectic ruthenates: Role of nanometric inclusions. *Phys. Rev. B*, 85:075126, Feb 2012.

[4] Namrata Bansal, Yong Seung Kim, Matthew Brahlek, Eliav Edrey, and Seongshik Oh. Thickness-independent transport channels in topological insulator bi_2se_3 thin films. *Phys. Rev. Lett.*, 109:116804, Sep 2012.

[5] Maissam Barkeshli and Xiao-Liang Qi. Topological response theory of doped topological insulators. *Phys. Rev. Lett.*, 107:206602, Nov 2011.

[6] E. Berg, E. Fradkin, E.-A. Kim, S. A. Kivelson, V. Oganesyan, J. M. Tranquada, and S. C. Zhang. Dynamical layer decoupling in a stripe-ordered high-T_c superconductor. *Phys. Rev. Lett.*, 99:127003, Sep 2007.

[7] Doron L. Bergman. Axion response in gapless systems. *Phys. Rev. Lett.*, 107:176801, Oct 2011.

[8] Doron L. Bergman and Gil Refael. Bulk metals with helical surface states. *Phys. Rev. B*, 82:195417, Nov 2010.

[9] Doron L. Bergman and Gil Refael. Bulk metals with helical surface states. *Phys. Rev. B*, 82:195417, Nov 2010.

[10] B. Andrei Bernevig, Taylor L. Hughes, and Shou-Cheng Zhang. Quantum spin hall effect and topological phase transition in hgte quantum wells. *Science*, 314(5806):1757–1761, 2006.

[11] Marco Bianchi, Dandan Guan, Shining Bao, Jianli Mi, Bo Brummerstedt Iversen, Philip D.C. King, and Philip Hofmann. Coexistence of the topological state and a two-dimensional electron gas on the surface of bi2se3. *Nat Commun*, 1:128–, November 2010.

[12] Annica M. Black-Schaffer and Sebastian Doniach. Resonating valence bonds and mean-field *d*-wave superconductivity in graphite. *Phys. Rev. B*, 75:134512, Apr 2007.

[13] P. E. Blöchl. Projector augmented-wave method. *Phys. Rev. B*, 50:17953–17979, 1994.

[14] P. E. Blöchl. Projector augmented-wave method. *Phys. Rev. B*, 50:17953–17979, Dec 1994.

[15] P. E. Blöchl. Projector augmented-wave method. *Phys. Rev. B*, 50:17953–17979, Dec 1994.

[16] H. W. J. Blöte, John L. Cardy, and M. P. Nightingale. Conformal invariance, the central charge, and universal finite-size amplitudes at criticality. *Phys. Rev. Lett.*, 56:742–745, Feb 1986.

[17] B. Burganov, C. Adamo, A. Mulder, M. Uchida, P. D. C. King, J. W. Harter, D. E. Shai, A. S. Gibbs, A. P. Mackenzie, R. Uecker, M. Bruetzam, M. R. Beasley, C. J. Fennie, D. G. Schlom, and K. M. Shen. Strain control of fermiology and many-body interactions in two-dimensional ruthenates. *Phys. Rev. Lett.*, 116:197003, May 2016.

[18] B. Burganov, C. Adamo, A. Mulder, M. Uchida, P. D. C. King, J. W. Harter, D. E. Shai, A. S. Gibbs, A. P. Mackenzie, R. Uecker, M. Bruetzam, M. R. Beasley, C. J. Fennie, D. G. Schlom, and K. M. Shen. Strain control of fermiology and many-body interactions in two-dimensional ruthenates. *Phys. Rev. Lett.*, 116:197003, May 2016.

[19] A. A. Burkov and D. G. Hawthorn. Spin and charge transport on the surface of a topological insulator. *Phys. Rev. Lett.*, 105:066802, Aug 2010.

[20] Ting Cao, Gang Wang, Wenpeng Han, Huiqi Ye, Chuanrui Zhu, Junren Shi, Qian Niu, Pingheng Tan, Enge Wang, Baoli Liu, and Ji Feng. Valley-selective circular dichroism of monolayer molybdenum disulphide. *Nat Commun*, 3:887–, June 2012.

[21] Y. L. Chen, J. G. Analytis, J.-H. Chu, Z. K. Liu, S.-K. Mo, X. L. Qi, H. J. Zhang, D. H. Lu, X. Dai, Z. Fang, S. C. Zhang, I. R. Fisher, Z. Hussain, and Z.-X. Shen. Experimental realization of a three-dimensional topological insulator, bi2te3. *Science*, 325(5937):178–181, 2009.

[22] Z. Chi, F. Yen, F. Peng, J. Zhu, Y. Zhang, X. Chen, Z. Yang, X. Liu, Y. Ma, Y. Zhao, T. Kagayama, and Y. Iwasa. Ultrahigh Pressure Superconductivity in Molybdenum Disulfide. *ArXiv e-prints*, March 2015.

[23] Gil Young Cho, Jens H. Bardarson, Yuan-Ming Lu, and Joel E. Moore. Superconductivity of doped weyl semimetals: Finite-momentum pairing and electronic analog of the ^{3}he-*a* phase. *Phys. Rev. B*, 86:214514, Dec 2012.

[24] Sungjae Cho, Brian Dellabetta, Alina Yang, John Schneeloch, Zhijun Xu, Tonica Valla, Genda Gu, Matthew J. Gilbert, and Nadya Mason. Symmetry protected josephson supercurrents in three-dimensional topological insulators. *Nat Commun*, 4:1689–, April 2013.

[25] Jiun-Haw Chu, Hsueh-Hui Kuo, James G. Analytis, and Ian R. Fisher. Divergent nematic susceptibility in an iron arsenide superconductor. *Science*, 337(6095):710–712, 2012.

[26] A. V. Chubukov, D. V. Efremov, and I. Eremin. Magnetism, superconductivity, and pairing symmetry in iron-based superconductors. *Phys. Rev. B*, 78:134512, 2008.

[27] Andrey V. Chubukov. Kohn-luttinger effect and the instability of a two-dimensional repulsive fermi liquid at T =0. *Phys. Rev. B*, 48:1097–1104, Jul 1993.

[28] Suk Bum Chung, Hendrik Bluhm, and Eun-Ah Kim. Stability of half-quantum vortices in $p_x + ip_y$ superconductors. *Phys. Rev. Lett.*, 99:197002, 2007.

[29] Dimitrie Culcer, E. H. Hwang, Tudor D. Stanescu, and S. Das Sarma. Two-dimensional surface charge transport in topological insulators. *Phys. Rev. B*, 82:17, Oct 2010.

[30] P. J. Curran, S. J. Bending, W. M. Desoky, A. S. Gibbs, S. L. Lee, and A. P. Mackenzie. Search for spontaneous edge currents and vortex imaging in sr_2Ruo_4 mesostructures. *Phys. Rev. B*, 89:144504, Apr 2014.

[31] Tanmoy Das and Kapildeb Dolui. Superconducting dome in mos_2 and $tise_2$ generated by quasiparticle-phonon coupling. *Phys. Rev. B*, 91:094510, Mar 2015.

[32] Sankar Das Sarma, Chetan Nayak, and Sumanta Tewari. Proposal to sta-

bilize and detect half-quantum vortices in strontium ruthenate thin films: Non-abelian braiding statistics of vortices in a $p_x + ip_y$ superconductor. *Phys. Rev. B*, 73:220502, Jun 2006.

[33] A. Di Bernardo, O. Millo, M. Barbone, H. Alpern, Y. Kalcheim, U. Sassi, A. K. Ott, D. De Fazio, D. Yoon, M. Amado, A. C. Ferrari, J. Linder, and J. W. A. Robinson. p-wave triggered superconductivity in single-layer graphene on an electron-doped oxide superconductor. *Nature Communications*, 8:14024–, January 2017.

[34] Yabin Fan, Pramey Upadhyaya, Xufeng Kou, Murong Lang, So Takei, Zhenxing Wang, Jianshi Tang, Liang He, Li-Te Chang, Mohammad Montazeri, Guoqiang Yu, Wanjun Jiang, Tianxiao Nie, Robert N. Schwartz, Yaroslav Tserkovnyak, and Kang L. Wang. Magnetization switching through giant spin??orbit torque in a magnetically doped topological insulator heterostructure. *Nat Mater*, 13(7):699–704, July 2014.

[35] M. H Fischer, A. Vaezi, A. Manchon, and E.-A. Kim. Spin-Torque Generation in Topological-Insulator-Based Heterostructures. *ArXiv e-prints*, May 2013.

[36] Mark H. Fischer and Erez Berg. Fluctuation and strain effects in a chiral p-wave superconductor. *Phys. Rev. B*, 93:054501, Feb 2016.

[37] Mark H. Fischer and Jun Goryo. Symmetry and gap classification of nonsymmorphic srptas. *Journal of the Physical Society of Japan*, 84(5):054705, 2015.

[38] Mark H. Fischer, Titus Neupert, Christian Platt, Andreas P. Schnyder, Werner Hanke, Jun Goryo, Ronny Thomale, and Manfred Sigrist. Chiral d-wave superconductivity in srptas. *Phys. Rev. B*, 89:020509, Jan 2014.

[39] Mark H. Fischer, Abolhassan Vaezi, Aurelien Manchon, and Eun-Ah Kim. Spin-torque generation in topological insulator based heterostructures. *Phys. Rev. B*, 93:125303, Mar 2016.

[40] D. Forsythe, S. R. Julian, C. Bergemann, E. Pugh, M. J. Steiner, P. L. Alireza, G. J. McMullan, F. Nakamura, R. K. W. Haselwimmer, I. R. Walker, S. S. Saxena, G. G. Lonzarich, A. P. Mackenzie, Z. Q. Mao, and Y. Maeno. Evolution of fermi-liquid interactions in sr2ruo4 under pressure. *Phys. Rev. Lett.*, 89:166402, Sep 2002.

[41] Liang Fu. Hexagonal warping effects in the surface states of the topological insulator bi_2te_3. *Phys. Rev. Lett.*, 103:266801, Dec 2009.

[42] Liang Fu and C. L. Kane. Superconducting proximity effect and majorana fermions at the surface of a topological insulator. *Phys. Rev. Lett.*, 100:096407, Mar 2008.

[43] Peter Fulde and Richard A. Ferrell. Superconductivity in a strong spin-exchange field. *Phys. Rev.*, 135:A550–A563, Aug 1964.

[44] Ion Garate and M. Franz. Inverse spin-galvanic effect in the interface between a topological insulator and a ferromagnet. *Phys. Rev. Lett.*, 104:146802, Apr 2010.

[45] H. Goudarzi, M. Khezerlou, H. Sedghi, and A. Ghorbai. Spin-triplet f-wave symmetry in superconducting monolayer MoS_2. *ArXiv e-prints*, January 2017.

[46] K. Govaerts, K. Park, C. De Beule, B. Partoens, and D. Lamoen. Effect of bi bilayers on the topological states of bi_2se_3: A first-principles study. *Phys. Rev. B*, 90:155124, Oct 2014.

[47] Christoph J. Halboth and Walter Metzner. Renormalization-group analysis of the two-dimensional hubbard model. *Phys. Rev. B*, 61:7364–7377, Mar 2000.

[48] F. D. M. Haldane. Model for a quantum hall effect without landau levels: Condensed-matter realization of the "parity anomaly". *Phys. Rev. Lett.*, 61:2015–2018, Oct 1988.

[49] F. D. M. Haldane. O(3) nonlinear σ model and the topological distinction between integer- and half-integer-spin antiferromagnets in two dimensions. *Phys. Rev. Lett.*, 61:1029–1032, Aug 1988.

[50] M. H. Hamidian, S. D. Edkins, S. H. Joo, A. Kostin, H. Eisaki, S. Uchida, M. J. Lawler, E.-A. Kim, A. P. Mackenzie, K. Fujita, J. Lee, and J. C. Séamus Davis. Detection of a Pair Density Wave State in Bi_2Sr_2CaCu_2O_8 + x Using Scanned Josephson Tunneling. *ArXiv e-prints*, November 2015.

[51] M. Z. Hasan and C. L. Kane. Colloquium. *Rev. Mod. Phys.*, 82:3045–3067, Nov 2010.

[52] M. W. Haverkort, I. S. Elfimov, L. H. Tjeng, G. A. Sawatzky, and A. Damascelli. Strong spin-orbit coupling effects on the fermi surface of sr_2ruo_4 and sr_2rho_4. *Phys. Rev. Lett.*, 101:026406, Jul 2008.

[53] Clifford W. Hicks, Mark E. Barber, Stephen D. Edkins, Daniel O. Brodsky, and Andrew P. Mackenzie. Piezoelectric-based apparatus for strain tuning. *Review of Scientific Instruments*, 85(6), 2014.

[54] Clifford W. Hicks, Daniel O. Brodsky, Edward A. Yelland, Alexandra S. Gibbs, Jan A. N. Bruin, Mark E. Barber, Stephen D. Edkins, Keigo Nishimura, Shingo Yonezawa, Yoshiteru Maeno, and Andrew P. Mackenzie. Strong increase of tc of sr2ruo4 under both tensile and compressive strain. *Science*, 344(6181):283–285, April 2014.

[55] C. Honerkamp, M. Salmhofer, N. Furukawa, and T. M. Rice. Breakdown of the landau-fermi liquid in two dimensions due to umklapp scattering. *Phys. Rev. B*, 63:035109, Jan 2001.

[56] D. Hsieh, D. Qian, L. Wray, Y. Xia, Y. S. Hor, R. J. Cava, and M. Z. Hasan. A topological dirac insulator in a quantum spin hall phase. *Nature*, 452(7190):970–974, April 2008.

[57] D. Hsieh, Y. Xia, D. Qian, L. Wray, J. H. Dil, F. Meier, J. Osterwalder, L. Patthey, J. G. Checkelsky, N. P. Ong, A. V. Fedorov, H. Lin, A. Bansil, D. Grauer, Y. S. Hor, R. J. Cava, and M. Z. Hasan. A tunable topological insulator in the spin helical dirac transport regime. *Nature*, 460(7259):1101–1105, August 2009.

[58] D. Hsieh, Y. Xia, D. Qian, L. Wray, J. H. Dil, F. Meier, J. Osterwalder, L. Patthey, J. G. Checkelsky, N. P. Ong, A. V. Fedorov, H. Lin, A. Bansil, D. Grauer, Y. S. Hor, R. J. Cava, and M. Z. Hasan. A tunable topological insulator in the spin helical dirac transport regime. *Nature*, 460(7259):1101–1105, August 2009.

[59] D. Hsieh, Y. Xia, L. Wray, D. Qian, A. Pal, J. H. Dil, J. Osterwalder, F. Meier, G. Bihlmayer, C. L. Kane, Y. S. Hor, R. J. Cava, and M. Z. Hasan. Observation of unconventional quantum spin textures in topological insulators. *Science*, 323(5916):919–922, 2009.

[60] Yi-Ting Hsu, Weejee Cho, Alejandro Federico Rebola, Bulat Burganov, Carolina Adamo, Kyle M. Shen, Darrell G. Schlom, Craig J. Fennie, and Eun-Ah Kim. Manipulating superconductivity in ruthenates through fermi surface engineering. *Phys. Rev. B*, 94:045118, Jul 2016.

[61] Yi-Ting Hsu, Mark H. Fischer, Taylor L. Hughes, Kyungwha Park, and Eun-Ah Kim. Effects of surface-bulk hybridization in three-dimensional topological metals. *Phys. Rev. B*, 89:205438, May 2014.

[62] Yi-Ting Hsu, Abolhassan Vaezi, Mark H. Fischer, and Eun-Ah Kim. Topological superconductivity in monolayer transition metal dichalcogenides. *Nature Communications*, 8:14985–, April 2017.

[63] Hui Hu and Xia-Ji Liu. Mean-field phase diagrams of imbalanced fermi gases near a feshbach resonance. *Phys. Rev. A*, 73:051603, May 2006.

[64] K. Ishida, H. Mukuda, Y. Kitaoka, K. Asayama, Z. Q. Mao, Y. Mori, and Y. Maeno. Spin-triplet superconductivity in sr2ruo4 identified by 17o knight shift. *Nature*, 396(6712):658–660, December 1998.

[65] D. A. Ivanov. Non-abelian statistics of half-quantum vortices in *p*-wave superconductors. *Phys. Rev. Lett.*, 86:268–271, Jan 2001.

[66] J. Jang, D. G. Ferguson, V. Vakaryuk, R. Budakian, S. B. Chung, P. M. Goldbart, and Y. Maeno. Observation of half-height magnetization steps in sr2ruo4. *Science*, 331(6014):186–188, January 2011.

[67] Sanghyun Jo, Davide Costanzo, Helmuth Berger, and Alberto F. Morpurgo. Electrostatically induced superconductivity at the surface of ws2. *Nano Letters*, 15(2):1197–1202, 2015. PMID: 25607653.

[68] Aaron M. Jones, Hongyi Yu, Nirmal J. Ghimire, Sanfeng Wu, Grant Aivazian, Jason S. Ross, Bo Zhao, Jiaqiang Yan, David G. Mandrus, Di Xiao, Wang Yao, and Xiaodong Xu. Optical generation of excitonic valley coherence in monolayer wse2. *Nat Nano*, 8(9):634–638, September 2013.

[69] Robert Joynt and Louis Taillefer. The superconducting phases of upt_3. *Rev. Mod. Phys.*, 74:235–294, Mar 2002.

[70] Alexandra Junck, Kun W. Kim, Doron L. Bergman, T. Pereg-Barnea, and Gil Refael. Transport through a disordered topological-metal strip. *Phys. Rev. B*, 87:235114, Jun 2013.

[71] Catherine Kallin. Chiral p-wave order in sr 2 ruo 4. *Reports on Progress in Physics*, 75(4):042501, 2012.

[72] Catherine Kallin. Chiral p-wave order in sr 2 ruo 4. *Reports on Progress in Physics*, 75(4):042501, 2012.

[73] Catherine Kallin and John Berlinsky. Chiral superconductors. *Reports on Progress in Physics*, 79(5):054502, 2016.

[74] C. L. Kane and E. J. Mele. Quantum spin hall effect in graphene. *Phys. Rev. Lett.*, 95:226801, Nov 2005.

[75] Andreas Karch. Surface plasmons and topological insulators. *Phys. Rev. B*, 83:245432, Jun 2011.

[76] Francoise Kidwingira, J. D. Strand, D. J. Van Harlingen, and Yoshiteru Maeno. Dynamical superconducting order parameter domains in sr2ruo4. *Science*, 314(5803):1267–1271, November 2006.

[77] Maximilian L. Kiesel, Christian Platt, Werner Hanke, Dmitry A. Abanin, and Ronny Thomale. Competing many-body instabilities and unconventional superconductivity in graphene. *Phys. Rev. B*, 86:020507, Jul 2012.

[78] Maximilian L. Kiesel, Christian Platt, Werner Hanke, Dmitry A. Abanin, and Ronny Thomale. Competing many-body instabilities and unconventional superconductivity in graphene. *Phys. Rev. B*, 86:020507, Jul 2012.

[79] Maximilian L. Kiesel, Christian Platt, Werner Hanke, and Ronny Thomale. Model evidence of an anisotropic chiral *d*+*id*-wave pairing state for the water-intercalated $\mathrm{na}_x\mathrm{coo}_2 \cdot y\mathbf{h}_2\mathbf{O}$ superconductor. *Phys. Rev. Lett.*, 111:097001, Aug 2013.

[80] Sunghun Kim, M. Ye, K. Kuroda, Y. Yamada, E. E. Krasovskii, E. V. Chulkov, K. Miyamoto, M. Nakatake, T. Okuda, Y. Ueda, K. Shimada, H. Namatame, M. Taniguchi, and A. Kimura. Surface scattering via bulk continuum states in the 3d topological insulator $\mathrm{bi}_2\mathrm{se}_3$. *Phys. Rev. Lett.*, 107:056803, Jul 2011.

[81] Yong Seung Kim, Matthew Brahlek, Namrata Bansal, Eliav Edrey, Gary A. Kapilevich, Keiko Iida, Makoto Tanimura, Yoichi Horibe, Sang-Wook Cheong, and Seongshik Oh. Thickness-dependent bulk properties and weak antilocalization effect in topological insulator $\mathrm{bi}_2\mathrm{se}_3$. *Phys. Rev. B*, 84:073109, Aug 2011.

[82] Hikari Kimura, R. P. Barber, S. Ono, Yoichi Ando, and R. C. Dynes. Scan-

ning josephson tunneling microscopy of single-crystal $bi_2sr_2cacu_2o_{8+\delta}$ with a conventional superconducting tip. *Phys. Rev. Lett.*, 101:037002, Jul 2008.

[83] P. D. C. King, R. C. Hatch, M. Bianchi, R. Ovsyannikov, C. Lupulescu, G. Landolt, B. Slomski, J. H. Dil, D. Guan, J. L. Mi, E. D. L. Rienks, J. Fink, A. Lindblad, S. Svensson, S. Bao, G. Balakrishnan, B. B. Iversen, J. Osterwalder, W. Eberhardt, F. Baumberger, and Ph. Hofmann. Large tunable rashba spin splitting of a two-dimensional electron gas in bi_2se_3. *Phys. Rev. Lett.*, 107:096802, Aug 2011.

[84] J. R. Kirtley, C. Kallin, C. W. Hicks, E.-A. Kim, Y. Liu, K. A. Moler, Y. Maeno, and K. D. Nelson. Upper limit on spontaneous supercurrents in sr_2Ruo_4. *Phys. Rev. B*, 76:014526, Jul 2007.

[85] Shunichiro Kittaka, Haruka Taniguchi, Shingo Yonezawa, Hiroshi Yaguchi, and Yoshiteru Maeno. Higher-tc superconducting phase in sr2ruo4 induced by uniaxial pressure. *Phys. Rev. B*, 81:180510, May 2010.

[86] Shunichiro Kittaka, Hiroshi Yaguchi, and Yoshiteru Maeno. Large enhancement of 3-k phase superconductivity in the sr2ruo4–ru eutectic system by uniaxial pressure. *J. Phys. Soc. Jpn.*, 78:103705–, 2009.

[87] K. v. Klitzing, G. Dorda, and M. Pepper. New method for high-accuracy determination of the fine-structure constant based on quantized hall resistance. *Phys. Rev. Lett.*, 45:494–497, Aug 1980.

[88] Mahito Kohmoto. Topological invariant and the quantization of the hall conductance. *Annals of Physics*, 160(2):343 – 354, 1985.

[89] W. Kohn and J. M. Luttinger. New mechanism for superconductivity. *Phys. Rev. Lett.*, 15:524–526, Sep 1965.

[90] Markus Konig, Hartmut Buhmann, Laurens W. Molenkamp, Taylor Hughes, Chao-Xing Liu, Xiao-Liang Qi, and Shou-Cheng Zhang. The quantum spin hall effect: Theory and experiment. *Journal of the Physical Society of Japan*, 77(3):031007, 2008.

[91] Markus Konig, Steffen Wiedmann, Christoph Brne Andreas Roth, Hartmut Buhmann, Laurens W. Molenkamp, Xiao-Liang Qi, and Shou-Cheng Zhang. Quantum spin hall insulator state in hgte quantum wells. *Science*, 318:766–770, 2007.

[92] G. Kresse and J. Furthmülle. Efficiency of ab-initio total energy calculations for metals and semiconductors using a plane-wave basis set. *Comp. Mat. Sci.*, 6(1):15–50, 1996.

[93] G. Kresse and J. Furthmüller. Efficient iterative schemes for *ab initio* total-energy calculations using a plane-wave basis set. *Phys. Rev. B*, 54:11169–11186, Oct 1996.

[94] G. Kresse and J. Furthmüller. Efficient iterative schemes for *ab initio* total-energy calculations using a plane-wave basis set. *Phys. Rev. B*, 54:11169–11186, Oct 1996.

[95] G. Kresse and J. Furthm?ller. Efficiency of ab-initio total energy calculations for metals and semiconductors using a plane-wave basis set. *Computational Materials Science*, 6(1):15 – 50, 1996.

[96] G. Kresse and D. Joubert. From ultrasoft pseudopotentials to the projector augmented-wave method. *Phys. Rev. B*, 59:1758–1775, Jan 1999.

[97] Y. Krockenberger, M. Uchida, K. S. Takahashi, M. Nakamura, M. Kawasaki, and Y. Tokura. Growth of superconducting sr2ruo4 thin films. *Appl. Phys. Lett.*, 97(8), 2010.

[98] K. Kuroda, M. Arita, K. Miyamoto, M. Ye, J. Jiang, A. Kimura, E. E. Krasovskii, E. V. Chulkov, H. Iwasawa, T. Okuda, K. Shimada, Y. Ueda, H. Namatame, and M. Taniguchi. Hexagonally deformed fermi surface of the 3d topological insulator bi_2se_3. *Phys. Rev. Lett.*, 105:076802, Aug 2010.

[99] A.I. Larkin and Y.N. Ovchinnikov. Inhomogeneous state of superconductors. *Sov. Phys. JETP*, 20:762, 1965.

[100] Duy Le, Alexei Barinov, Edwin Preciado, Miguel Isarraraz, Iori Tanabe, Takashi Komesu, Conrad Troha, Ludwig Bartels, Talat S Rahman, and Peter A Dowben. Spinorbit coupling in the band structure of monolayer wse 2. *Journal of Physics: Condensed Matter*, 27(18):182201, 2015.

[101] Alex Taekyung Lee, Myung Joon Han, and Kyungwha Park. Magnetic proximity effect and spin-orbital texture at the bi_2se_3/EuS interface. *Phys. Rev. B*, 90:155103, Oct 2014.

[102] Patrick A. Lee. Amperean pairing and the pseudogap phase of cuprate superconductors. *Phys. Rev. X*, 4:031017, Jul 2014.

[103] A. J. Li, X. Zhu, G. R. Stewart, and A. F. Hebard. Bi-2212/1T-TaS_2 Van der Waals junctions: Interplay of proximity induced high-T_c superconductivity and CDW order. *ArXiv e-prints*, March 2017.

[104] Jacob Linder, Annica M. Black-Schaffer, Takehito Yokoyama, Sebastian Doniach, and Asle Sudbø. Josephson current in graphene: Role of unconventional pairing symmetries. *Phys. Rev. B*, 80:094522, Sep 2009.

[105] Minhao Liu, Cui-Zu Chang, Zuocheng Zhang, Yi Zhang, Wei Ruan, Ke He, Li-li Wang, Xi Chen, Jin-Feng Jia, Shou-Cheng Zhang, Qi-Kun Xue, Xucun Ma, and Yayu Wang. Electron interaction-driven insulating ground state in bi_2se_3 topological insulators in the two-dimensional limit. *Phys. Rev. B*, 83:165440, Apr 2011.

[106] Y. C. Liu, F. C. Zhang, T. M. Rice, and Q. H. Wang. Theory of the Evolution of Superconductivity in Sr_2RuO_4 under Anisotropic Strain. *ArXiv e-prints*, April 2016.

[107] J. M. Lu, O. Zheliuk, I. Leermakers, N. F. Q. Yuan, U. Zeitler, K. T. Law, and J. T. Ye. Evidence for two-dimensional ising superconductivity in gated mos2. *Science*, 350(6266):1353–1357, 2015.

[108] A. P. Mackenzie, R. K. W. Haselwimmer, A. W. Tyler, G. G. Lonzarich, Y. Mori, S. Nishizaki, and Y. Maeno. Extremely strong dependence of superconductivity on disorder in sr_2ruo_4. *Phys. Rev. Lett.*, 80:161–164, Jan 1998.

[109] Y. Maeno, T. Ando, Y. Mori, E. Ohmichi, S. Ikeda, S. NishiZaki, and S. Nakatsuji. Enhancement of superconductivity of sr_2ruo_4 to 3 k by embedded metallic microdomains. *Phys. Rev. Lett.*, 81:3765–3768, Oct 1998.

[110] Gerald D. Mahan. *Many-Particle Physics*. Plenum, New York, N.Y., 3rd edition, 2000.

[111] Farzad Mahfouzi, Naoto Nagaosa, and Branislav K. Nikolić. Spin-orbit coupling induced spin-transfer torque and current polarization in topological-insulator/ferromagnet vertical heterostructures. *Phys. Rev. Lett.*, 109:166602, Oct 2012.

[112] S. Maiti and A. V. Chubukov. Superconductivity from repulsive interaction. In A. Avella and F. Mancini, editors, *American Institute of Physics Conference Series*, volume 1550 of *American Institute of Physics Conference Series*, pages 3–73, August 2013.

[113] Leyla Majidi and Reza Asgari. Valley- and spin-switch effects in molybdenum disulfide superconducting spin valve. *Phys. Rev. B*, 90:165440, Oct 2014.

[114] K. F. Mak, K. L. McGill, J. Park, and P. L. McEuen. The valley hall effect in mos2 transistors. *Science*, 344(6191):1489–1492, 2014.

[115] Kin Fai Mak, Keliang He, Jie Shan, and Tony F. Heinz. Control of valley polarization in monolayer mos2 by optical helicity. *Nat Nano*, 7(8):494–498, August 2012.

[116] Z. Q. Mao, Y. Mori, and Y. Maeno. Suppression of superconductivity in sr_2ruo_4 caused by defects. *Phys. Rev. B*, 60:610–614, Jul 1999.

[117] J. M. Marmolejo-Tejada, P.-H. Chang, P. Lazic, S. Smidstrup, D. Stradi, K. Stokbro, and B. K. Nikolic. Topological-insulator/ferromagnetic-metal interface band and spin structure decoded by first-principles Green functions and tunneling anisotropic magnetoresistance. *ArXiv e-prints*, January 2017.

[118] A. R. Mellnik, J. S. Lee, A. Richardella, J. L. Grab, P. J. Mintun, M. H. Fischer, A. Vaezi, A. Manchon, E.-A. Kim, N. Samarth, and D. C. Ralph. Spin-transfer torque generated by a topological insulator. *Nature*, 511(7510):449–451, July 2014.

[119] V. N. Men'shov, V. V. Tugushev, S. V. Eremeev, P. M. Echenique, and E. V. Chulkov. Band bending driven evolution of the bound electron states at the interface between a three-dimensional topological insulator and a three-dimensional normal insulator. *Phys. Rev. B*, 91:075307, Feb 2015.

[120] S. Nakajima. The crystal structure of $Bi_2Te_{3-x}Se_x$. *J. Phys. Chem. Solids*, 24(3):479–485, 1963.

[121] Rahul Nandkishore, L. S. Levitov, and A. V. Chubukov. Chiral superconductivity from repulsive interactions in doped graphene. *Nat Phys*, 8(2):158–163, February 2012.

[122] Rahul Nandkishore, Ronny Thomale, and Andrey V. Chubukov. Superconductivity from weak repulsion in hexagonal lattice systems. *Phys. Rev. B*, 89:144501, Apr 2014.

[123] Rahul Nandkishore, Ronny Thomale, and Andrey V. Chubukov. Super-

conductivity from weak repulsion in hexagonal lattice systems. *Phys. Rev. B*, 89:144501, Apr 2014.

[124] Chetan Nayak, Steven H. Simon, Ady Stern, Michael Freedman, and Sankar Das Sarma. Non-abelian anyons and topological quantum computation. *Rev. Mod. Phys.*, 80:1083–1159, Sep 2008.

[125] K. D. Nelson, Z. Q. Mao, Y. Maeno, and Y. Liu. Odd-parity superconductivity in sr2ruo4. *Science*, 306(5699):1151–1154, November 2004.

[126] Johnpierre Paglione, C. Lupien, W. MacFarlane, J. Perz, Louis Taillefer, Z. Mao, and Y. Maeno. Elastic tensor of sr_2ruo_4. *Phys. Rev. B*, 65:220506, May 2002.

[127] Z.-H. Pan, E. Vescovo, A. V. Fedorov, D. Gardner, Y. S. Lee, S. Chu, G. D. Gu, and T. Valla. Electronic structure of the topological insulator bi_2se_3 using angle-resolved photoemission spectroscopy: Evidence for a nearly full surface spin polarization. *Phys. Rev. Lett.*, 106:257004, Jun 2011.

[128] Kyungwha Park, Christophe De Beule, and Bart Partoens. The ageing effect in topological insulators: evolution of the surface electronic structure of bi 2 se 3 upon k adsorption. *New Journal of Physics*, 15(11):113031, 2013.

[129] S. R. Park, W. S. Jung, Chul Kim, D. J. Song, C. Kim, S. Kimura, K. D. Lee, and N. Hur. Quasiparticle scattering and the protected nature of the topological states in a parent topological insulator bi_2se_3. *Phys. Rev. B*, 81:041405, Jan 2010.

[130] J. P. Perdew, K. Burke, and M. Ernzerhof. Generalized Gradient Approximation Made Simple. *Phys. Rev. Lett.*, 77(18):3865–3868, 1996.

[131] John P. Perdew, Kieron Burke, and Matthias Ernzerhof. Generalized gradient approximation made simple. *Phys. Rev. Lett.*, 77:3865–3868, Oct 1996.

[132] Dmytro Pesin and Allan H. MacDonald. Spintronics and pseudospintronics in graphene and topological insulators. *Nat Mater*, 11(5):409–416, May 2012.

[133] Jingshan Qi, Xiao Li, Qian Niu, and Ji Feng. Giant and tunable valley degeneracy splitting in $mote_2$. *Phys. Rev. B*, 92:121403, Sep 2015.

[134] Xiao-Liang Qi and Shou-Cheng Zhang. Topological insulators and superconductors. *Rev. Mod. Phys.*, 83:1057–1110, Oct 2011.

[135] S. Raghu, A. Kapitulnik, and S. A. Kivelson. Hidden quasi-one-dimensional superconductivity in ¡span class=”aps-inline-formula”¿¡math display=”inline”¿¡msub¿¡mi¿sr¡/mi¿¡mn¿2¡/mn¿¡/msub¿¡msub¿¡mi¿ruo¡/mi¿¡mn¿4¡/mn¿ *Phys. Rev. Lett.*, 105:136401, Sep 2010.

[136] S. Raghu, A. Kapitulnik, and S. A. Kivelson. Hidden quasi-one-dimensional superconductivity in ¡span class=”aps-inline-formula”¿¡math display=”inline”¿¡msub¿¡mi¿sr¡/mi¿¡mn¿2¡/mn¿¡/msub¿¡msub¿¡mi¿ruo¡/mi¿¡mn¿4¡/mn¿ *Phys. Rev. Lett.*, 105:136401, Sep 2010.

[137] S. Raghu, A. Kapitulnik, and S. A. Kivelson. Hidden quasi-one-dimensional superconductivity in sr2ruo4. *Phys. Rev. Lett.*, 105:136401, Sep 2010.

[138] S. Raghu, S. A. Kivelson, and D. J. Scalapino. Superconductivity in the repulsive hubbard model: An asymptotically exact weak-coupling solution. *Phys. Rev. B*, 81:224505, Jun 2010.

[139] S. Raghu, S. A. Kivelson, and D. J. Scalapino. Superconductivity in the repulsive hubbard model: An asymptotically exact weak-coupling solution. *Phys. Rev. B*, 81:224505, Jun 2010.

[140] S. Raghu, S. A. Kivelson, and D. J. Scalapino. Superconductivity in the repulsive hubbard model: An asymptotically exact weak-coupling solution. *Phys. Rev. B*, 81:224505, Jun 2010.

[141] Ashwin Ramasubramaniam. Large excitonic effects in monolayers of molybdenum and tungsten dichalcogenides. *Phys. Rev. B*, 86:115409, Sep 2012.

[142] N. Read and Dmitry Green. Paired states of fermions in two dimensions with breaking of parity and time-reversal symmetries and the fractional quantum hall effect. *Phys. Rev. B*, 61:10267–10297, Apr 2000.

[143] N. Read and Dmitry Green. Paired states of fermions in two dimensions with breaking of parity and time-reversal symmetries and the fractional quantum hall effect. *Phys. Rev. B*, 61:10267–10297, Apr 2000.

[144] R. Roldán, E. Cappelluti, and F. Guinea. Interactions and superconductivity in heavily doped mos_2. *Phys. Rev. B*, 88:054515, Aug 2013.

[145] M. Rösner, S. Haas, and T. O. Wehling. Phase diagram of electron-doped dichalcogenides. *Phys. Rev. B*, 90:245105, Dec 2014.

[146] Emil J Rozbicki, James F Annett, Jean-René Souquet, and Andrew P Mackenzie. Spin–orbit coupling and k -dependent zeeman splitting in strontium ruthenate. *Journal of Physics: Condensed Matter*, 23(9):094201, 2011.

[147] Benjamin Sacp, Jeroen B. Oostinga, Jian Li, Alberto Ubaldini, Nuno J.G. Couto, Enrico Giannini, and Alberto F. Morpurgo. Gate-tuned normal and superconducting transport at the surface of a topological insulator. *Nat Commun*, 2:575–, December 2011.

[148] Manfred Salmhofer. Continuous renormalization for fermions and fermi liquid theory. *Commun. Math. Phys.*, 194(2):249–295, 1998.

[149] Thomas Scaffidi, Jesper C. Romers, and Steven H. Simon. Pairing symmetry and dominant band in sr_2ruo_4. *Phys. Rev. B*, 89:220510, Jun 2014.

[150] Thomas Scaffidi, Jesper C. Romers, and Steven H. Simon. Pairing symmetry and dominant band in sr_2ruo_4. *Phys. Rev. B*, 89:220510, Jun 2014.

[151] R. Shankar. Renormalization-group approach to interacting fermions. *Rev. Mod. Phys.*, 66:129–192, Jan 1994.

[152] Wu Shi, Jianting Ye, Yijin Zhang, Ryuji Suzuki, Masaro Yoshida, Jun Miyazaki, Naoko Inoue, Yu Saito, and Yoshihiro Iwasa. Superconductivity series in transition metal dichalcogenides by ionic gating. *Scientific Reports*, 5:12534–, August 2015.

[153] Manfred Sigrist and Kazuo Ueda. Phenomenological theory of unconventional superconductivity. *Rev. Mod. Phys.*, 63:239–311, Apr 1991.

[154] E. Sosenko, J. Zhang, and V. Aji. Superconductivity in transition metal dichalcogenides. *ArXiv e-prints*, December 2015.

[155] Catalin D. Spataru and Fran çois Léonard. Fermi-level pinning, charge transfer, and relaxation of spin-momentum locking at metal contacts to topological insulators. *Phys. Rev. B*, 90:085115, Aug 2014.

[156] H. Steinberg, J.-B. Laloe, V. Fatemi, J. S. Moodera, and P. Jarillo-Herrero. Electrically tunable surface-to-bulk coherent coupling in topological insulator thin films. *Phys. Rev. B*, 84:233101, Dec 2011.

[157] Alexander Steppke, Lishan Zhao, Mark E. Barber, Thomas Scaffidi, Fabian Jerzembeck, Helge Rosner, Alexandra S. Gibbs, Yoshiteru Maeno, Steven H. Simon, Andrew P. Mackenzie, and Clifford W. Hicks. Strong peak in tc of sr2ruo4 under uniaxial pressure. *Science*, 355(6321), 2017.

[158] Michael Stone and Rahul Roy. Edge modes, edge currents, and gauge invariance in p_x+ip_y superfluids and superconductors. *Phys. Rev. B*, 69:184511, May 2004.

[159] R. Suzuki, M. Sakano, Y. J. Zhang, R. Akashi, D. Morikawa, A. Harasawa, K. Yaji, K. Kuroda, K. Miyamoto, T. Okuda, K. Ishizaka, R. Arita, and Y. Iwasa. Valley-dependent spin polarization in bulk mos2 with broken inversion symmetry. *Nat Nano*, 9(8):611–617, August 2014.

[160] Ronny Thomale, Christian Platt, Jiangping Hu, Carsten Honerkamp, and B. Andrei Bernevig. Functional renormalization-group study of the doping dependence of pairing symmetry in the iron pnictide superconductors. *Phys. Rev. B*, 80:180505, Nov 2009.

[161] D. J. Thouless, M. Kohmoto, M. P. Nightingale, and M. den Nijs. Quantized hall conductance in a two-dimensional periodic potential. *Phys. Rev. Lett.*, 49:405–408, Aug 1982.

[162] Miguel M. Ugeda, Aaron J. Bradley, Su-Fei Shi, Felipe H. da Jornada, Yi Zhang, Diana Y. Qiu, Wei Ruan, Sung-Kwan Mo, Zahid Hussain, Zhi-Xun Shen, Feng Wang, Steven G. Louie, and Michael F. Crommie. Giant bandgap renormalization and excitonic effects in a monolayer transition metal dichalcogenide semiconductor. *Nat Mater*, 13(12):1091–1095, December 2014.

[163] Loïg Vaugier, Hong Jiang, and Silke Biermann. Hubbard u and hund exchange j in transition metal oxides: Screening versus localization trends from constrained random phase approximation. *Phys. Rev. B*, 86:165105, Oct 2012.

[164] C. N. Veenstra, Z.-H. Zhu, M. Raichle, B. M. Ludbrook, A. Nicolaou, B. Slomski, G. Landolt, S. Kittaka, Y. Maeno, J. H. Dil, I. S. Elfimov, M. W. Haverkort, and A. Damascelli. Spin-orbital entanglement and the

breakdown of singlets and triplets in sr_2ruo_4 revealed by spin- and angle-resolved photoemission spectroscopy. *Phys. Rev. Lett.*, 112:127002, Mar 2014.

[165] M. Veldhorst, M. Snelder, M. Hoek, T. Gang, V. K. Guduru, X. L. Wang, U. Zeitler, W. G. van der Wiel, A. A. Golubov, H. Hilgenkamp, and A. Brinkman. Josephson supercurrent through a topological insulator surface state. *Nat Mater*, 11(5):417–421, May 2012.

[166] Jörn W. F. Venderbos, Vladyslav Kozii, and Liang Fu. Odd-parity superconductors with two-component order parameters: Nematic and chiral, full gap, and majorana node. *Phys. Rev. B*, 94:180504, Nov 2016.

[167] G.E. Volovik. On edge states in superconductors with time inversion symmetry breaking. *JETP Lett.*, 66(7):522–527, 1997.

[168] G.E. Volovik. *Universe in a Helium Droplet*. Oxford University Press, 2003.

[169] R. Wakatsuki and K. T. Law. Proximity effect and Ising superconductivity in superconductor/transition metal dichalcogenide heterostructures. *ArXiv e-prints*, April 2016.

[170] Mei-Xiao Wang, Canhua Liu, Jin-Peng Xu, Fang Yang, Lin Miao, Meng-Yu Yao, C. L. Gao, Chenyi Shen, Xucun Ma, X. Chen, Zhu-An Xu, Ying Liu, Shou-Cheng Zhang, Dong Qian, Jin-Feng Jia, and Qi-Kun Xue. The coexistence of superconductivity and topological order in the bi2se3 thin films. *Science*, 336(6077):52–55, 2012.

[171] J. R. Williams, A. J. Bestwick, P. Gallagher, Seung Sae Hong, Y. Cui, Andrew S. Bleich, J. G. Analytis, I. R. Fisher, and D. Goldhaber-Gordon. Unconventional josephson effect in hybrid superconductor-topological insulator devices. *Phys. Rev. Lett.*, 109:056803, Jul 2012.

[172] Di Xiao, Gui-Bin Liu, Wanxiang Feng, Xiaodong Xu, and Wang Yao. Coupled spin and valley physics in monolayers of mos_2 and other group-vi dichalcogenides. *Phys. Rev. Lett.*, 108:196802, May 2012.

[173] Jin-Peng Xu, Mei-Xiao Wang, Zhi Long Liu, Jian-Feng Ge, Xiaojun Yang, Canhua Liu, Zhu An Xu, Dandan Guan, Chun Lei Gao, Dong Qian, Ying Liu, Qiang-Hua Wang, Fu-Chun Zhang, Qi-Kun Xue, and Jin-Feng Jia. Experimental detection of a majorana mode in the core of a magnetic vortex inside a topological insulator-superconductor $bi_2te_3/nbse_2$ heterostructure. *Phys. Rev. Lett.*, 114:017001, Jan 2015.

[174] Hong Yao and Fan Yang. Topological odd-parity superconductivity at type-ii two-dimensional van hove singularities. *Phys. Rev. B*, 92:035132, Jul 2015.

[175] Hong Yao and Fan Yang. Topological odd-parity superconductivity at type-ii two-dimensional van hove singularities. *Phys. Rev. B*, 92:035132, Jul 2015.

[176] Oleg V. Yazyev, Joel E. Moore, and Steven G. Louie. Spin polarization and transport of surface states in the topological insulators bi_2se_3 and bi_2te_3 from first principles. *Phys. Rev. Lett.*, 105:266806, Dec 2010.

[177] J. T. Ye, Y. J. Zhang, R. Akashi, M. S. Bahramy, R. Arita, and Y. Iwasa. Superconducting dome in a gate-tuned band insulator. *Science*, 338(6111):1193–1196, 2012.

[178] Y. A. Ying, N. E. Staley, Y. Xin, K. Sun, X. Cai, D. Fobes, T. J. Liu, Z. Q. Mao, and Y. Liu. Enhanced spin-triplet superconductivity near dislocations in sr2ruo4. *Nat Commun*, 4:2596, 2013.

[179] Takehito Yokoyama, Jiadong Zang, and Naoto Nagaosa. Theoretical study of the dynamics of magnetization on the topological surface. *Phys. Rev. B*, 81:241410, Jun 2010.

[180] Shingo Yonezawa, Kengo Tajiri, Suguru Nakata, Yuki Nagai, Zhiwei Wang, Kouji Segawa, Yoichi Ando, and Yoshiteru Maeno. Thermodynamic evidence for nematic superconductivity in cuxbi2se3. *Nat Phys*, 13(2):123–126, February 2017.

[181] J. Yuan and C. Honerkamp. Triplet pairing driven by Hund's coupling in doped monolayer MoS$_2$. *ArXiv e-prints*, April 2015.

[182] Noah F. Q. Yuan, Kin Fai Mak, and K. T. Law. Possible topological superconducting phases of mos_2. *Phys. Rev. Lett.*, 113:097001, Aug 2014.

[183] D. Zanchi and H. J. Schulz. Superconducting instabilities of the non-half-filled hubbard model in two dimensions. *Phys. Rev. B*, 54:9509–9519, Oct 1996.

[184] Hui Zhai, Fa Wang, and Dung-Hai Lee. Antiferromagnetically driven electronic correlations in iron pnictides and cuprates. *Phys. Rev. B*, 80:064517, Aug 2009.

[185] Duming Zhang, Jian Wang, Ashley M. DaSilva, Joon Sue Lee, Humberto R. Gutierrez, Moses H. W. Chan, Jainendra Jain, and Nitin Samarth. Superconducting proximity effect and possible evidence for pearl vortices in a candidate topological insulator. *Phys. Rev. B*, 84:165120, Oct 2011.

[186] Haijun Zhang, Chao-Xing Liu, Xiao-Liang Qi, Xi Dai, Zhong Fang, and Shou-Cheng Zhang. Topological insulators in bi2se3, bi2te3 and sb2te3 with a single dirac cone on the surface. *Nat Phys*, 5(6):438–442, June 2009.

[187] Haijun Zhang, Chao-Xing Liu, Xiao-Liang Qi, Xi Dai, Zhong Fang, and Shou-Cheng Zhang. Topological insulators in bi2se3, bi2te3 and sb2te3 with a single dirac cone on the surface. *Nat Phys*, 5(6):438–442, June 2009.

[188] Yi Zhang, Ke He, Cui-Zu Chang, Can-Li Song, Li-Li Wang, Xi Chen, Jin-Feng Jia, Zhong Fang, Xi Dai, Wen-Yu Shan, Shun-Qing Shen, Qian Niu, Xiao-Liang Qi, Shou-Cheng Zhang, Xu-Cun Ma, and Qi-Kun Xue. Crossover of the three-dimensional topological insulator bi2se3 to the two-dimensional limit. *Nat Phys*, 6(8):584–588, August 2010.

[189] Zhen Zheng, Ming Gong, Xubo Zou, Chuanwei Zhang, and Guangcan Guo. Route to observable fulde-ferrell-larkin-ovchinnikov phases in three-dimensional spin-orbit-coupled degenerate fermi gases. *Phys. Rev. A*, 87:031602, Mar 2013.

[190] Z. Y. Zhu, Y. C. Cheng, and U. Schwingenschlögl. Giant spin-orbit-induced spin splitting in two-dimensional transition-metal dichalcogenide semiconductors. *Phys. Rev. B*, 84:153402, Oct 2011.

[191] Mark A. Zurbuchen, Yunfa Jia, Stacy Knapp, Altaf H. Carim, Darrell G. Schlom, Ling-Nian Zou, and Ying Liu. Suppression of superconductivity by crystallographic defects in epitaxial sr2ruo4 films. *Appl. Phys. Lett.*, 78(16):2351–2353, 2001.